

**Characterization of Hyperpolarized ^{129}Xe Dissolved in
Perfluorooctyl Bromide Emulsions as a Novel Magnetic
Resonance Contrast Agent**

by

Mihai Raul Gherase

M.Sc. (University of Bucharest) 2001

A thesis submitted to the
Faculty of Graduate Studies and Research
in partial fulfillment of the requirements
for the degree of

DOCTOR OF PHILOSOPHY

(Physics)

Ottawa-Carleton Institute for Physics

Department of Physics

Carleton University

April 19, 2006

© 2006, Mihai Raul Gherase



Library and
Archives Canada

Bibliothèque et
Archives Canada

Published Heritage
Branch

Direction du
Patrimoine de l'édition

395 Wellington Street
Ottawa ON K1A 0N4
Canada

395, rue Wellington
Ottawa ON K1A 0N4
Canada

Your file *Votre référence*
ISBN: 978-0-494-18220-8
Our file *Notre référence*
ISBN: 978-0-494-18220-8

NOTICE:

The author has granted a non-exclusive license allowing Library and Archives Canada to reproduce, publish, archive, preserve, conserve, communicate to the public by telecommunication or on the Internet, loan, distribute and sell theses worldwide, for commercial or non-commercial purposes, in microform, paper, electronic and/or any other formats.

The author retains copyright ownership and moral rights in this thesis. Neither the thesis nor substantial extracts from it may be printed or otherwise reproduced without the author's permission.

AVIS:

L'auteur a accordé une licence non exclusive permettant à la Bibliothèque et Archives Canada de reproduire, publier, archiver, sauvegarder, conserver, transmettre au public par télécommunication ou par l'Internet, prêter, distribuer et vendre des thèses partout dans le monde, à des fins commerciales ou autres, sur support microforme, papier, électronique et/ou autres formats.

L'auteur conserve la propriété du droit d'auteur et des droits moraux qui protègent cette thèse. Ni la thèse ni des extraits substantiels de celle-ci ne doivent être imprimés ou autrement reproduits sans son autorisation.

In compliance with the Canadian Privacy Act some supporting forms may have been removed from this thesis.

Conformément à la loi canadienne sur la protection de la vie privée, quelques formulaires secondaires ont été enlevés de cette thèse.

While these forms may be included in the document page count, their removal does not represent any loss of content from the thesis.

Bien que ces formulaires aient inclus dans la pagination, il n'y aura aucun contenu manquant.


Canada

Abstract

Current imaging methods used for cancer detection are limited in terms of sensitivity, specificity and spatial resolution. Dynamic contrast-enhanced magnetic resonance imaging (DCE-MRI) methods with Gadolinium-diethylenetriaminepentaacetic acid (Gd-DTPA) are promising, but limited by the fact that contrast is obtained indirectly from the magnetic resonance (MR) signal of the water protons. Hyperpolarized ^{129}Xe (H-Xe) dissolved in perfluorooctyl bromide (PFOB) emulsions stabilized with egg-yolk phospholipid (EYP) has been suggested as a possible *in vivo* MR contrast agent. Xenon is biocompatible, diffusible and soluble in biological media. These properties and the high MR signal of the H-Xe gas represent the rationale of this thesis.

A theoretical radial diffusive exchange model based on the generalized Bloch equations is developed in order to investigate the MR spectra of H-Xe dissolved in PFOB emulsions. In the slow exchange regime, a relationship between the linewidth of the MR peaks and the average residence times of the spins in the two compartments is validated. By fitting the theoretical spectra to experimental spectra, EYP membrane permeability and porosity are estimated. Spectra of H-Xe dissolved in mixtures of PFOB emulsions and blood are presented and the slow exchange relationship is confirmed.

Flow rate measurements using the linewidths of dynamically acquired MR spectra of H-Xe dissolved in PFOB emulsions injected into a flowing water stream are presented. The advantages and limitations of this method for possible *in vivo* blood perfusion measurements for cancer detection, as well as their implications on future work are discussed.

Acknowledgements

I would like to thank my supervisor, Giles Santyr, for the research opportunity in a challenging and interesting field. I'm grateful to all members of the Carleton Magnetic Resonance Facility I had the pleasure to know and work with: Albert Cross, Julia Wallace, Juan Parra-Robles, Ken Nkongchu, Greg Cron, Steve White and Nishard Abdeen. In particular, I would like to thank Julia and Albert for their continuous support, time and patience they showed in presenting me the lab and the experimental techniques specific to my project.

I would like to acknowledge Lisa Bernas for her emulsion droplet size measurements, and Steve Lang and Shane Pawsey from the National Research Council for their valuable assistance with polarization cell preparation.

My mom and my brother have shown me love and unconditional support all my life and the past five years were no different. My sincere gratitude and great sympathy go towards all my friends. Especially, I would like to thank my closest friends in Ottawa, Sorina, Maria and Ken for making my life so much easier and enjoyable all this time.

Table of Contents

Abstract	iii
Acknowledgements	iv
Table of Contents	v
List of Tables	ix
List of Figures	x
List of Abbreviations	xiii
1. Introduction	1
1.1 Historical background	1
1.1.1 Breast Cancer Imaging	1
1.1.2 Nuclear Magnetic Resonance	7
1.1.3 Hyperpolarized Noble Gases	9
1.1.4 Hyperpolarized ^{129}Xe as Contrast Agent	10
1.2 Thesis Overview	13
2. Physics of Hyperpolarized Noble Gas NMR	15
2.1 Introduction	15
2.2 Physics of NMR	15
2.2.1 Nuclear Magnetic Moment in a Static Magnetic Field	15

2.2.2	Nuclear Spin Ensemble in a Static Magnetic Field.	17
2.2.3	Effect of Alternating Magnetic Fields.	20
2.2.4	Relaxation and the Phenomenological Bloch Equations.	23
2.2.5	NMR Signal Detection.	27
2.3	Laser Polarization of Noble Gases.	30
2.4	NMR with Hyperpolarized Noble Gases.	34
3.	Radial Diffusive Exchange Model.	36
3.1	Introduction.	36
3.2	Two-compartment Radial Diffusive Exchange Model.	37
3.3	Methods.	42
3.4	Results and Discussion.	44
3.5	Conclusions.	53
4.	H-Xe Spectroscopy in PFOB Emulsions and Blood.	54
4.2	Introduction.	54
4.2.1	Materials and Methods.	55
4.2.2	Results and Discussion.	60
4.3	NMR Spectroscopy of H-Xe Dissolved in Mixtures of PFOB Emulsions and Blood.	68
4.3.1	Materials and Methods.	68
4.3.2	Results and Discussion.	70
4.4	Conclusions.	74

5. Flow Measurements with H-Xe Dissolved in PFOB Emulsions.	76
5.1 Introduction.	76
5.2 Theory.	77
5.3 Materials and Methods.	79
5.3.1 Experimental Setup.	79
5.3.2 Pulse Sequence Design.	82
5.3.3 Data Analysis.	85
5.4 Results and Discussion.	86
5.5 Conclusions.	91
6. Conclusions and Future Work.	98
6.1 Summary.	98
6.1.1 Theoretical Modeling.	99
6.1.2 Spectra of H-Xe Dissolved in PFOB Emulsions and Blood.	100
6.1.3 Water Flow Measurements.	101
6.2 Future Work.	102
References.	105
Appendix A.	116
Appendix B.	120

List of Tables

3.1.	Parameters used for the simulation of the theoretical spectra.	43
4.1.	Diffusion coefficients, transverse relaxation rates and Ostwald solubility ($T = 37^{\circ}C$, $p = 1 atm$) values of xenon in water and PFOB.	60

List of Figures

1.1.	Schematic representation of the perfluorooctyl bromide (PFOB) droplet in a PFOB emulsion and of the carbon chain of the PFOB molecule. . . .	12
2.1.	Precession of the nuclear magnetic moment in a static magnetic field. . .	18
2.2.	Energy level diagram for nuclear spin $I=1/2$ in a static magnetic field. . .	18
2.3.	Magnetic field in the laboratory frame and in the rotating frame.	22
2.4.	Magnetization trajectory in the laboratory frame and in the rotating frame.	22
2.5.	Graphs of the longitudinal and transverse magnetizations as functions of time.	26
2.6.	FID signal with thermal noise and the corresponding NMR spectrum. . .	29
2.7.	Schematic experimental arrangement for spin-exchange optical pumping	31
2.8.	Interaction of alkali-metal atoms with left-circularly polarized light. . . .	32
2.9.	Scheme of the two spin-exchange mechanisms.	33
3.1.	Two-spherical concentric compartment geometry of the radial diffusive exchange model.	38
3.2.	Theoretical NMR spectra of spins undergoing diffusive exchange between two spherically concentric compartments.	44
3.3.	Semi-logarithmic plot of the sum of resonance peaks FWHM as a function of membrane permeability.	46

3.4.	Plot of the exchange rate dependence on the membrane permeability. . .	48
3.5.	Plot of $1/\tau_1$ and $1/\tau_2$ as a function of radius b for constant radius a	49
3.6.	Plot of $1/\tau_2$ as a function of $V_2/(V_1 + V_2)$	50
3.7.	Plot of τ_1/τ_2 versus V_1/V_2 for three different relative solubilities.	52
3.8.	Plot of the probability of spins crossing the membrane as a function of membrane permeability.	52
4.1.	Normalized histogram of the PFOB emulsion droplet diameter.	56
4.2.	Schematic of the flow ^{129}Xe polarization system and H-Xe cryotrapping method.	58
4.3.	Experimental NMR spectra of xenon dissolved in PFOB emulsions. . .	61
4.4.	Theoretical NMR spectra of xenon dissolved in PFOB emulsions.	61
4.5.	Best fit values of the FWHM of the water and PFOB peaks.	62
4.6.	Plot of the one standard deviation ellipse of the two-parameter fit.	63
4.7.	Plot of theoretical FWHM for different diameters and membrane permeabilities.	64
4.8.	Plot of residence time ratio of xenon in water and PFOB versus volume ratio.	66
4.9.	The main experimental steps of NMR spectra acquisition from H-Xe dissolved in mixtures of blood and PFOB emulsion.	68
4.10.	Plots of typical experimental spectra of H-Xe dissolved in mixtures of PFOB emulsion and blood for three blood volume concentrations.	70
4.11.	Plot of FWHM of the experimental peaks corresponding to H-Xe dissolved in mixtures of PFOB emulsions and blood.	71

4.12.	Graph of exchange rate as a function of blood volume concentration. . . .	74
5.1.	Schematic of the experimental setup used in the flow experiments.	79
5.2.	Semi-logarithmic plot of relative H-Xe dissolved in water signal during the application of 130 RF pulses equally spaced at $TR = 250$ ms.	84
5.3.	Plot of typical dynamic acquisition of NMR spectra of H-Xe dissolved in the PFOB emulsion bolus.	86
5.4.	PFOB concentration-time data plots.	87
5.5.	Plot of the flow rate measurements vs. calibrated flow values.	89
5.6.	Plot of the mean transit time vs. calibrated flow values.	90
5.7.	Plot of the water volume concentration vs. calibrated flow values.	90
5.8.	Plot of the calculated volume of distribution and total diluted emulsion volume vs. calibrated flow values.	92
5.9.	Scheme of proposed <i>in vivo</i> blood concentration measurements.	93
5.10.	Plot of the linear dependence of resonance frequency shift Δf as a function of position Δx for two magnetic field gradient values.	94

List of Abbreviations

AIF	Arterial Input Function
CPMG	Carr-Purcell-Meiboom-Gill
CT	Computed Tomography
DCE-MRI	Dynamic Contrast-Enhanced Magnetic Resonance Imaging
DCIS	Ductal Carcinoma <i>In Situ</i>
EYP	Egg-Yolk-Phospholipid
FDG	Fluoro-2-Deoxy-D-Glucose
FFT	Fast Fourier Transform
FID	Free Induction Decay
FWHM	Full Width at Half Maximum
Gd-DTPA	Gadolinium-Diethylenetriaminepentaacetic Acid
HNG	Hyperpolarized Noble Gases
H-Xe	Hyperpolarized ^{129}Xe
LS	Least-Squares
MR	Magnetic Resonance
MRI	Magnetic Resonance Imaging
MTT	Mean Transit Time
NMR	Nuclear Magnetic Resonance
PET	Positron Emission Tomography

PFC	Perfluorocarbon compound
PFOB	Perfluorooctyl Bromide
RBC	Red Blood Cell
RF	Radiofrequency
SPECT	Single Photon Emission Computed Tomography
SNR	Signal-to-Noise Ratio
TR	Repetition Time
TRF	Tissue Residue Function
US	Ultrasound

1. Introduction

1.1. Historical Background

1.1.1. Breast Cancer Imaging

Breast cancer is the most frequent cancer in women in the world [1]. Breast imaging plays an important role within screening and the diagnosis of symptomatic women. Ideally, imaging methods should have high specificity and sensitivity, good cost/effectiveness ratio and they should be non-invasive and harmless [2]. The female breast is also prone to benign disease, so it is very important for a breast imaging technique to discriminate between benign and malignant lesions [1].

The detection of cancer intrinsically depends on its pathology: the sum of all anatomical and physiological changes in the tissues affected by this disease. One of the most important changes which take place in tumours is pathological angiogenesis, a hallmark of cancer and various ischemic and inflammatory diseases [3]. Angiogenesis represents the formation of new blood vessels and it is a key element of a large number of normal and pathological processes [4].

Nutrients and oxygen are distributed to different organs throughout the body using a complex and intricate network of blood vessels. Oxygen diffusion limits the survival of mammalian cells within a distance of 100 to 200 μm from blood vessels.

Therefore, tumour growth is not possible without the recruitment of new blood vessels [3]. Without blood vessels, tumours cannot grow beyond a critical size or metastasize to another organ. In healthy tissues, angiogenesis is regulated by a balance between pro- and anti-angiogenic molecules. This biological mechanism can be derailed towards abnormal blood vessel growth in various diseases, especially cancer [3].

Measurements indicating the existence of pathological angiogenesis in tissues have been suggested as a method for early cancer detection. In 1976, Gullino showed that cells in pre-cancerous tissue acquire angiogenic capacity on their way to becoming cancerous [5]. Subsequently, cancer imaging modalities have attempted to exploit the difference between physiological (normal) and pathological (abnormal) parameters in tissues. Such parameters which have been used for cancer diagnosis include: high microvascular blood volume [6], increased glucose uptake [6], altered blood flow and perfusion [7] and blood vessel permeability (i.e. blood vessels leakiness in tumours) [8]. This evolution has been part of a larger process of extending the paradigm of medical imaging from pure anatomical imaging to functional imaging which makes use of both exogenous and endogenous contrast agents and dynamic data acquisition.

Most of the pathological properties of tumours which represent the target of different cancer detection modalities are directly related to abnormal angiogenesis. In general, these biological parameters are not independent of each other, but each of them is more suitable for a particular imaging modality.

Cancer imaging is a vast area of research and clinical practice, so that a comprehensive review is not possible in this introduction. There are many techniques for *in vivo* cancer detection. *In vitro* imaging of cancer cells has played a significant role in

fundamental biological cancer research. These include invasive methods such as optical and electron microscopy, which are, in most cases, excluded as possibilities for *in vivo* cancer diagnosis in humans. The final goal of all cancer imaging modalities is to serve as a reliable early detector of cancer via quantitative measurements and/or qualitative assessments of various biological properties and functions.

In vivo imaging modalities which are currently used in clinics or have great promise for future use are: (i) X-ray imaging (i.e. mammography) and computed tomography (CT), (ii) magnetic resonance (MR) imaging, (iii) nuclear medicine techniques: positron emission tomography (PET) and single photon emission computed tomography (SPECT), (iv) ultrasound (US), (v) optical imaging and (vi) electrical impedance techniques. In particular, X-ray mammography, nuclear medicine, ultrasound (US) and MR imaging deserve further attention.

X-ray mammography is the most important breast imaging technique and has proven to be effective in reducing breast cancer mortality in a number of screening programs [1]. The main limitation for mammography which has been identified and reported is the severe decrease in sensitivity (i.e. probability that malignant diseases will be detected) for imaging of dense breasts [1] [9]. This difficulty is related to the fact that lesions in these breasts are frequently surrounded by normal fibroglandular tissues which have similar X-ray attenuation properties [9]. In addition, the carcinogenic potential of ionizing radiation remains one of the risks of mammography [1].

Ultrasound imaging of breast cancer is particularly efficient in the differentiation between cyst and solid masses [10]. The main limitations of ultrasound imaging remain

poor detection of microcalcifications in ductal carcinoma *in situ* (DCIS), long scan times and the difficulty to ensure that the entire breast has been imaged [10].

PET with 2-[fluorine-18]-fluoro-2-deoxy-D-glucose (F-18-FDG) tests the uptake of glucose in the tissue whose increase has been linked to the presence of cancer [6]. Since increase in the glucose uptake is common to all cancerous tissues, PET applications extend to the majority of cancers [11]. PET is a functional imaging modality ideally suited for pre-clinical and clinical imaging of cancer biology. This is due to the fact that natural biological molecules can be labelled with positron-emitting isotopes. Hence, PET is able to measure the kinetic parameters which characterize tracer movement and metabolism within the body. All cells metabolize glucose, so FDG is not specific for malignant transformation [11]. Although, in principle, PET should be useful in depicting multifocal diseases, the limitations of PET in detecting small lesions in the breast (spatial resolution of clinical PET systems ~ 4 mm) have limited the role of PET in the breast cancer diagnosis [12].

MR imaging for detecting breast cancer consists of methods based on the difference between MR relaxation properties of normal tissues and cancerous tissues [13] and dynamic contrast-enhanced magnetic resonance imaging (DCE-MRI) which is based on contrast agents such as gadolinium diethylenetriamine pentaacetic (Gd-DTPA).

Conventional MR imaging exploits the differences between proton relaxation times in different soft tissues and/or proton densities in order to produce image contrast. Unfortunately, MR fails to distinguish breast cancer from normal or benign tissues due to the overlap in relaxation times between malignant and non-malignant breast tissue. While

hybrid imaging approaches might improve the sensitivity of these methods to breast disease, the specificity remains a problem [13].

DCE-MRI is an imaging method which consists of dynamic acquisition of MR images following the administration of intravenous contrast medium. The main idea consists of the acquisition of local MR concentration-time curves of the contrast agent. Using tracer kinetics models, various parameters of blood microcirculation such as blood vessel permeability, blood flow and blood volume can be measured. In this way, tumour vascular characteristics are detected and can be quantified using the analysis of contrast agent bolus passage in a dynamically acquired sequence of MR images [14] [15]. The reported sensitivity of this method for the visualization of invasive breast cancer has approached 100% [16] [17]. Yet, there are a number of short-comings of this method such as overlap between malignant and benign inflammatory tissue, failure to resolve microscopic disease and the inconsistent predictive value of enhancement pattern with regard to clinical outcome [15]. Also, there seem to be difficulties in establishing a standard for this multiparametric imaging technique [15] and the goal of absolute perfusion quantification remains problematic [18].

These shortcomings of DCE-MRI are mostly due to the fact that tissue concentration of paramagnetic contrast agents *in vivo* is indirectly measured through shortening of longitudinal relaxation time (T_1) of water protons within the interaction range of the paramagnetic agent. Since water molecules are free to move among different biological compartments (capillaries, cells, and interstitial space), precise determination of microcirculatory parameters using contrast agent kinetic models becomes a difficult task [19].

DCE-MRI is one of the best imaging modalities for breast cancer with almost perfect sensitivity (>95%). In spite of this success, there are problems with detection of microscopic lesions and a clear distinction between malignant and benign tumours. There is also the unsolved problem of absolute quantification of perfusion in this dynamic imaging method. Absolute perfusion measurements could permit investigations of abnormal angiogenesis effects on perfusion as well as open the possibility of studying perfusion variability among individuals for certain tissues and in various diseases such as cancer.

Summarizing, the main problems in breast cancer diagnosis remain the low sensitivity of X-ray mammography for dense breast, the ability to distinguish between benign and malign lesions and the detection of microcalcifications and small lesions.

Combinations of two or more imaging techniques are also found in the medical literature. PET/CT fusion is such an example already used in clinics [20]. The reasoning behind these multimodality approaches is to overcome the drawbacks of one particular technique with complementary modalities. Also, looking at several pathological characteristics of cancerous tissues can result in improved diagnosis. This is the case of dynamic contrast-enhanced magnetic resonance imaging (DCE-MRI) where a few functional parameters are being measured at the same time [14] [15].

In general, there seems to be no ideal imaging modality for cancer diagnosis. In spite of the successes registered by all these methods, each one of them has its own limitations. This is the rationale for the search for a better assessment of the biological parameters mentioned earlier which can further lead to early diagnosis and more efficient treatment.

In this thesis, hyperpolarized ^{129}Xe (H-Xe) dissolved in a perfluorocarbon bromide (PFOB) emulsion is proposed as a new magnetic resonance (MR) contrast agent for cancer imaging, in particular, for breast cancer. This may be achieved by *in vivo* measurements of PFOB concentration in tissues using a quantitative analysis of dynamically-acquired H-Xe MR spectra. The final goal is to investigate if this new proposed modality can overcome the pitfalls of current methods used for cancer detection.

1.1.2. Nuclear Magnetic Resonance

The nuclear magnetic resonance (NMR) phenomenon was discovered independently in 1946 by two research groups led by F. Bloch [21] and E. M. Purcell [22]. Initial research efforts concentrated on NMR spectroscopy with applications in physics, chemistry and biology. Since that time, steady and continuous progress had been made towards understanding fundamental NMR phenomena. NMR spectroscopy, in particular, had evolved to become a rich and versatile field of research, a powerful introspective tool in the analysis of structure and dynamics of matter [23].

NMR research in medicine and biology has grown significantly with the advent of magnetic resonance imaging (MRI) to the area of magnetic resonance (MR) applications. In 1971, Damadian was the first to report the diagnostic potential of NMR to distinguish cancer [24]. He compared the MR relaxation times of six normal tissues in the rat and in two malignant solid tumours and found that “relaxation times for the two malignant tumours were distinctly outside the range of values for the normal tissues studied...”

[24]. The first report of an imaging method based on the NMR phenomenon came in 1973 when Lauterbur published the first MR image of two tubes of water using linear magnetic gradients [25]. Later, in 1976, Mansfield and Maudsley reported the first image of a living human finger [26].

Today, MRI is one of the most important medical imaging modalities used in clinics worldwide as well as an active field of research. For this reason, the pioneers of MRI, P.C. Lauterbur and P. Mansfield were awarded the 2003 Nobel Prize in Physiology or Medicine.

MR imaging exploits the abundance of water in most living tissues (notable exceptions are bone and lung tissues). The two ^1H nuclei (protons) of the water molecule have one half spin suitable for NMR or MRI experiments. Proton MRI has a few advantages over other clinical imaging techniques such as X-ray, nuclear medicine techniques, X-ray computed tomography (CT) or PET: it is a non-invasive and non-ionizing technique, it has high soft tissue contrast and it allows the acquisition of multi-planar cross-sectional images of the body.

Progress has been achieved in both anatomical and functional MR imaging. Phantom studies, *in vivo* and *in vitro* experiments have set the stage for quantitative measurements of biological and physical properties and function of cells, tissues and organs. NMR relaxation properties of tissues, restricted diffusion of water within biological structures, blood flow, water permeabilities of cell membranes and capillaries, perfusion and elastic properties of tissues, and imaging of lungs and cavities with hyperpolarized noble gases (HNG) have all been explored using appropriate MR methods.

1.1.3. Hyperpolarized Noble Gases (HNG)

Despite the advantages of proton MR, there are certain fundamental limitations associated with both anatomical and functional imaging. One of the important limitations is that the acquired signal inherently depends on the strength of the applied static magnetic field [27]. Another important limitation appears in the area of DCE-MRI where the assessment of signal/concentration relationship intrinsically depends on the motion of water molecules between microbiological compartments [14]. The development of HNG production using optical pumping and spin-exchange has brought the possibility of overcoming these limitations.

The optical pumping of alkali atoms was first predicted in 1950 and experimentally demonstrated two years later by A. Kastler [28]. Later, in 1960, Bouchiat *et al.* [29] reported the enhancement of the nuclear spin polarization of ^3He nuclei when used as buffer gas in alkali optical pumping experiments. A more detailed study of this process was published by Colegrove *et al.* [30] three years later. In 1978, B.C. Grover successfully observed the enhancement of nuclear spin polarization of five noble gas isotopes: ^3He , ^{21}Ne , ^{83}Kr , ^{129}Xe and ^{131}Xe using spin-exchange between optically-pumped Rb and noble gases [31]. Further advances in both theoretical frameworks and experimental setup were reported throughout the 1980's by the work of Happer and his collaborators [32]-[34].

In 1991, Pines *et al.* [35] reported NMR spectroscopy studies using hyperpolarized ^{129}Xe . A few years later, Albert *et al.* [36] published the first MR images

of the excised lungs and heart of a mouse using laser-polarized ^{129}Xe . They also speculated that the low cost of xenon gas and availability of polarization systems may open the way to "... ^{129}Xe imaging of any desired portion of a living mammal."

1.1.4. Hyperpolarized ^{129}Xe as Contrast Agent

A prevalent choice of conventional proton MR contrast agents are biocompatible paramagnetic compounds that can be safely injected in the bloodstream. From these compounds, gadolinium chelates (e.g. Gd-DTPA) are the most widely used in clinics [37]. The contrast mechanism is provided by dipolar interaction between proton nuclear spins and unpaired electrons within these compounds that is responsible for the shortening of the NMR relaxation times of water in tissues [14].

The difficulty of using hyperpolarized ^{129}Xe (H-Xe) as a contrast agent for *in vivo* MR measurements stems from the fact that ^{129}Xe is a gas at room temperature and atmospheric pressure. For this reason, the delivery of H-Xe to different tissues is not an easy task. One approach is to dissolve H-Xe in the blood stream and then use perfusion measurements as an indicator of the tissue's pathology.

There are two ways xenon can be delivered efficiently to the blood stream for medical purposes: (i) inhalation through respiration and (ii) direct injection into the blood stream using a biocompatible substance highly soluble to gases (carrier). The first method uses the gas exchange mechanisms in the alveoli of the lungs [38]. Xenon is highly soluble in organic substances [39], where it can then diffuse from the gas space into the blood stream. This method of delivering H-Xe gas has already been used for *in vivo*

experiments and has been reported in several publications [40]-[44]. NMR spectroscopy and MR methods have demonstrated that H-Xe gas can be measured in both blood and tissues (e.g. heart, brain, kidney, etc.).

In 1996, Bifone *et al.* [45] proposed the use of perfluorocarbon compounds to deliver H-Xe to the blood stream. The authors concluded that such a technique was “promising for MRI angiography and perfusion imaging, as well as *in vivo* localized NMR spectroscopy of xenon exchange phenomena.”

Biocompatible compounds for transport of respiratory gases, O₂ and CO₂, also known as “blood substitutes”, have been sought for several decades [46]. In particular, perfluorocarbon compounds (PFCs) have been proposed as carriers for O₂ in the second half of 1960’s [47] [48]. Due to their virtual insolubility in water, PFCs are formulated into emulsions for parenteral administration.

In particular, perfluorooctylbromide (PFOB or perflubron) stands out among candidate PFCs for therapeutic use [46]. It has a relatively fast excretion rate (about 3 days in humans for a 2.7 g/kg dose), it has high gas solubility (O₂, CO₂ and noble gases) [49], it can be easily manufactured in very high purity, it is inert to the conditions of processing, storage and use and it has low viscosity. Also, its emulsions show improved stability when phospholipids are used as emulsifiers. Egg yolk phospholipids (EYP) have been selected as the emulsifier because of very good PFOB emulsion stabilization effect, long history of use in pharmaceutical industry and few side effects related to human use [46].

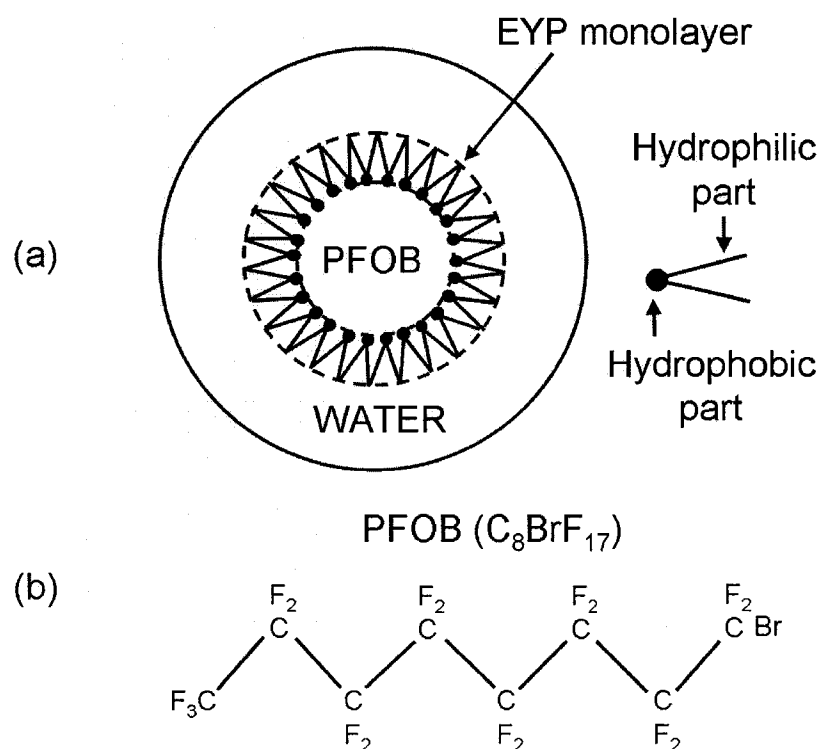


Figure 1.1. (a) Schematic representation of the perfluorooctyl bromide (PFOB) droplet surrounded by the egg-yolk phospholipid (EYP) monolayer in a water-PFOB emulsion. (b) Carbon chain representation of the PFOB molecule [46]. Continuous lines represent covalent bonds between two atoms.

In 1998, Wolber *et al.* [50] investigated the use of PFOB emulsions stabilized with EYP as carriers for intravenous delivery of H-Xe. They analyzed the NMR spectra of H-Xe dissolved in PFOB emulsions and they also reported *in vivo* acquisition of the PFOB peak following an intravenous injection of 1 ml of emulsion in the tail vein of a rat. Three years later, they reported the first *in vivo* H-Xe NMR spectra in tumours [51]. Characteristic differences between the measured NMR longitudinal relaxation times of H-Xe in two types of tumours were observed. The differences were linked to the exchange of H-Xe between the carrier medium and the tissue compartments.

Currently, no phantom work or *in vivo* experiments involving tracking of H-Xe dissolved in PFOB emulsions by means of dynamic data acquisition have been reported. The work presented herein is a preliminary assessment of H-Xe dissolved in PFOB emulsions as a possible contrast agent for cancer detection using dynamic NMR spectroscopy methods and phantom studies. The main advantage of this method compared to DCE-MRI techniques consists in establishing a straightforward relationship between the MR signal and the contrast agent concentration in the blood pool. This also implies possible perfusion measurements using tracer kinetic modelling.

1.2. Thesis Overview

The following chapter (Chapter 2) briefly presents the NMR theory (phenomenological Bloch equations) and the important features of NMR experiments with hyperpolarized gases.

In Chapter 3, an analytical two-compartment radial spin diffusive exchange model is presented. This model permits a complete quantitative analysis of H-Xe dissolved in PFOB emulsions spectra in terms of emulsion droplet size, diffusion coefficients, xenon solubility, and membrane permeability. The results of the model are presented as generalized NMR spectra for any set of input parameters. Spectra corresponding to the slow, intermediate and fast exchange regimes previously discussed in the literature are demonstrated for varying membrane permeability.

A detailed discussion of the slow exchange regime follows the theoretical model presentation. The calculation of residence time in the two compartments based on the spectral full-width at half maximum (FWHM) values is shown. This regime is found to be particularly useful since spectra of H-Xe dissolved in PFOB emulsion and blood are determined by slow exchange of xenon between the PFOB droplets and blood which considerably simplifies the modeling and interpretation of spectra.

Chapter 4 describes the experimental acquisition and analysis of H-Xe dissolved in PFOB emulsions spectra in the first part, and in PFOB emulsion and blood spectra in the second part. The analysis of H-Xe dissolved in different dilutions of PFOB emulsions provides complete characterization of this type of emulsion. FWHM dependence on water volume concentration also reveals a technique for calculating concentrations from spectral linewidths analysis. H-Xe dissolved in PFOB emulsions and blood for three volume concentrations shows the same trend of the spectral linewidths. The slow exchange regime of H-Xe spins between PFOB droplet and water/blood compartment is confirmed.

In Chapter 5, flow measurements of water in a closed loop are performed using the injection of H-Xe dissolved in PFOB emulsion bolus and the quantitative spectral analysis described in Chapter 4 to demonstrate the potential of this technique *in vivo*. Further, a discussion for *in vivo* blood flow measurements shows the potential of this method as a contrast agent for cancer detection.

Chapter 6 summarizes the results presented in the thesis and indicates the future directions of this research.

2. Physics of Hyperpolarized Noble Gases NMR

2.1 Introduction

In this chapter, the basic physical principles of NMR and laser polarization of noble gases are reviewed for a better understanding of the work presented in the following chapters. Section 2.2 is dedicated to the presentation of NMR phenomenology. Section 2.3 describes physical processes behind the enhancement of nuclear polarization of noble gases using laser resonant absorption. The final section of this chapter (section 2.4) highlights the unique features of NMR and MR imaging experiments using hyperpolarized noble gases.

2.2 Physics of NMR

2.2.1 Nuclear Magnetic Moment in a Static Magnetic Field

Magnetic resonance phenomena can be observed in systems of particles that possess both magnetic moments and angular momentum [52]. The nuclei of isotopes with nuclear spin different from zero ($I \neq 0$) are such particles. They are composed of nucleons: protons and neutrons. Individual nucleons have a spin of $1/2$, but their orbital moments are quenched by the interactions present in the nuclei [53]. The nuclear spin I is

the result of the coupling of nuclear spins that form a particular nucleus. Thus, the total angular momentum of the nucleus \vec{J} can be simply written as:

$$\vec{J} = \hbar \vec{I} \quad (2.1)$$

where \vec{I} is the dimensionless angular momentum operator and \hbar is Dirac's constant or reduced Planck's constant $h/2\pi$. \vec{I}^2 has eigenvalues $I(I+1)$ where I is either integer or half-integer [52]. For the isotopes of hydrogen ^1H and xenon ^{129}Xe , $I = 1/2$.

The total magnetic moment $\vec{\mu}$ and the total angular momentum \vec{J} are parallel vectors and are related via the gyromagnetic ratio γ , a scalar constant for a given nucleus:

$$\vec{\mu} = \gamma \vec{J}. \quad (2.2)$$

The gyromagnetic ratios for hydrogen and xenon are: $\gamma_{^1\text{H}} = 266.5 \times 10^6$ rad/T's and $\gamma_{^{129}\text{Xe}} = 73.7 \times 10^6$ rad/T's, respectively.

The interaction of the nuclear magnetic moment $\vec{\mu}$ with a static magnetic field \vec{B}_0 , also known as Zeeman interaction, is described by a simple Hamiltonian:

$$H = -\vec{\mu} \cdot \vec{B}_0. \quad (2.3)$$

Combining equations (2.1) and (2.2), the allowed energies corresponding to the eigenvalues of this Hamiltonian can be written as [52]:

$$E = -\gamma \hbar B_0 m \quad (2.4)$$

where $m = -I, -I+1, \dots, I-1, I$ represent the eigenvalues of I_z . Hence, the energy difference between these levels is:

$$\Delta E = \gamma \hbar B_0. \quad (2.5)$$

Both classical and quantum mechanical treatments of NMR show that the precession represents the dynamics of any isolated magnetic moment $\vec{\mu}$ in a static magnetic field \vec{B}_0 [52]. The angular frequency of precession ω_0 is given by the Larmor equation:

$$\vec{\omega}_0 = -\gamma \vec{B}_0. \quad (2.6)$$

The precession frequency ω_0 is also called the Larmor frequency. The precession of the magnetic moment $\vec{\mu}$ with angular frequency $\vec{\omega}_0$ is depicted in Fig. 2.1.

Using the Larmor frequency ω_0 , the energy separation between adjacent Zeeman energy levels ΔE formulated in Eq. (2.5) can be written as:

$$\Delta E = \hbar \omega_0. \quad (2.7)$$

For typical static magnetic field strengths B_0 (1-4 T) and gyromagnetic ratios of the isotopes used in NMR/MRI applications, ω_0 is in the radio frequency (RF) domain (1-1000 MHz).

2.2.2 Nuclear Spin Ensemble in a Static Magnetic Field

For a population of nuclear spins at thermal equilibrium and in the presence of a static magnetic field B_0 , the ratio between the number of nuclei in the lower energy state n_- and the number of nuclei on the higher energy state n_+ , can be found using Boltzmann statistics [53]:

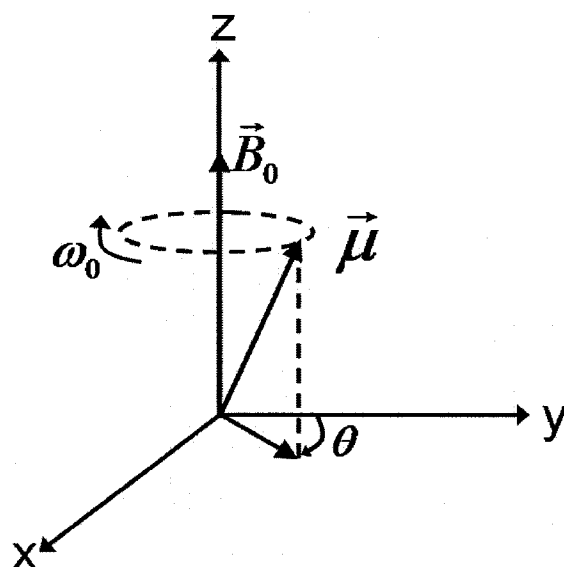


Fig. 2.1. Precession of the nuclear magnetic moment $\vec{\mu}$ in a static magnetic field \vec{B}_0 with the Larmor angular frequency $\omega_0 = \gamma B_0$. The angle θ represents the phase of the precession.

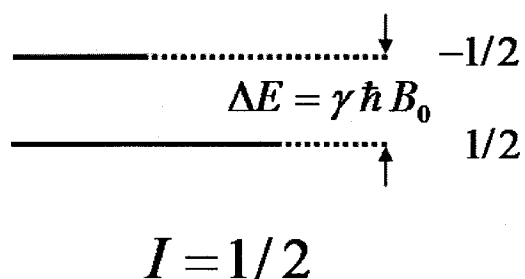


Fig. 2.2. Energy level diagram for nuclear spin $I=1/2$ (b) in a static magnetic field B_0 . The energy difference between levels separated by $\Delta m = \pm 1$ is $\Delta E = \gamma \hbar B_0$. The bold line schematically represents the relative population in each state for an ensemble of spins at thermal equilibrium.

$$\frac{n_-}{n_+} = \exp\left(\frac{\Delta E}{kT}\right). \quad (2.8)$$

In Eq. (2.8), ΔE refers to the energy difference between Zeeman levels and is defined by Eq. (2.5), k is the Boltzmann constant and T is the absolute temperature of the spin system. Zeeman energy level diagrams for nuclear spins $I = 1/2$ and relative population in each state are shown in Fig. 2.2.

For a population of N nuclei with spin $I = 1/2$, one can define the polarization P as the fractional excess of nuclei in the lower energy state:

$$P = \frac{n_+ - n_-}{N}. \quad (2.9)$$

Using Eq. (2.6) the polarization P can be rewritten as:

$$P = \tanh\left(-\frac{\Delta E}{2kT}\right). \quad (2.10)$$

The alignment of spins in the static magnetic field can also be expressed using the concept of magnetization \vec{M} that is defined as the volume density of the sum of all magnetic moments $\vec{\mu}_i$:

$$\vec{M} = \frac{\sum_{i=1}^N \vec{\mu}_i}{V} \quad (2.11)$$

At thermal equilibrium, the nuclear magnetic moments undergo incoherent motions. This means that, in the presence of a static magnetic field \vec{B}_0 , the phases of individual nuclear magnetic moments precession (i.e. spin precession) are not correlated.

As a result, the time average of the sum of all magnetic moment projections on to the plane perpendicular to the static magnetic field \vec{B}_0 (transverse plane) is zero.

For N nuclei with spin $I = 1/2$, the magnetization M per unit volume is:

$$M = |\vec{M}| = \left| \sum_{i=1}^N \vec{\mu}_i \right| = \frac{1}{2} N \gamma \hbar P \quad (2.12)$$

where $\vec{\mu}_i$ (index i having values from 1 to N) represents the total magnetic moment of individual nuclei, γ is the gyromagnetic ratio, \hbar is Dirac's constant and P is the polarization of the spin ensemble.

2.2.3 Effect of Alternating Magnetic Fields

For a better understanding of the effect of alternating magnetic fields on the bulk magnetization of the spin ensemble, the concept of the rotating reference frame proves to be useful. Intuitively this is a natural thing to do, since the Larmor precession is always occurring in the presence of the static magnetic field. A clear description of the rotating frame is given in the paper by Rabi, Ramsey and Schwinger [54].

The NMR phenomenon can be measured after the 'excitation' of a sample of nuclear spins found in a static magnetic field \vec{B}_0 by applying a time-varying magnetic field \vec{B}_1 with RF carrier frequency ω . The most efficient excitation is when magnetic field \vec{B}_1 is applied in a direction perpendicular to the static magnetic field \vec{B}_0 . Thus, individual nuclear magnetic moments are experiencing a combination of the two fields.

In the frame rotating with the same frequency ω of the \vec{B}_1 field, the effective magnetic field \vec{B}_{eff} experienced by the spin system is given by [53]:

$$\vec{B}_{eff} = \vec{B}_1 + \vec{B}_0 - \vec{\omega}/\gamma. \quad (2.13)$$

The difference between the total magnetic fields as they appear in the laboratory frame (\vec{B}_{total}) and in the rotating frame (\vec{B}_{eff}) is shown in Fig. 2.3.

In almost all NMR applications, the magnetic field \vec{B}_1 is applied as a pulse (also called an RF pulse) of t_p duration. The effect of the RF pulse on the magnetization \vec{M} , initially aligned along the direction of the static magnetic field \vec{B}_0 , is shown in Fig. 2.4.

This behaviour, called “nutation”, assumes that the spin ensemble evolution can be represented by the macroscopic angular momentum vector which is simply \vec{M}/γ where \vec{M} is the magnetization and γ is the nuclear gyromagnetic ratio. The equation of motion of the macroscopic angular momentum is obtained by equating the torque with the rate of change of angular momentum [52]:

$$\frac{d\vec{M}}{dt} = \gamma \vec{M} \times \vec{B}. \quad (2.14)$$

On resonance ($\omega = \omega_0$), in the rotating frame ($x' y' z'$), the magnetization \vec{M} is tipped into the ($x' y'$) plane which is perpendicular to the static magnetic field \vec{B}_0 . The tip angle α depends on the magnetic field intensity B_1 of the RF pulse, gyromagnetic ratio γ and the duration of the pulse t_p [53]:

$$\alpha = \gamma \int_0^{t_p} B_1(t) dt. \quad (2.15)$$

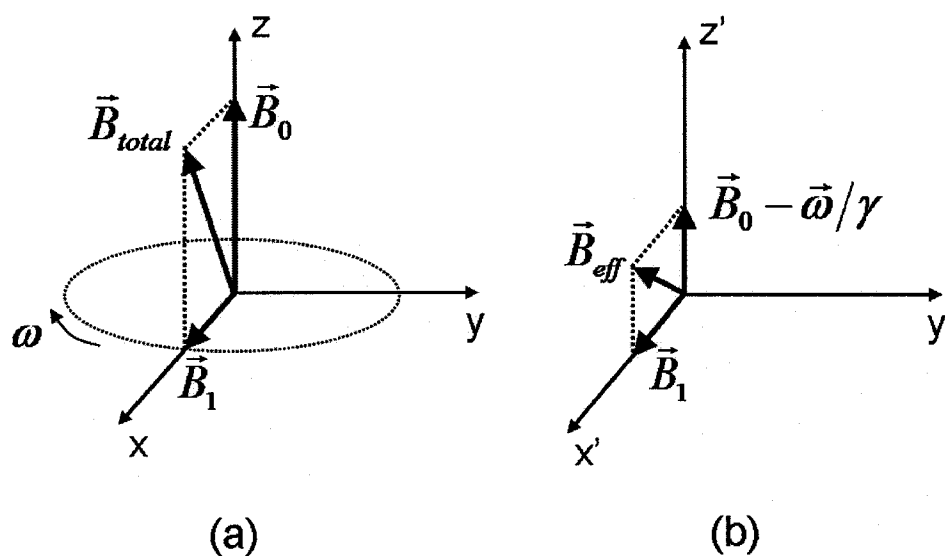


Fig. 2.3. (a) Total magnetic field \vec{B}_{total} in the laboratory frame ($x y z$) and (b) effective field \vec{B}_{eff} in the rotating frame ($x' y' z'$) with angular frequency ω .

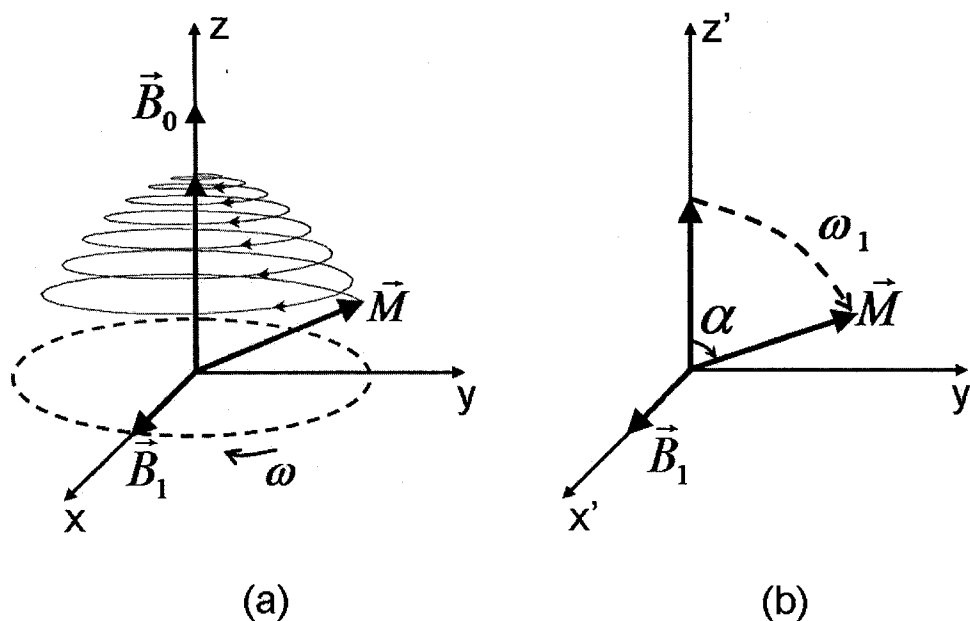


Fig. 2.4. (a) Magnetization trajectory, in the laboratory frame ($x y z$), in the presence of both (i) longitudinal static magnetic field \vec{B}_0 and (ii) transverse rotating field \vec{B}_1 . At resonance, when $\omega = \omega_0$, the magnetization vector simultaneously precesses about \vec{B}_0 at frequency ω_0 and about \vec{B}_1 at frequency ω_1 . (b) Magnetization trajectory in the rotating frame ($x' y' z'$) on resonance ($\omega = \omega_0$). The longitudinal effective field is zero.

In practice, Eq. (2.15) can be used to calculate the tip angle provided that the excitation field B_1 is homogeneous in the region of interest.

2.2.4 Relaxation and the Phenomenological Bloch Equations

A resonant RF pulse perturbs the spin system from its thermal equilibrium state. The return to the equilibrium state involves two types of relaxation. The first is longitudinal or spin-lattice relaxation which represents the return of the longitudinal magnetization M_z (i.e. along the direction of static field B_0) to the equilibrium value M_0 . This process involves the exchange of energy between the spin system and the surrounding thermal reservoir, known as the “lattice”. The phenomenological description first summarized by Bloch is given by the equation [55]:

$$\frac{dM_z}{dt} = -\frac{M_z - M_0}{T_1} \quad (2.16)$$

with solution

$$M_z(t) = M_z(0) \exp(-t/T_1) + M_0 (1 - \exp(-t/T_1)). \quad (2.17)$$

T_1 is referred to as the spin-lattice or longitudinal relaxation time. At room temperature, T_1 is typically in the range 0.1 to 10 seconds for protons in dielectrics [55]. The longitudinal magnetization behaviour implied by Eq. (2.16) is shown graphically in Fig. 2.5 (a).

The second process is the transverse relaxation or the spin-spin relaxation. Transverse magnetization corresponds to a state of phase coherence among the nuclear

spin states. This means that transverse relaxation is sensitive to interaction terms which cause loss of the spin coherence [55]. In the rotating frame, the phenomenological description can be written mathematically as:

$$\frac{dM_{xy}}{dt} = \frac{-M_{xy}}{T_2} \quad (2.18)$$

with solution

$$M_{xy}(t) = M_{xy}(0) \exp(-t/T_2). \quad (2.19)$$

The transverse relaxation described by Eq. (2.18) corresponds to an exponential decay and is graphed in Fig. 2.5 (b). T_2 is called spin-spin or transverse relaxation time. It is important to mention that this behaviour applies to the case where interaction terms responsible for transverse relaxation are weak, the regime of the Bloembergen, Purcell and Pound (BPP) theory [56].

The exponential recovery of the longitudinal magnetization that follows an excitation RF pulse (Eq. 2.16) is the consequence of the interaction of the spins with the surroundings (“lattice”). This return to the thermal equilibrium process is dissipative in nature; part of the absorbed energy from the RF pulse is transferred to the lattice in the form of heat.

On the other hand, transverse magnetization relaxation, in general, conserves energy in the static magnetic field [52]. The detailed interactions behind this coherence loss among neighbouring nuclear spins fit into the quantum statistical physics framework. The investigation of these mechanisms, also called coherence pathways constitutes the field of modern NMR spectroscopy [55].

The process of coherence loss is not only the result of interactions among nuclear spins. Looking at Eq. (2.6), one can observe that any local changes in the applied static magnetic field in frequency domain, translate to the broadening of the resonance peaks. In the time domain, the intrinsic transverse relaxation time T_2 decreases and it is replaced by the apparent transverse relaxation time T_2^* .

There are three distinct contributions influencing the local static field: (i) B_0 inhomogeneities related to the magnet design, (ii) magnetic susceptibility differences related to the sample intrinsic magnetic properties and (iii) chemical shift. The last contribution relates to the fact that the magnetic field at the site of the nucleus depends on the surrounding electron shells, so it depends on the chemical composition of the substances in the spin neighbourhood. As a consequence, at a certain static field B_0 , different substances surrounding a certain nuclear isotope give rise to slightly different resonance frequencies. The chemical shift is usually defined with respect to a reference frequency ω_R to eliminate the dependence on static magnetic field. If the resonance frequency of the sample is ω_S , then the chemical shift δ , in parts per million (ppm), is given by:

$$\delta = \frac{\omega_S - \omega_R}{\omega_R} \cdot 10^6. \quad (2.20)$$

Diffusion and chemical exchange can also influence the transverse relaxation time [55].

In practice, the effect of B_0 inhomogeneities is the most common. This effect can be diminished by using active or passive shimming and it can be negligible if the sample size is small. Measurements of transverse relaxation time T_2 can be accomplished by employing a special pulse sequence consisting in an 90° RF pulse followed by equal

spaced 180° RF pulses refocusing transverse magnetization loss due to static magnetic field inhomogeneities. This pulse sequence is called the Carr-Purcell-Meiboom-Gill (CPMG) sequence, an acronym of the inventors who originally contributed to its development [57] [58].

The effects of chemical shift, susceptibility differences, chemical exchange and diffusion can only be partially corrected using pulse sequences such as CPMG. They represent fundamental limits for resolution and signal-to noise ratio (SNR) in MRI [55] and they pose challenges for precise measurements in applications such as DCE-MRI. Their detailed analysis proves to be useful in different research areas such as the one presented in this thesis.

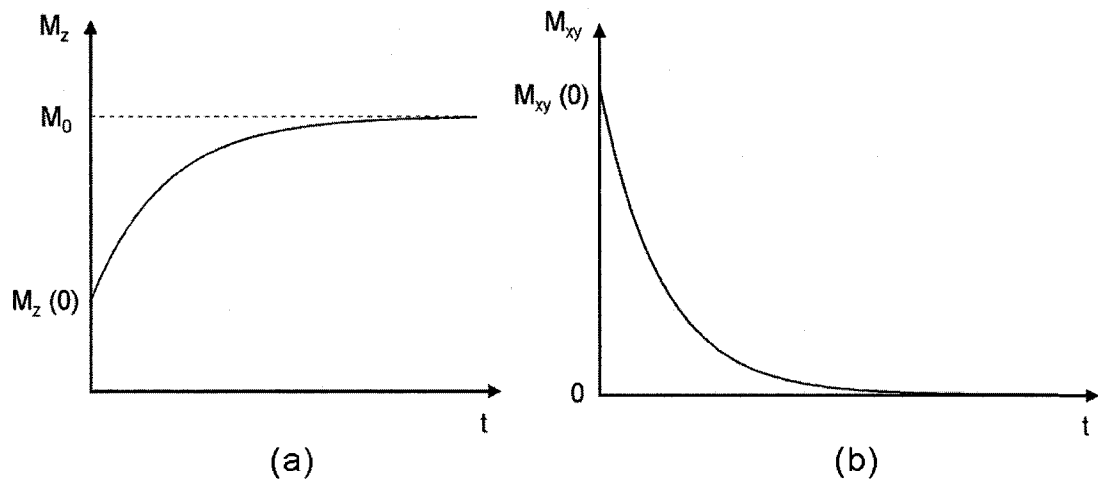


Fig. 2.5. Graphs of the (a) longitudinal magnetization M_z and (b) transverse magnetization M_{xy} relaxation as a function of time, t .

Combining Eqs. (2.14), (2.16) and (2.18) in the rotating frame, the behaviour of the magnetization vector \vec{M} can be described by the phenomenological Bloch equations [52][55]. These equations can be written as a single vector equation:

$$\frac{d\vec{M}}{dt} = \vec{M} \times \gamma \vec{B} - \frac{M_x \hat{x} + M_y \hat{y}}{T_2} - \frac{(M_z - M_0) \hat{z}}{T_1} \quad (2.21)$$

where \hat{x} , \hat{y} and \hat{z} are the unit vectors in the x , y and z directions respectively, M_0 is the equilibrium magnetization and \vec{B} includes the magnetic fields applied (\vec{B}_0 and \vec{B}_1).

Although they have some limitations (classical vectorial equations describing the dynamics of macroscopic magnetization), Bloch equations play an important role in understanding magnetic resonance phenomena, since they provide a very simple way of introducing relaxation effects. They can explain most of the spin manipulations for spin 1/2 systems and combined with the classical diffusion equation form the so-called generalized Bloch equations or the Bloch-Torrey equations [59]. In this form, they are the basis of the theoretical model presented in the next chapter.

2.2.5 NMR Signal Detection

The NMR signal detection can be explained using the magnetic field version of the Principle of Reciprocity which is, in fact, a form of the Faraday law of electromagnetic induction [60][61]. The main device used for NMR signal detection is an RF coil that is properly tuned to the Larmor frequency of the sample in the static magnetic field \vec{B}_0 . The same coil can be used to produce both the excitation magnetic field \vec{B}_1 (RF pulse) as well as detect the NMR signal.

The voltage induced in the coil by the dynamics of the sample magnetization can be derived from the basic laws of classical electrodynamics in the near-field approximation (i.e. the wavelength corresponding to the Larmor frequency is larger than

the sample size) [61]. In this context, the Principle of Reciprocity states that if the \hat{B}_1 created at the NMR sample by a unit of direct current in the coil is known, then the voltage ξ induced in the coil by the precession of the nuclear magnetic moment $\bar{\mu}$ is proportional to the strength of this hypothetical field and given by the scalar product [61]:

$$\xi = -\frac{\partial}{\partial t}(\hat{B}_1 \cdot \bar{\mu}). \quad (2.22)$$

Equation (2.21) can be applied to calculate the induced voltage for an NMR sample of volume V_s [62]:

$$\xi = -\frac{\partial}{\partial t} \int_{V_s} (B_1(\bar{r}))_{xy} M_{xy}(\bar{r}, t) dV. \quad (2.23)$$

The voltage ξ induced in the RF coil represents the NMR signal and typically is on order of a microvolt (μV) [55]. This signal is amplified and then digitized. The high frequency component of the signal is removed through phase-sensitive detection (or dual-phase detection). By separately mixing the signal with two reference signals 90° out of phase, separate in-phase and quadrature phase output signals can be obtained proportional to the orthogonal components of the transverse magnetization: M_x and M_y . Using two low-pass filters, the frequency of the reference signal ω_r and the resulting signal (also called baseband signal) oscillates at the offset frequency: $\Delta\omega = \omega_0 - \omega_r$. This method, almost universally adopted, allows the detection of both the amplitude and the phase of the NMR signal [63].

Inspection of Eq. (2.23) shows that the induced voltage ξ depends strictly on the existence of transverse magnetization M_{xy} . Longitudinal magnetization M_z does not contribute to the NMR signal detection. The time dependence of the signal reflects the

dynamics of the transverse magnetization M_{xy} that follows the excitation. The frequency spectrum of the signal is obtained by applying the Fourier Transform or its practical implementation: the Fast Fourier Transform (FFT) algorithm [64]. The curve showing the signal induced in the coil by the free precession of the transverse magnetization is called the free induction decay (FID). The envelope of the signal is, in general, an exponential decay described by Eq. (2.19) where transverse relaxation time T_2 has to be replaced by T_2^* to account for the effects of the static field inhomogeneities. Correspondingly, in the frequency domain, the spectrum is represented by a Lorentzian-shaped peak which can be described by the full-width-at-half-maximum (FWHM). The following equation relates the two parameters:

$$FWHM = \frac{1}{\pi T_2^*} \quad (2.24)$$

An experimental FID signal and its corresponding spectrum are shown in Fig. 2.6.

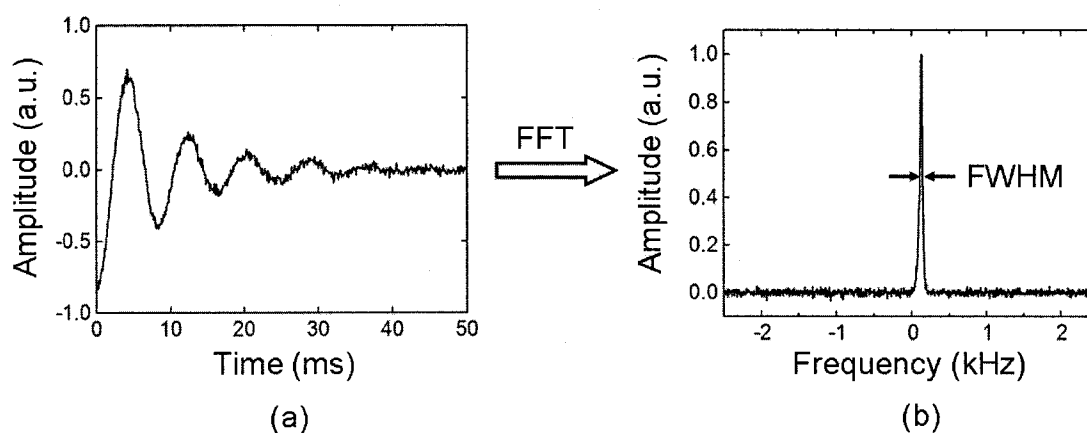


Fig. 2.6. FID signal acquisition in the presence of thermal noise. Graph (a) represents the FID signal from a H-Xe gas sample and graph (b) shows the corresponding NMR spectrum. Modulation frequency of the FID signal is equal to the 128 Hz off-resonance frequency.

Thermal noise or Johnson noise [65] is present in any NMR data acquisition. Noise induced-voltage in the NMR sample and in the coil is important for signal-to-noise ratio (SNR) calculations and it is related to the fundamental limitations of the NMR/MRI technique. The root-mean-square (r.m.s.) voltage V_{rms} generated by the thermal motion of electrons within a conductor is given by [61]:

$$V_{rms} = \sqrt{4kT\Delta f R} \quad (2.25)$$

where k is the Boltzmann constant, T is the temperature of the sample, Δf is the bandwidth of the noise considered and R is the electrical resistance of the sample.

2.3 Laser Polarization of Noble Gases

Laser polarization of noble gases refers to the increase in nuclear spin polarization level beyond the thermal equilibrium by means of optical pumping of an alkali-metal using the light generated by a laser. This process is the result of a cascade of physical phenomena. Optical pumping is the process by which the electronic spin level polarization of an alkali metal is increased via absorption of electromagnetic radiation. The first step is the optical pumping of two electronic levels of the alkali-metal atom followed by the spin-exchange between an alkali-metal atom and a noble gas atom.

The following paragraphs describe, in general terms, the processes involved in the laser polarization of xenon gas, the premise of the project presented in this thesis. More

detailed and extensive reviews of this subject are beyond the purpose of this introductory presentation and can be found elsewhere [66] [67].

The main components of a spin-exchange optical pumping system are summarized in Fig. 2.7: (i) a laser source tuneable to a wavelength $\lambda = 794.7 \text{ nm}$ (resonant absorption line of Rb), (ii) a circularly-polarized source of laser light, (iii) a glass cell containing a gas mixture of Xe, N₂ and He, (iv) a source of Rb vapour and (v) a static magnetic field B₀.

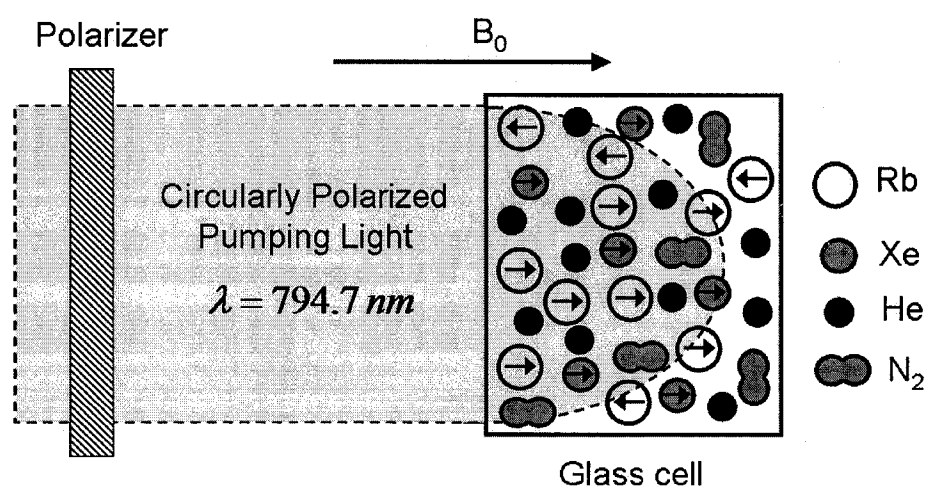


Fig. 2.7. Schematic experimental arrangement for spin-exchange optical pumping (adapted from Ref. [63]). N₂ is a quenching gas and a third body during Xe-Rb collisions while He gas is a factor in the pressure broadening of Rb absorption line.

In the most general case, optical pumping can be quite complex, especially at low pressures where the hyperfine structure of the absorption lines is well resolved [66] [67]. However, Walker and Happer [67] concluded that in almost all applications of spin-exchange optical pumping the following simplifying conditions prevail:

(a) Circularly polarized light is used to induce resonant transitions from the $^2S_{1/2}$ ground state of the alkali-metal atom to the lowest $^2P_{1/2}$ excited state.

(b) Pressure broadening of the absorption line makes the alkali-metal hyperfine structure unresolved.

(c) The quenching gas (N_2) eliminates radiation trapping as a source of relaxation.

(d) As a result of (b) and (c), the nuclear-spin polarization of the atom is conserved in the time between excitation by a pumping photon and de-excitation by a quenching collision.

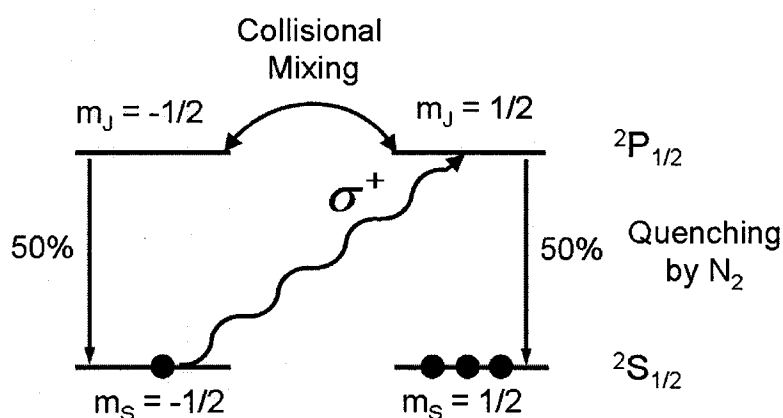


Fig. 2.8. The interaction of alkali-metal atoms with left-circularly (σ^+) polarized light (adapted from Ref. [67]).

The mechanism of spin-polarization of the alkali-metal electrons by resonant light absorption is shown in Fig. 2.8. Left-circularly polarized photons excite atoms from the spin down ($m_s = -1/2$) sublevel of the $^2S_{1/2}$ state into the spin-up ($m_j = 1/2$) of the $^2P_{1/2}$ state. Collisions with noble-gas atoms rapidly equalize the sub-level populations of the excited state [67]. Then, quenching collisions with N_2 molecules re-populate both ground-state sublevels with nearly equal probability as it is depicted in Fig. 2.8. The

balance of the angular momentum before photon absorption and after quenching leads to the result that each absorbed photon deposits a $1/2$ unit of spin angular momentum in the Rb atoms, the remainder being lost to translational motion during collisions [67].

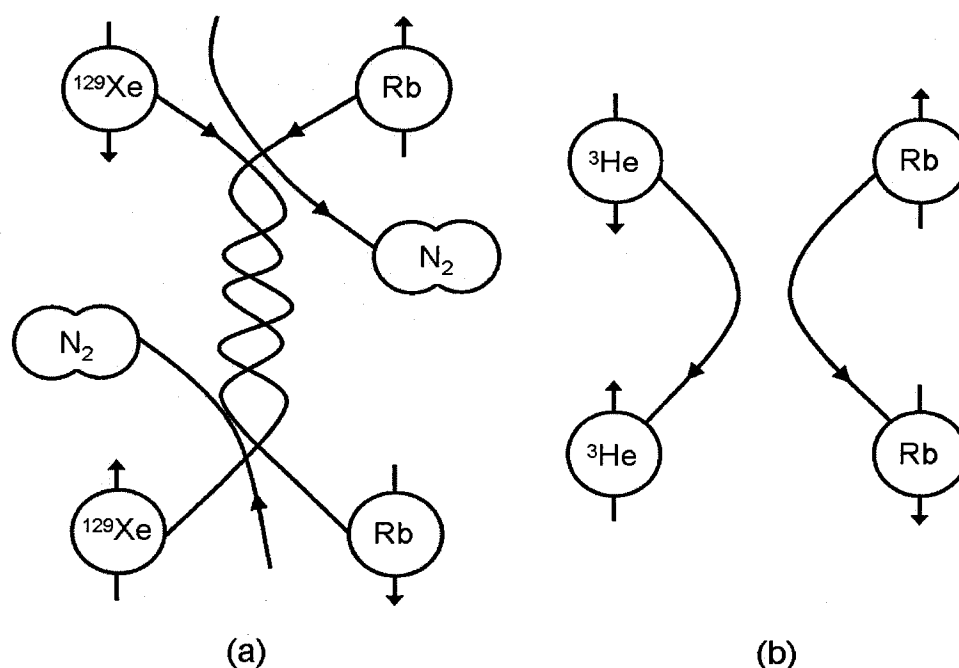


Fig. 2.9. Scheme of the two spin-exchange mechanisms: (a) formation and break-up of an alkali-metal/noble-gas van de Waals molecule and (b) binary collision between an alkali-metal atom and a noble gas atom (adapted from Ref. [67]).

The key process in spin-exchange optical pumping is collisional transfer of polarization between optically pumped alkali-metal atoms and the nuclei of the noble-gas atoms [67]. The transfer of angular momentum occurs in two cases depicted in Fig. 2.9: (a) during the time the atoms are bound in a van de Waals molecule or (b) in simple binary collisions between the atoms. For ^3He , binary conditions dominate the spin relaxation while for heavier noble gases like xenon at low gas pressures (few tens of Torr), the contributions of van der Waals molecules can greatly exceed the contribution

of binary collisions. At high gas pressure (few atmospheres) of interest for practical spin-exchange optical pumping, the lifetime of the van der Waals molecules is too short for the spin-exchange process to occur. In this case, binary collisions dominate the spin transfer [67].

Two practical modalities for producing H-Xe have been developed: (i) the batch system and (ii) the continuous-flow system [68]. Using the batch system production of small quantities of H-Xe with spin polarization approaching 70% have been reported [68]. With different continuous-flow setups ^{129}Xe spin polarizations on the order of 2-20% have been achieved [68].

2.4 NMR with Hyperpolarized Noble Gases

Hyperpolarization of nuclear spins leads to a non-equilibrium longitudinal magnetization in a static magnetic field. This means that after an RF excitation the initial longitudinal magnetization can not be recovered. Longitudinal relaxation mathematically expressed by Eq. (2.17) describes a return to the thermal equilibrium magnetization. However, the equilibrium magnetization is negligible compared to the initial magnetization of the hyperpolarized state and, for most practical pulse sequence designs, the corresponding signal is below noise level, hence, not useful.

These dynamics are different from conventional NMR/MRI where the thermal magnetization is the only one available for producing MR signals. The main disadvantage is that the time-frame of any experiment with hyperpolarized noble gases is limited by the

longitudinal relaxation time (typically seconds – minutes). Also, any repetition of the experiments using 90° RF pulses implies the existence of readily available sources of hyperpolarized gas. This difficulty has been overcome by the design of hyperpolarized gas continuous-flow systems [68].

Using a simple iteration technique, the remaining longitudinal magnetization $M_z(n)$ after the n -th pulse in a train of equally spaced pulses of the same flip angle α , is given by [69]:

$$M_z(n) = M_0 [\cos(\alpha)]^n \exp\left(-\frac{nTR}{T_1}\right) \quad (2.25)$$

where M_0 is the initial magnetization, TR is the time between pulses and T_1 is the longitudinal relaxation time. Patyal *et al.* [69] showed that this relationship can be used to estimate both T_1 and α , either in a single experiment or in a set of two separate experiments.

In general, in NMR experiments using hyperpolarized substances, small flip angles are chosen for probing the sample. In experiments involving the flow of spins, the optimal value of the tip angle in terms of preserving or cancelling the initial magnetization M_0 , depends on the specific conditions of the flow (i.e. flow velocity) as it has been theoretically shown by Gao *et al.* [70].

3. Radial Diffusive Exchange Model

3.1. Introduction

Hyperpolarized ^{129}Xe (H-Xe) gas dissolved in PFOB emulsions is not confined to the PFOB droplets. At equilibrium, H-Xe atoms can diffuse in and out the droplets into the surrounding media crossing the phospholipid (EYP) membrane. The chemical shift between the Larmor resonant frequencies of H-Xe dissolved in water and in PFOB is 1890 Hz at a static magnetic field of 1.89 T. Given this large frequency separation, the diffusive motion of H-Xe spins has a measurable effect on the linewidths of the H-Xe NMR spectrum. In the NMR literature these effects are attributed to a process generally known as *chemical exchange*. For a complete assessment of the possible use of H-Xe dissolved in PFOB emulsions as an MR contrast agent, it is important to quantify this effect in terms of all the physical parameters involved in this process.

In this chapter, a theoretical model suitable for the description of diffusive exchange of H-Xe in PFOB emulsions is presented. This work is based on a manuscript accepted for publication in the Journal of Chemical Physics [71]. The model is general; it works under a wide set of physical conditions and is not limited to the modeling of H-Xe dissolved in PFOB emulsions spectra. It can serve to provide quantitative analysis of other NMR applications where diffusive exchange of spins between two spherically concentric compartments is considered a good approximation (eg. spherical emulsion droplets in solvent).

3.2. Two-Compartment Radial Diffusive Exchange Model

The effects of chemical exchange between two compartments with different relaxation times and different resonant frequencies on NMR lineshapes [72]-[76] can be determined using the Bloch-McConnell equations [76]. In this formalism, the exchange of magnetization between the compartments is accounted for by adding terms to the usual Bloch equations to include exchange rate constants. The exchange rates are the inverse of the average residence times of the spins in each of the two compartments. While this is reasonable for systems exhibiting chemical exchange (i.e. chemical reactions), it is not appropriate if the exchange process does not occur instantaneously. The approximation of chemical exchange is reasonable when the exchange time is very short (<1 ms) compared to the relaxation times in each compartment (fast exchange), but it fails to accurately describe the effects of exchange on the spectra when the compartment sizes are large compared to the diffusive pathlength on the NMR time scale (diffusion-limited exchange). This is expected to occur in such systems as porous media, tissues and large droplet (>1 μm) emulsions. In this case, Belton and Hills [77] have shown that the Bloch-Torrey equations [78] (or generalized Bloch equations) explicitly incorporating the diffusion equation more accurately describe the effects of diffusive exchange on the NMR lineshapes.

The first to include spin diffusion in the analysis of transverse relaxation decay were Brownstein and Tarr [79]. They used simple surface relaxation and the generalized Bloch equations to explain the observed multiexponential decay of NMR signal in the studies of cells. Their model was based on a single compartment with the wall serving as

an infinite relaxation “sink”. Later, Belton and Hills [80] underlined the importance of morphology and restricted diffusion in a more realistic description of the exchange process using a two-compartment model with a membrane, applied to one-dimensional lamellar systems. A detailed analysis of the diffusive exchange of spins in systems between two compartments separated by a spherical interface probed by pulsed-field NMR has also been reported by Price *et al.* [81].

In this work, a theoretical diffusive exchange model is developed based on a spherical two-compartment system with a separating membrane between the compartments using the generalized Bloch equations. The dependence of NMR lineshapes on the spin diffusive motion determinants (droplet size/dilution, diffusion coefficients and membrane permeability) and relaxation properties (transverse relaxation times) of this two-compartment system is determined analytically.

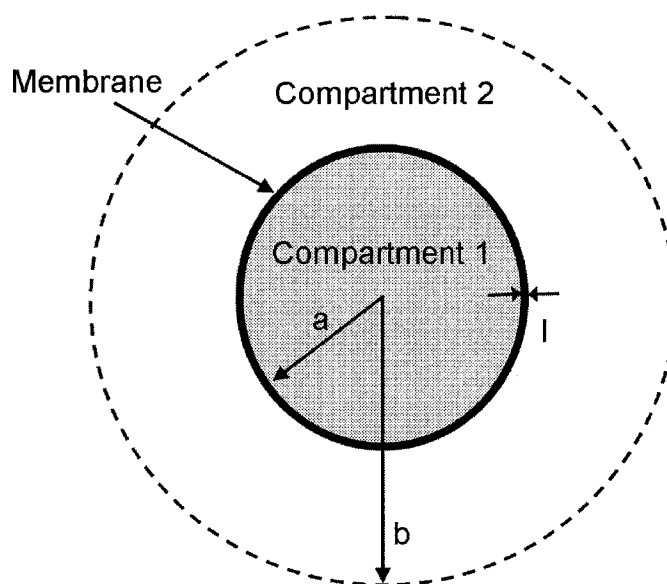


Fig. 3.1 Two-spherical concentric compartment geometry used for the radial diffusive exchange model. The compartments are separated by a membrane of thickness l .

The radial diffusive exchange system used in the theoretical model is shown in Fig. 3.1. The PFOB emulsion can be modeled by a unit cell composed of a spherical PFOB droplet (compartment 1) surrounded by a concentric shell of water (compartment 2). In this case, the radius (a) for this unit cell represents the volume-weighted average diameter of the PFOB droplet size distribution of the entire emulsion. The unit cell radius b is determined based on the radius a and the water volume dilution. The compartments are separated by a membrane of permeability (κ). The exact application of the model to the case of H-Xe dissolved in PFOB emulsion spectra and the detailed experimental data reduction, are presented in the next chapter.

The theory presented below follows the work of Belton and Hills [80] suitably modified for a finite spherical geometry and different solubility of spins in the two media of the compartments.

In general, the transverse magnetization depends on time and spatial coordinates. For this theory, isotropic diffusion is assumed. That is, in spherical coordinates (r, θ, φ), magnetization M does not depend on the polar angle θ , or the azimuthal angle φ $\left(\frac{\partial M}{\partial \theta} = 0 \text{ and } \frac{\partial M}{\partial \varphi} = 0 \right)$.

Using complex notation, the generalized equation for the transverse magnetization including diffusion, is:

$$\frac{\partial M}{\partial t} = -i \cdot \omega_0 \cdot M - \gamma \cdot M + D \cdot \frac{1}{r} \cdot \frac{\partial^2}{\partial r^2} (r \cdot M). \quad (3.1)$$

In this equation, r represents the radius, ω_0 is the Larmor resonant frequency, M is the complex transverse magnetization, γ is the transverse relaxation rate ($1/T_2^*$) in the absence of diffusive exchange and D is the diffusion coefficient of the spins.

Equation (3.1) can be solved using the Laplace Transform [77] [82]:

$$D \cdot \frac{1}{r} \cdot \frac{\partial^2}{\partial r^2} (\tilde{M} \cdot r) - \alpha \cdot \tilde{M} = -M_0 \quad (3.2)$$

where: $\alpha = s + i \cdot \omega_0 + \gamma$; ($s = -i \cdot \omega$), ω is the Laplace transform angular frequency variable, M_0 is the initial transverse magnetization and \tilde{M} is the Laplace transform of M and depends on radius, r , and complex frequency s ; ($s = -i \cdot \omega$).

For $r = 0$, Eq. (3.2) has a singularity. Therefore, one must apply the condition that $\tilde{M}(r, s)$ and its derivative $\frac{\partial \tilde{M}(r, s)}{\partial r}$ be finite (or bounded) at $r = 0$. Using the notations in Fig. 3.1 where subscript 1 represents the droplet compartment and subscript 2 represents the second compartment surrounding the droplet, the corresponding equations for the transverse magnetization in these two sites are:

$$D_1 \cdot \frac{1}{r} \cdot \frac{\partial^2}{\partial r^2} (\tilde{M}_1 \cdot r) - \alpha_1 \cdot \tilde{M}_1 = -M_{01}, \quad r \in [0, a] \quad (3.3)$$

and

$$D_2 \cdot \frac{1}{r} \cdot \frac{\partial^2}{\partial r^2} (\tilde{M}_2 \cdot r) - \alpha_2 \cdot \tilde{M}_2 = -M_{02}, \quad r \in [a, b]. \quad (3.4)$$

At the interface between compartments (the membrane), the continuity of spin flux is expected. The flux can be written as the product of the diffusion coefficient for the compartment (D_1 or D_2) and the magnetization gradient at the interface. The flux can also be expressed as the product of the membrane permeability (κ) and the magnetization difference across the membrane since the thickness of the membrane ($\sim \text{nm}$) is much smaller than the diffusion pathlength within the transverse relaxation time scale ($\sim \mu\text{m}$). The magnetization difference across the membrane at any time is calculated by taking

into account the difference in solubility of the spin particles in the media of the two compartments. Accounting for this difference, the fluxes between the membrane and compartment 1 can be equated:

$$D_1 \cdot \left(\frac{\partial \tilde{M}_1}{\partial r} \right)_{r=a} = \kappa \cdot [\beta \cdot \tilde{M}_2(a) - \tilde{M}_1(a)]. \quad (3.5)$$

Similarly, at the interface between the membrane and compartment 2:

$$D_2 \cdot \left(\frac{\partial \tilde{M}_2}{\partial r} \right)_{r=a} = \kappa \cdot [\beta \cdot \tilde{M}_2(a) - \tilde{M}_1(a)] \quad (3.6)$$

where β represents the solubility ratio between compartments (see Appendix B).

The boundary condition imposed on $M_1(r)$ at $r = 0$ gives the following equation:

$$\left(\frac{\partial \tilde{M}_1}{\partial r} \right)_{r=0} = 0. \quad (3.7)$$

Also, at the geometrical boundary, $r = b$, the net flux is zero,

$$\left(\frac{\partial \tilde{M}_2}{\partial r} \right)_{r=b} = 0. \quad (3.8)$$

Equations (3.5)-(3.8) represent all the boundary conditions necessary to solve the differential equations (3.3) and (3.4). The solution that forms the complex signal can be found using the usual methods for boundary-value problems [82]. The mathematical details are given in Appendix A and Appendix B. Only the final results are quoted here.

The complex signal $S(s)$ expression can be divided in two parts: a non-exchange part $N(s)$ and an exchange part $E(s)$.

$$S(s) = N(s) + E(s) \quad (3.9)$$

$$N(s) = \frac{\mu_1 \cdot a}{\xi_1^2} \cdot V_1 + \frac{\mu_2 \cdot (b-a)}{\xi_2^2} \cdot V_2 \quad (3.10)$$

$$E(s) = 4 \cdot \pi \cdot \left[q_1 \cdot \int_0^a r^2 \cdot u_1(r, s) \cdot dr + q_2 \cdot \int_a^b r^2 \cdot u_2(r, s) \cdot dr \right] \quad (3.11)$$

The real part of function $N(s)$ from Eq. (3.10) gives two Lorentzian-shaped lines centered on the resonant frequencies: ω_1 and ω_2 . Their linewidths expressed as FWHM are related to the transverse relaxation times in each compartment via Eq. (2.23) from the previous chapter. The real part of the function $E(s)$ from Eq. (3.11) includes the diffusive exchange contributions to the transverse relaxation. Step-by-step calculations of $\text{Re}[E(s)]$ are not shown, but analytical expressions for these quantities can be determined algebraically and are shown in Appendix B. The NMR spectrum is then given by:

$$P(\omega) = \frac{\text{Re}[S(s)]}{2 \cdot \pi \cdot |M_0|}. \quad (3.12)$$

3.3. Methods

The generality of the model described in the previous section of this chapter can be tested using a set of numerical values of the physical parameters that shape the NMR spectrum expressed in Eq. (3.12). Theoretical spectra were generated using a C++ code which incorporated the equations from Appendix A and Appendix B. The FWHM of the spectra were estimated using quadratic and linear interpolations of the point grid used for plotting the theoretical spectra.

For a given two-compartment system such as depicted in Fig. 3.1., there are two factors that modulate the exchange of spins between the two compartments: (i) a

diffusive motion factor which is composed of the diffusion coefficients of the two media (D_1 and D_2) and the compartments sizes (a and b radii) and (ii) the membrane permeability (κ). A set of values for diffusion coefficients, compartment sizes, membrane permeability as well as transverse relaxation rates and chemical shifts can be chosen to illustrate different situations (see Figs. 3.2 and 3.3).

The parameters used to generate the spectra are shown in Table 3.1. The geometrical parameters corresponding to equal volumes of the compartments: $V_1 = V_2$, are: $a = 1 \mu\text{m}$ and $b = 1.26 \mu\text{m}$. No solubility difference between the compartments was selected (solubility ratio $\beta = 1$). The frequency separation was chosen to be 1000 Hz.

Compartment #	Diffusion coefficient ($10^{-9} \text{ m}^2/\text{s}$)	T_2 (ms)	Compartment volume (μm^3)
1	4	100	4.19
2	2	50	4.19

Table 3.1. Parameters used for the simulation of the theoretical spectra.

A point grid with 1 Hz frequency resolution was generated using a C++ code incorporating all the equations from Appendix A and Appendix B. The spectra were plotted using Origin 5.0 (MicroCal, Northampton, MA, USA).

3.4. Results and Discussion

The exchange regimes for a two-site spin system have been discussed by Allerhand and Gutowsky [74] using a general approach based on Bloch-McConnell equations [76]. They identified three exchange regimes based on the frequency separation (Δf), exchange time (τ) and relative spin populations of the two sites (P_1 and P_2). These are: (i) slow exchange regime [$1/\tau < 2(P_1 P_2)^{1/2} \Delta f$], (ii) intermediate exchange regime [$1/\tau = 2(P_1 P_2)^{1/2} \Delta f$] and (iii) fast exchange regime [$1/\tau > 2(P_1 P_2)^{1/2} \Delta f$].

In graphs (a), (b) and (c) from Fig. 3.2, the peaks corresponding to the two compartments can be distinguished. This is the regime of slow exchange or intermediate exchange. The last two graphs (d) and (e) from Fig. 3.2 show a single peak spectrum, an indicator of the fast exchange regime.

Further physical insight can be gained by analyzing the departures from the pure Lorentzian shapes which can be noticed in graphs (b) and (c) in Fig. 3.2. The effect is more visible as the exchange contribution increases with increasing membrane permeability. In the case of diffusive exchange, transverse relaxation can no longer be described by a simple exponential decay as the one expressed in Eq. (2. 19). Additional transverse relaxation corresponding to the diffusive exchange of spins between the two compartments has to be taken into account.

The exchange regimes can also be defined in the frequency domain. Figure 3.3 shows the plot of the total linewidth (expressed as FWHM) dependence on the membrane permeability. The parameters used are the same as the ones used to generate the graphs in

Fig. 3.2. For this set of parameters, five orders of magnitude of the membrane permeability are seen to be sufficient to describe the full range of the exchange regimes.

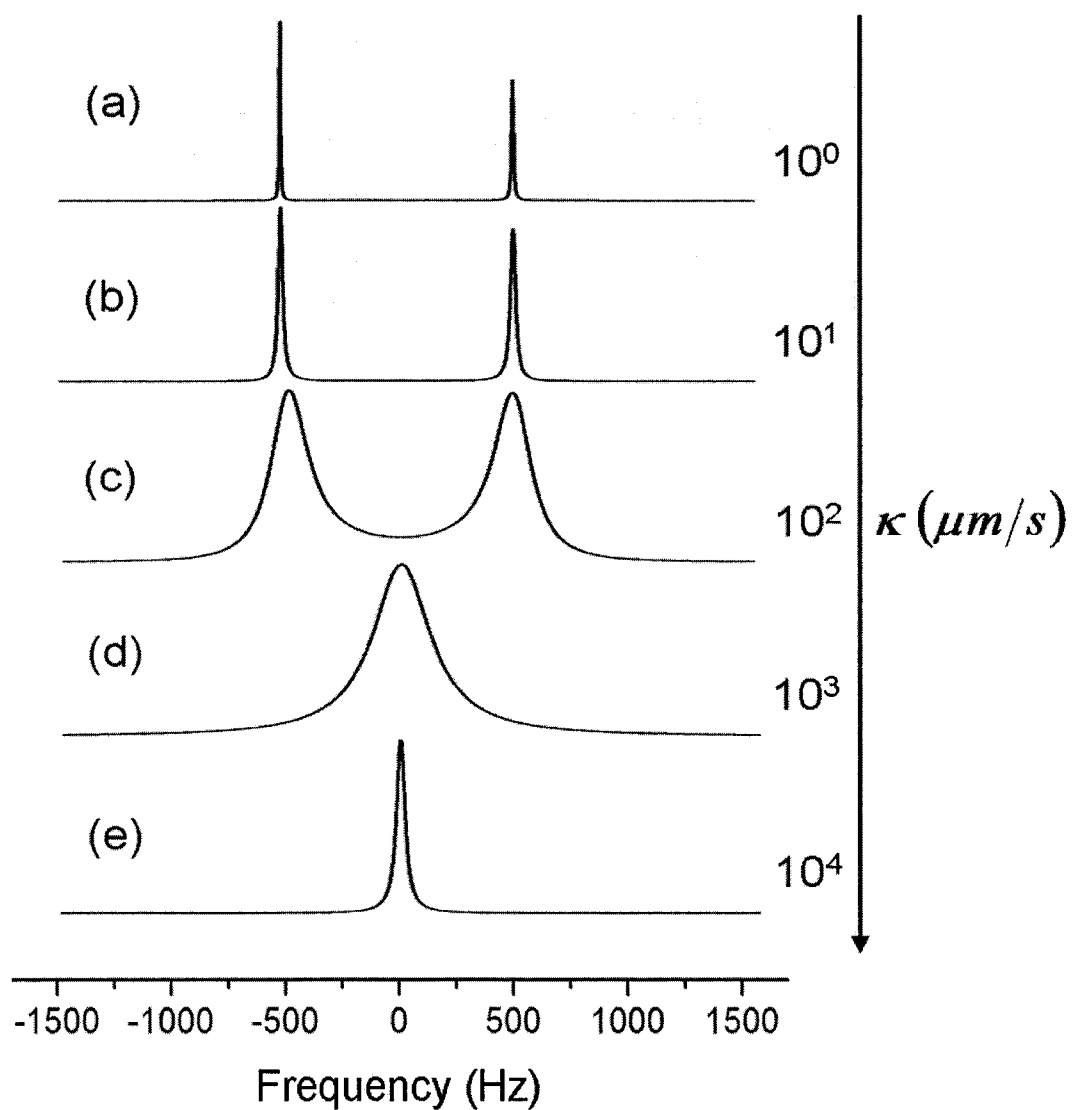


Fig. 3.2. Theoretical NMR spectra of spins undergoing diffusive exchange between two spherical concentric compartments. Different permeabilities of the separating membrane correspond to different exchange regimes of the spins. The frequency separation between resonant frequencies in the two compartments is $\Delta f = 1000 \text{ Hz}$.

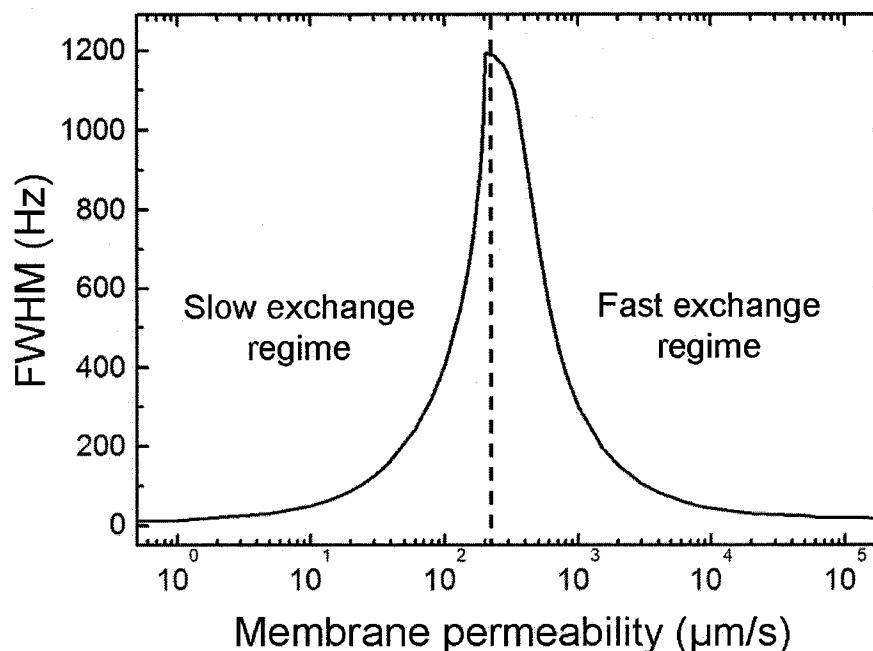


Fig. 3.3. Semi-logarithmic plot of the sum of resonance peaks FWHM as a function of membrane permeability. Dashed vertical line represents the maximum of the sum of FWHM values for the two resonance peaks.

Visual inspection of the dependence leads to an *ad-hoc* criterion of the exchange regimes which can be stated as it follows. The maximum of the curve represents the intermediate exchange limit, while the slow and fast exchange regimes lie to the left and to the right of this limit respectively. According to this criterion, for fast exchange regimes, the resonance peaks can no longer be distinguished. The tails of the curve correspond to the very slow and very fast exchange regimes.

In the limit of slow exchange, the total transverse magnetization decay can be separated into relaxation of two transverse magnetizations precessing at the resonant frequencies of the two sites. In this regime, the additional term which contributes to the

transverse magnetization loss is given by the spins diffusing out of the compartment. Hence, the total transverse relaxation rate can be written as follows:

$$\gamma_i^e = \gamma_i + \tau_i^{-1} \quad (3.13)$$

where γ^e corresponds to the transverse relaxation rate in the presence of exchange, γ represents the transverse relaxation rate without exchange, τ is the average resident time of the spins in the compartment and lower index i designates the compartment. This relationship is equivalent to the result of Allerhand and Gutowsky [74] for equal relaxation rates of the two sites ($\gamma_1 = \gamma_2$) and equal relative populations ($P_1 = P_2 = 0.5$).

At equilibrium, the net flux of particles across the separating membrane is zero. In this case, the exchange time (τ) can be computed given the residence time in the compartments (τ_1 and τ_2) [72]:

$$\frac{1}{\tau} = \frac{1}{\tau_1} + \frac{1}{\tau_2} . \quad (3.14)$$

Equation (2.24) from Chapter 2 can be used to estimate the transverse relaxation rate using the *FWHM* of the resonance peak:

$$\gamma = \pi \text{FWHM} . \quad (3.15)$$

Combining Eqs. (3.13), (3.14) and (3.15), allows estimation of the exchange times for any given set of the physical parameters previously mentioned. Figure 3.4 shows the dependence of the spin exchange rate ($1/\tau$) on membrane permeability for the same parameters used to generate the graphs from Fig. 3.2. For low permeabilities of the separating membrane, an expected linear increase of exchange rate with membrane permeability is obtained. For higher permeabilities, a deviation from the linear relationship can be noticed. The physical assumption behind Eq. (3.13) is no longer valid

as the limit of intermediate exchange regime is approached. In this case of equal populations ($P_1 = P_2$), the intermediate exchange limit of Allerhand and Gutowsky [74] corresponds to: $1/\tau = 1ms^{-1}$.

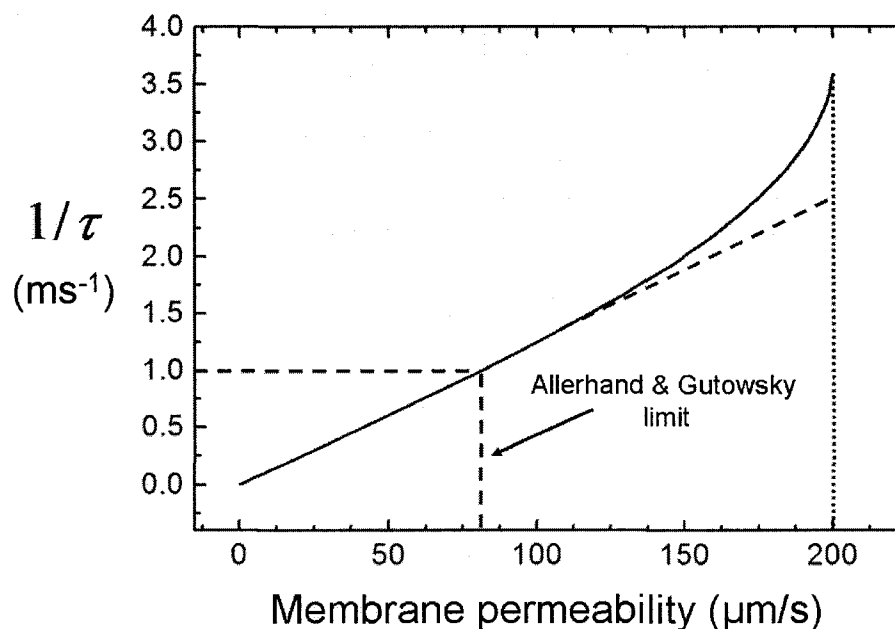


Fig. 3.4. Plot of the exchange rate ($1/\tau$) dependence on the membrane permeability (κ). Vertical dotted line (right) corresponds to the maximum sum of FWHM values of the two peaks and the vertical dashed line (left) shows the Allerhand and Gutowsky [74] limit between slow and fast exchange regimes.

For intermediate and fast exchange regimes, the exchange rate is high enough that transverse magnetization transfer between the compartments dominates the transverse relaxation and Eq. (3.13) no longer holds. The dependence of the lineshape on the dynamic parameters is complicated and given by the real part of function $E(s)$ described by Eq. (3.11). The final expression is too complicated to be given in a single equation. The elementary functions which describe the dependence are explicitly given in Appendix B.

In the slow exchange regime in which Eq. (3.13) is valid, the dependence of the residence times (τ_1 and τ_2) on the geometrical parameters (a and b) can be investigated.

The results are shown in Fig. 3.5.

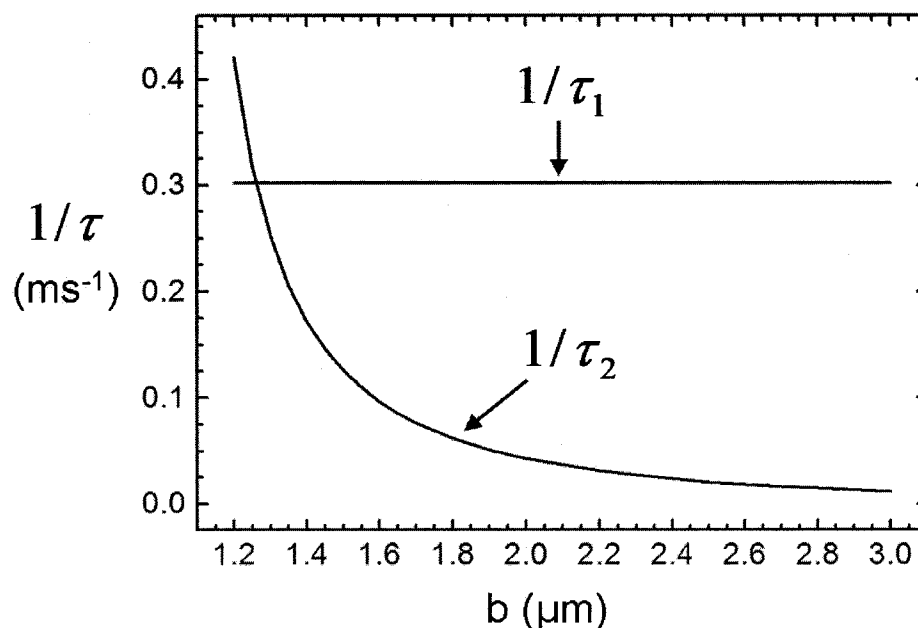


Fig. 3.5. Plot of inverse residence times ($1/\tau_1$ and $1/\tau_2$) as a function of radius b for constant radius $a = 1 \mu\text{m}$.

To generate the graph in Fig. 3.5, a membrane permeability of $50 \mu\text{m/s}$ was chosen and the rest of the parameters used were the same as for the previous graphs. This choice assured the slow exchange regime and Eq. (3.13) could be used.

It can be noticed that the residence time of spins in compartment 1 (τ_1) remains constant with b as it is expected while the residence time in compartment 2 (τ_2) increases with increasing b . The intersection point of the two curves represents the point of equal relative populations ($P_1 = P_2 = 0.5$). This is also the point of equal volumes of the

compartments ($V_1 = V_2$) since the spin particle solubility in the compartments was considered to be equal ($\beta = 1$).

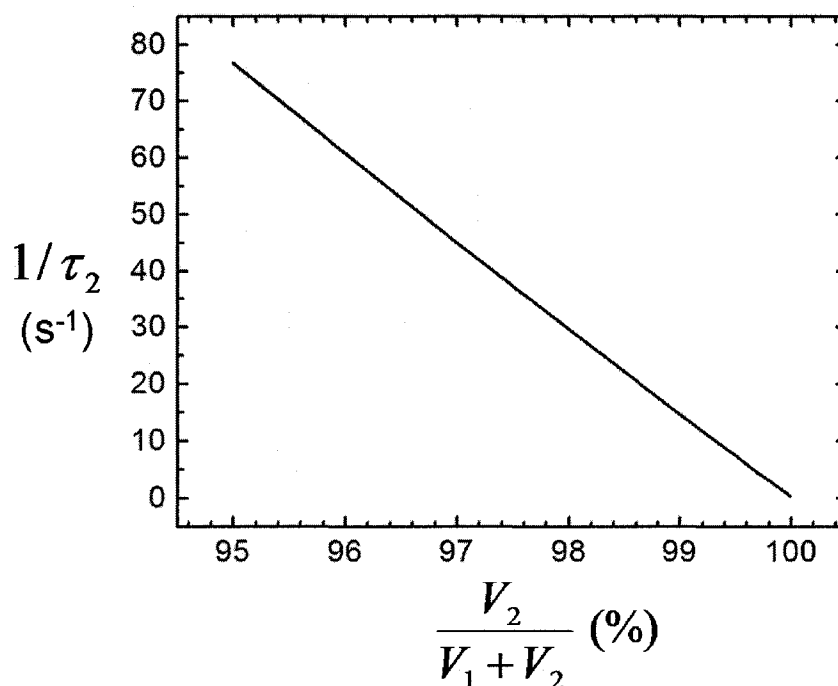


Fig. 3.6. Plot of the inverse residence time $1/\tau_2$ as a function of volume ratio $V_2/(V_1 + V_2)$. The expected vanishing value for high volume ratios can also be seen.

Using the same parameters, but different values for outer diameter b , the plot in Fig. 3.6 of $1/\tau_2$ versus relative volume ratio $V_2/(V_1 + V_2)$ shows a linear dependence between the two parameters and the expected vanishing value of the transfer rate with increasing volume. Similar behavior is expected for the exchange rate $1/\tau$ in the limit of increasing the size of one compartment and decreasing the size of the other.

At equilibrium, the following relationship between relative solubility (β), relative population ratio (P_1/P_2), residence time ratio (τ_1/τ_2) and volumes ratio (V_1/V_2) holds [50] [73]:

$$\frac{P_1}{P_2} = \beta \frac{V_1}{V_2} = \frac{\tau_1}{\tau_2}. \quad (3.16)$$

In the slow exchange regime, the residence times can be calculated using Eq. (3.13). The relationship expressed by Eq. (3.16) is illustrated in Fig. 3.6. The constant parameters used were: $\kappa = 50 \mu\text{m}/\text{s}$ and $a = 1 \mu\text{m}$. The outer radius b was varied to maintain the slow exchange regime and validity of (Eq. 3.13). Its value is related to the volume ratio (V_1/V_2) and radius a according to the following equation based on the spherical volume formula (see Eqs. (A.17) and (A.18) from Appendix A):

$$b = a \left(1 + \frac{V_1}{V_2} \right)^{1/3}. \quad (3.17)$$

The residence times (τ_1 and τ_2) were estimated using Eqs. (3.13) and (3.15).

The average residence time of a diffusing particle within a sphere $\langle t \rangle$ can be calculated from basic diffusion theory using the following relationship [83]:

$$\langle t \rangle = \frac{d^2}{15D} \quad (3.18)$$

where d is the sphere's diameter and D is the diffusion coefficient of the particle within the sphere.

Using Eq. (3.18), the probability of particles crossing the separating membrane, p , can be estimated as the ratio between the residence time within the sphere with no outer boundary restriction $\langle t \rangle$ and the residence time within the sphere with a separating membrane restricting the diffusion τ_1 [50]:

$$p = \langle t \rangle / \tau_1. \quad (3.19)$$

The plot of this probability as a function of membrane permeability in the slow exchange range is shown in Fig. 3.7. The same set of parameters used for Fig. 3.4 represents the input necessary to generate the FWHM values for the two peaks. Eqs. (3.13) and (3.15) were also used to calculate τ_1 .

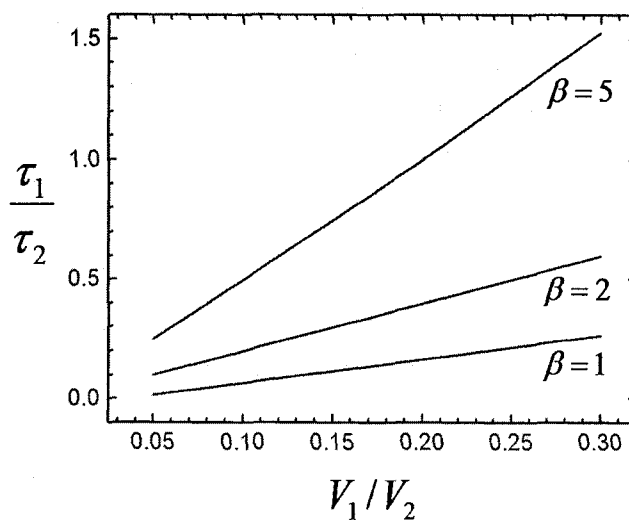


Fig. 3.7. Plot of residence time ratio (τ_1/τ_2) versus compartment volume ratio (V_1/V_2) for three different values of relative solubility β . Predicted linear dependence of Eq. (3.16) is obtained. The slope of the lines is equal to β .

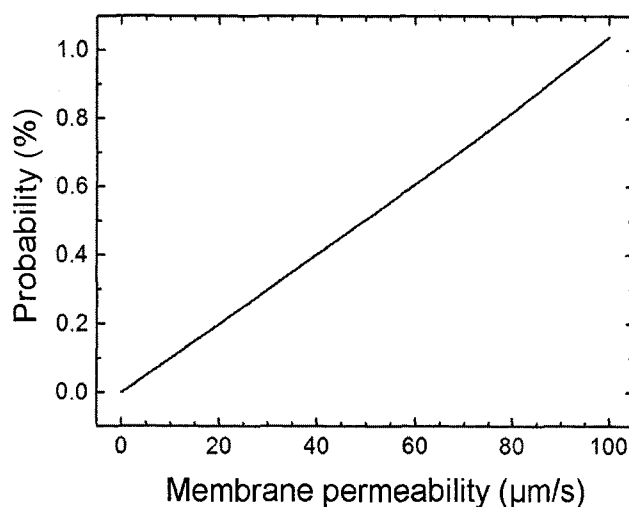


Fig. 3.8. Plot of the spin particle probability to cross the membrane as a function of permeability. The expected linear relationship is obtained.

3.5. Conclusions

In this chapter a general diffusive exchange model in radial geometry was developed. The generalized Bloch equations and boundary conditions incorporate spin diffusion and the usual transverse relaxation. The problem was solved in the frequency domain. The result is a generalized theory which predicts the NMR spectra for any set of parameters which define the system.

The theoretical model accommodates all the exchange regimes previously defined in the literature and permits a practical criterion for identifying the exchange regimes for any two-compartment radial diffusive exchange system simply based on the degree of separation between the peaks.

For the slow exchange regime, a simplifying assumption permits estimation of residence times of the spin particles within each compartment. It is also shown that, in this regime, knowledge of the diffusion coefficient of spins within the inner spherical compartment, its radius, FWHM of the exchange spectra and non-exchange transverse relaxation rates is sufficient to calculate the probability of spin particles crossing the membrane. This provides the theoretical framework for the analysis of the experimental results which now follow.

4. H-Xe Spectroscopy in PFOB Emulsions and Blood

4.1. Introduction

The diffusive motion of xenon between the PFOB droplet and the surrounding media shapes the observed NMR spectra. The purpose of the spectroscopy experiments described in this chapter was to apply the theoretical model presented in detail in the previous chapter to the study of the NMR spectra of xenon dissolved in PFOB emulsions.

The experimental procedures used in the acquisition of NMR spectra with H-Xe are described. Two different NMR spectroscopy-type experiments with H-Xe were performed. The first set of experiments involved the acquisition of spectra of H-Xe dissolved in PFOB emulsions at different water dilutions. The results presented in this part are included in a manuscript accepted for publication in *Journal of Chemical Physics* [71]. In the second part, spectra of H-Xe dissolved in a mix of blood and PFOB emulsion for three different blood volume dilutions are analysed.

The water dilutions of the PFOB emulsion experiments enable estimation of the unknown parameters that control the diffusive motion of xenon in such emulsions, namely the egg-yolk phospholipid (EYP) membrane permeability and the volume-weighted diameter of the emulsion. This was achieved by fitting the theoretical model to the experimental dilution linewidth data using the diffusion coefficients of xenon in water and PFOB published in the literature. The permeability of the EYP membrane and the

average diameter are found. Using basic pore theory, the diffusion coefficient within the membrane pores is also estimated.

4.2. NMR Spectroscopy of H-Xe Dissolved in PFOB Emulsions

4.2.1. Materials and Methods

A relatively large droplet emulsion (average volume-weighted diameter of approximately 4.6 μm) was prepared from 2.6 ml PFOB (Sigma-Aldrich, St. Louis, MO, USA), 2.9 ml distilled water and 46 mg egg yolk phospholipid (EYP, Sigma-Aldrich, St. Louis, MO, USA). The suspension was emulsified using a VirSonic 60 sonicator at a power setting of 10 for approximately 45 seconds. The samples were aged for 24 hours at 20°C in order to increase their average diameter [50]. This procedure yielded a PFOB emulsion containing 47% PFOB and 53% water by volume. The density of the EYP was calculated to be 1.018 g/cm^3 (this gives a phospholipid volume of only 0.045 cm^3 , hence, the EYP volume is negligible [84]).

Emulsion droplets were sized using a Horiba LA-920 Laser Scattering Particle Size Distribution Analyzer (Irvine CA). Droplet size distribution measurements using the light scattering analyzer are shown in Fig. 4.1. The volume-weighted average diameter corresponding to the distribution was 4.6 μm and standard deviation was 2.1 μm . The longer tail of the distribution towards larger values of PFOB droplet diameter is a consequence of the aging process during which the diameter of the droplets increases to

minimize the Gibbs free energy associated with the interfacial tension between the continuous and the dispersed phases [85].

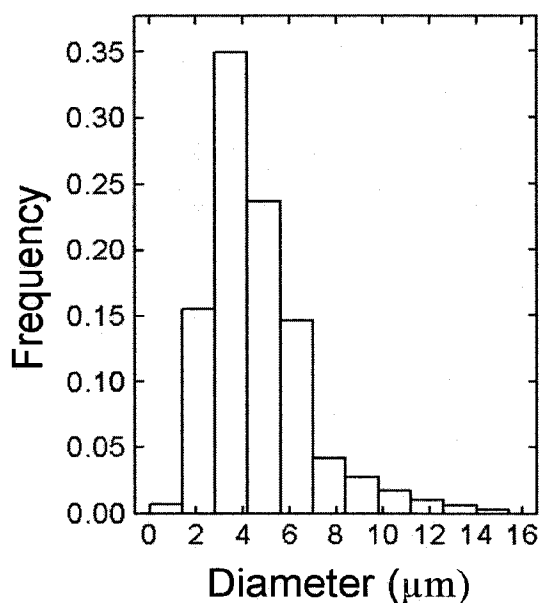


Fig. 4.1. Normalized histogram of the PFOB emulsion droplet diameter. Bin frequencies represent weights by volume measured by the laser scattering particle size distribution analyzer. The corresponding volume-weighted mean droplet diameter is $4.6 \mu\text{m}$ and the standard deviation is $2.1 \mu\text{m}$.

For the water dilution experiments, it was important to start the dilution from a single batch of non-diluted emulsion (53% water by volume). The use of different batches of emulsions introduces bias into the final results and increases the overall experimental uncertainty. The reason behind this limitation is that different batches have different volume weighted average diameters. The dilutions were made starting with the stock emulsion (47%), V , to be added to an initial volume and consecutively diluted by adding water in precise pre-calculated aliquots. The volume of water V to be added in a volume V_0 of PFOB emulsion of c_0 % water volume dilution to obtain a volume $(V+V_0)$

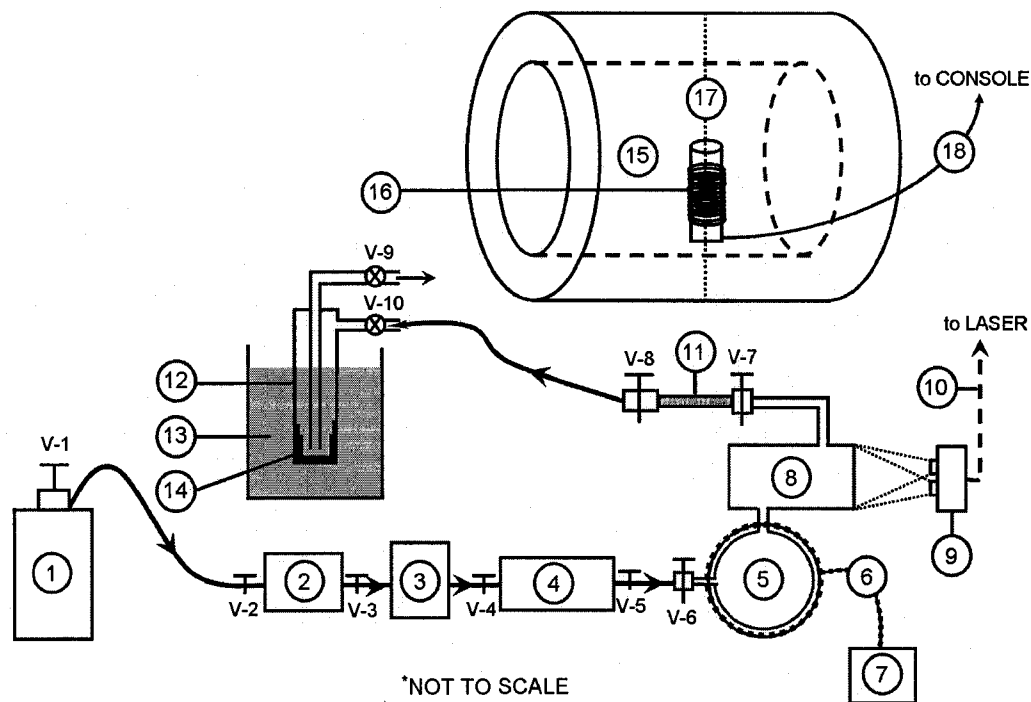
of PFOB emulsion of c % water volume dilution, can be calculated using the following equation:

$$V = \frac{c - c_0}{100 - c} V_0. \quad (4.1)$$

Cryotrapped hyperpolarized ^{129}Xe (H-Xe) from the flow system (Fig. 4.2) was expanded into a 3 cm^3 syringe containing 1.5 ml of the diluted PFOB emulsion. The average spin polarization of the xenon gas used in experiments was approximately 10%. Polarization measurements were performed by comparison with the thermal signal from a precise volume of naturally abundant xenon gas enclosed in a sealed glass cell [86]. The sample was then shaken vigorously for 3-4 seconds and the excess gas was carefully expelled. NMR spectra were obtained from the sample in the syringe.

The NMR measurements were obtained using a 1.89 T, 30 cm horizontal bore superconducting magnet (Magnex, Abingdon UK), controlled by an MRRS MR5000 console (Surrey UK). Samples of six different water dilutions of the PFOB emulsion were placed inside a 1 cm diameter solenoid coil tuned to the xenon resonance frequency (22.18 MHz). A 90° pulse with a length of $20 \mu\text{s}$ was applied for the excitation of the xenon dissolved in the PFOB emulsion. The carrier frequency of the pulses was set at 150 ppm with respect to the xenon gas peak (0 ppm) between the water peak and the PFOB peak. The spectral width was set at 10 kHz with a 4096 sample point array that gave a total time of 400 ms for the data acquisition.

The NMR spectra were analyzed using the MRRS Specana software (MRRS MR5000, Surrey, UK). The signal-to-noise ratio (SNR) of the acquired spectra (defined as the ratio between maximum peak intensity and noise standard deviation [87]) varied from 45 to 150.



LEGEND

1 – Xe GAS CYLINDER (1% Xe, 10% N_2 , 89 % He)	10 – FIBER OPTIC TO LASER CELL
2 – H_2O trap	11 – Rb TRAP
3 – FLOW METER	12 – Xe TRAP
4 – O_2 TRAP	13 – LIQUID NITROGEN / WARM WATER
5 – Rb CELL	14 – Xe ICE
6 – THERMOCUPLE AND HEATING WIRES	15 – 1.89 T MAGNET
7 – TEMPERATURE CONTROLLER	16 – SOLENOID COIL
8 – OPTICAL PUMPING CELL	17 – ISOCENTER POSITION
9 – POLARIZER AND LENSES	18 – SOLENOID COIL OUTPUT

Fig. 4.2. Schematic of the ^{129}Xe polarization flow system and H-Xe cryo-trapping method.

A fit of the experimental spectra with the theoretical model developed in Chapter 3 was performed using a C++ code which computed the deviations from the FWHM values of the experimental spectra (i.e. χ^2 minimization method). The two unknown parameters - the average droplet diameter and the EYP membrane permeability - were varied in small steps to find the minimum of the χ^2 function.

Following the notations described in Chapter 3 and Fig. 3.1, the PFOB emulsion was modeled by a unit cell composed of a spherical PFOB droplet (compartment 1) surrounded by a concentric shell of water (compartment 2). In this theoretical treatment, it was assumed that a single unit cell is representative of all the droplets in the entire volume of emulsion. The droplet radius a for this unit cell represents the volume-weighted average radius of the droplet size. The unit cell radius b was determined based on the radius a and the outer media volume dilution using Eq. (3.17) from Chapter 3. The other parameters for xenon in water and PFOB required for the diffusive exchange model were: (i) the diffusion coefficients (D), (ii) the measured transverse relaxation rates (γ) and (iii) the Ostwald solubility which is defined as the volume of gas that can be absorbed by a unit volume of solvent. The values for (i) and (iii) were extracted from the literature and are summarized in Table 4.1. Values for (ii) were measured experimentally from lineshape analysis of spectra of H-Xe dissolved in pure water and pure PFOB respectively.

	D ($10^{-9} \text{ m}^2 \text{ s}^{-1}$)	γ (s^{-1})	Xenon Ostwald solubility
Water	2.2 ± 0.4	15.7	0.11
PFOB	4.5 ± 0.6	22.0	1.2

Table 4.1. Diffusion coefficients (D) [88], transverse relaxation rates (γ) and Ostwald solubility ($T = 37^\circ\text{C}$, $p = 1 \text{ atm}$) of xenon in water and PFOB [39].

4.2.2. Results and Discussion

The linewidths of xenon dissolved in pure water and pure PFOB were found to be 5.4 Hz and 6.9 Hz respectively. The corresponding relaxation rates used in the theoretical modeling of the lineshapes are listed in Table 4.1. The chemical shift between xenon dissolved in PFOB and xenon dissolved in water was measured to be 1890 Hz at the magnetic field strength used here (1.89 T).

Figure 4.3 shows an example of a typical set of experimental spectra acquired for different water dilutions while Fig. 4.4 shows the corresponding theoretical spectra generated with the best fit parameters of the model and parameters in Table 4.1. A strong similarity between the experimental lineshapes can be observed; not just in terms of linewidth, which is seen in graphs from Fig. 4.4, but also in terms of relative intensities of the two peaks.

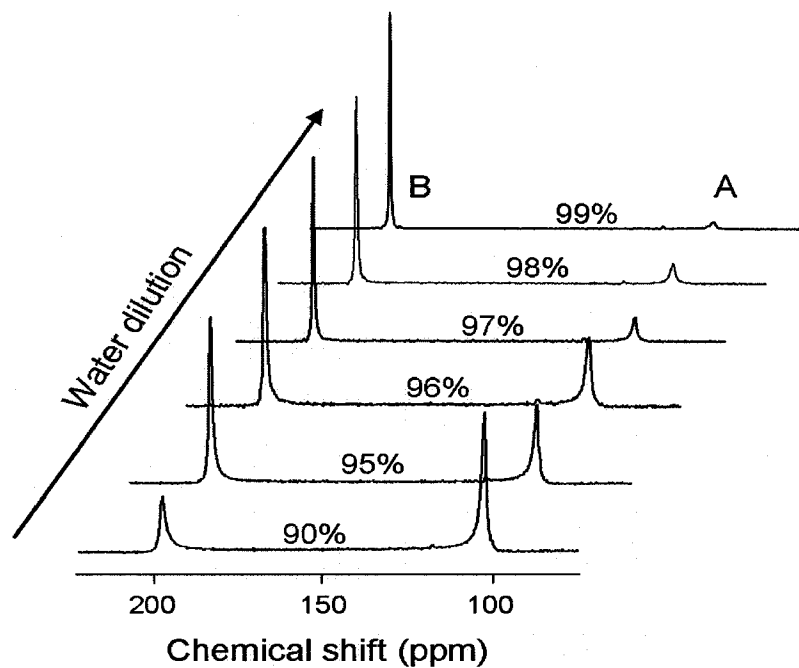


Fig. 4.3. Experimental NMR spectra of xenon dissolved in the PFOB emulsion for different water dilutions expressed as volume percentage ratio. For each spectrum, peak A corresponds to xenon in PFOB and peak B corresponds to xenon in water.

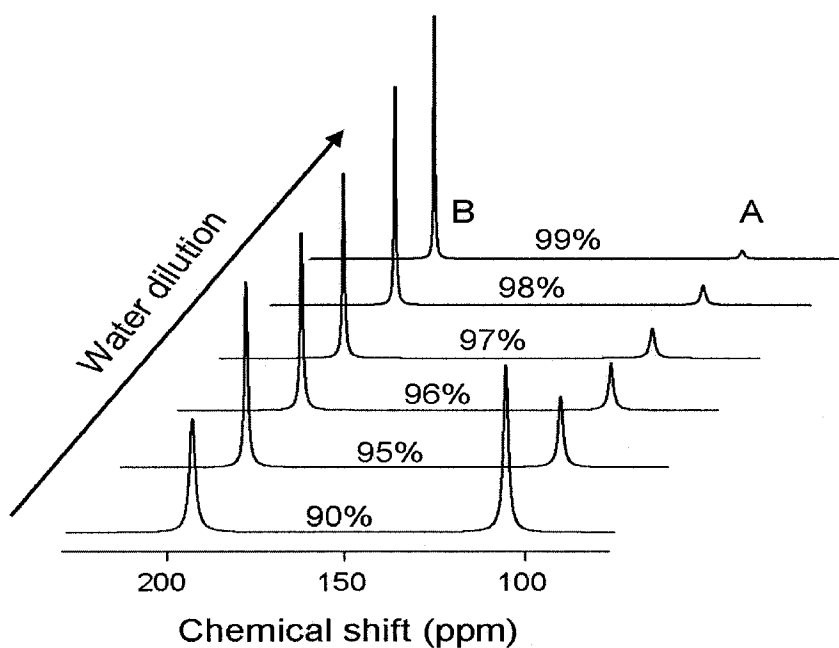


Fig. 4.4. Theoretical NMR spectra of xenon dissolved in the PFOB emulsion for different water dilutions expressed as volume percentage ratio. For each spectrum, peak A corresponds to xenon in PFOB and peak B corresponds to xenon in water.

Figures 4.5 and 4.6 show, in detail, the results of the fit of the theoretical spectra linewidths to the experimental spectra of xenon dissolved in the PFOB emulsions at different water dilutions. Figure 4.5 (a) shows a strong decrease in the water peak linewidth with increasing water dilution. The increase in the residence time of xenon in water diminishes the effect of the exchange process on the water peak, so that for very large water dilutions the xenon water peak converges to the pure water xenon linewidth as expected. This corresponds to a progressive transition from the slow exchange regime to very slow exchange regime. In graph (b) from Fig. 4.5, the FWHM of the PFOB peak does not depend on the dilution confirming that the average diameter of the PFOB droplet of the starting batch of emulsion remains constant during the time of data acquisition (approx. 2-3 hrs.).

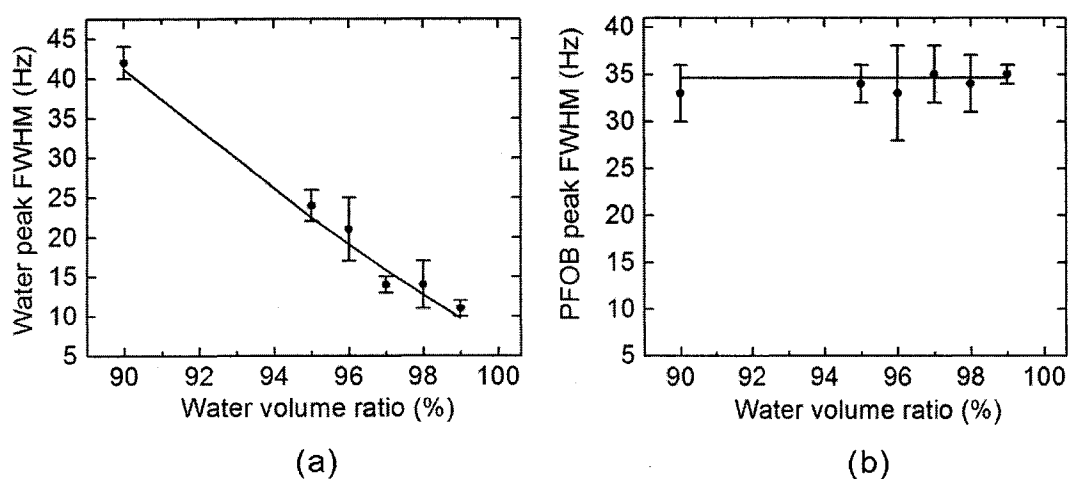


Fig. 4.5. FWHM of the (a) water peak and (b) the PFOB peak for six water dilutions of the PFOB emulsion. The solid line represents the best fit of the theoretical model to the data points. The error bars represent standard deviations based on three repeated experiments. The chi-square per number of degrees of freedom is 0.6.

For the best fit values in Fig. 4.5, the average diameter of the PFOB droplet was found to be $(3.5 \pm 0.8) \mu\text{m}$ which is within one standard deviation of the volume-weighted average diameter of $(4.6 \pm 2.1) \mu\text{m}$ obtained using light scattering. The value of the EYP membrane permeability for xenon was found to be $(58 \pm 14) \mu\text{m/s}$ which is of the same order of magnitude as the reported water permeability of red blood cells (RBC) of $21.5 \mu\text{m/s}$ [89]. This is consistent with the range of diffusion coefficients of water expected in biological media $(1.0\text{-}2.5) \times 10^{-9} \text{ m}^2/\text{s}$ which are relatively close to the values of xenon diffusion coefficients in water and PFOB measured by Wolber *et al.* [88] (see Table 4.1). This suggests that the diffusion behaviour of xenon in the PFOB emulsion resembles the behaviour of water in biological media, in agreement with the generally accepted view that xenon is freely diffusible in biological media [39].

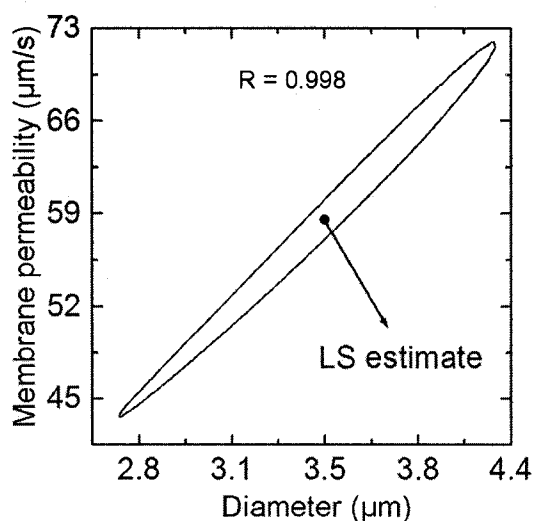


Fig. 4.6. Plot of the one standard deviation ellipse of the two-parameter fit of the FWHM of the PFOB and water peaks. The least-squares (LS) estimates of the volume-weighted average droplet diameter and the membrane permeability, respectively, were: $d = (3.45 \pm 0.80) \mu\text{m}$ and $\kappa = (58 \pm 14) \mu\text{m/s}$. The correlation coefficient, R , between the two measured parameters was found to be 0.998 which indicates a strong correlation.

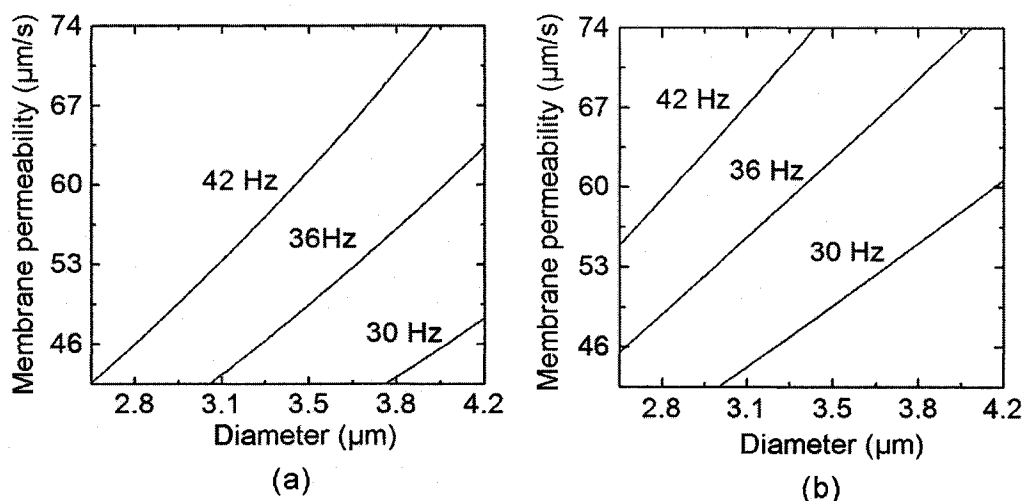


Fig. 4.7. Plot of theoretical FWHM for different diameters and membrane permeabilities. Three constant linewidths corresponding to the water peak (a) and the PFOB peak (b) at 90% water volume dilution of the PFOB emulsion are shown.

The diameter and the permeability of the membrane were found to be positively correlated with a correlation coefficient $R = 0.998$ (Fig. 4.6). This was calculated using the analytical equation of the covariance ellipse [90] and two arbitrary points on the ellipse curve. This strong correlation indicates that identical spectra can only be obtained if the droplet size and the permeability increase (or decrease) simultaneously.

In Fig. 4.7 the theoretical dependence of diameter and membrane permeability are plotted for three different values of the water peak linewidths (Fig. 4.7a) and PFOB peak (Fig. 4.7b) at 90% water volume dilution. The positive slope of the curves is a consequence of the correlation shown in Fig. 4.6 and indicates that both the PFOB droplet size and the EYP membrane antagonistically regulate the diffusive exchange of xenon between the compartments for a constant water dilution.

Based on the discussion from Chapter 3, slow exchange of xenon between PFOB and water compartments was found to determine the spectra shown in Fig. 4.3. In this

regime, equations (3.13), (3.15) can be used to determine the residence time τ_1 within the PFOB droplet. Using the best estimates shown in Fig. 4.6 and the corresponding FWHM of the PFOB peak, τ_1 was found to be 10.8 ms.

Similarly, the residence time of xenon in the water compartment can be calculated for different water dilutions. For example, in the case of 90% water dilution of the PFOB emulsion ($V_1/V_2 = 1/9$), the average residence time of xenon in water, τ_2 , is calculated to be 9.3 ms. The ratio $\frac{\tau_1/\tau_2}{V_1/V_2}$ equals 10.4 which is comparable to the xenon Ostwald solubility ratio $\beta = 10.9$ between PFOB and water calculated from the last column of Table 4.1.

For the water volume dilution range of the experimental spectra shown in Fig. 4.3 (90%-99%), the plot of τ_1/τ_2 versus V_1/V_2 is shown in Fig. 4.8. Best-fit parameters from Fig. 4.5 were used to compute the residence times: τ_1 and τ_2 . The slope of 10.6 represents the theoretical estimate of the xenon solubility ratio β between PFOB and water.

Equations (3.18) and (3.19) from Chapter 3 can be used to estimate the probability p of xenon atoms crossing the EYP monolayer. This was determined to be 1.6% which is equal to that calculated by Wolber *et al.* [50] in this type of emulsion using residence time estimates based on Bloch-McConnell equations and xenon solubility values in water and in PFOB. The equivalent statement is that, on average, from 1000 xenon atoms encountering the EYP membrane only 16 cross into the other compartment.

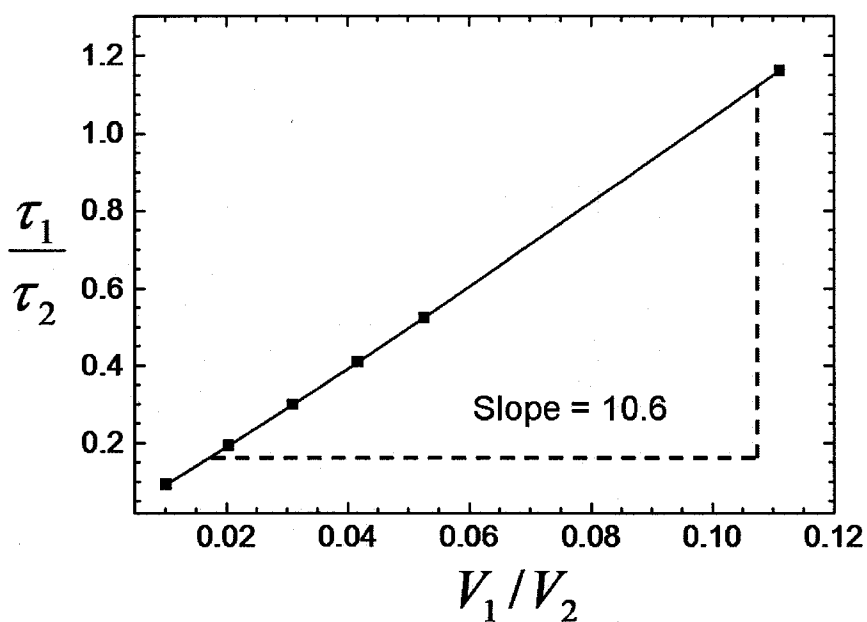


Fig. 4.8. Plot of residence time ratio of xenon in PFOB and water versus volume ratio between the two substances in the PFOB emulsion for the range 90% to 99% water volume dilution. The slope of 10.6 represents xenon solubility ratio between PFOB and water.

Further insight into the EYP membrane properties can be gained using the definition of membrane permeability (κ) which takes into account the porosity of the membrane [91]:

$$\kappa = \frac{\text{porosity } D_m}{l} \quad (4.2)$$

This equation is based on the microscopic treatment of particle transport across membranes. The underlying assumption is that particles cross the membrane by passage through its pores and nowhere else. In Eq. (4.2), D_m is the diffusion coefficient of particles within the pores of the membrane and l represents the thickness of the membrane.

The thickness of the EYP membrane l has been estimated to be 2.1 nm based on its density (1.018 g/cm^3), molecular weight of EYP (776 g/mol), and surface density ($61 \text{ \AA}^2/\text{molecule}$) [84]. The porosity can be considered to be equal to the probability of xenon atoms crossing the membrane. Using these values and the best estimates of membrane permeability and volume-weighted diameter, Eq. (4.2) gives the diffusion coefficient of xenon within the pores of the EYP monolayer as approximately $2.1 \times 10^{-11} \text{ m}^2/\text{s}$. This value is two orders of magnitude smaller than the diffusion coefficient of xenon in water or in PFOB, indicating that motion of xenon atoms in the EYP pores is significantly slower than diffusion in water or PFOB. Combined with the relatively low porosity, this diffusion coefficient explains the slow exchange regime measured in the experimental spectra (Fig. 4.3).

4.3. NMR Spectroscopy of H-Xe Dissolved in Mixtures of PFOB Emulsions and Blood

4.3.1. Materials and Methods

Measurements of H-Xe dissolved in PFOB emulsion and blood involved, in most part, the same experimental procedures described in the previous section: PFOB emulsion preparation, H-Xe cryogenic trapping and NMR spectra acquisition. The main difference was that blood dilutions of the PFOB emulsion and blood mixture were not prepared before dissolving the H-Xe gas. As shown in Fig. 4.9a, to simulate an actual *in vivo* injection, the trapped H-Xe was released into the syringe containing the desired volume of undiluted PFOB emulsion (47% volume PFOB). The syringe was then shaken for 3-4 seconds until H-Xe was completely dissolved in the PFOB emulsion. After that, the mixture of H-Xe and emulsion is transferred into a second syringe containing the appropriate volume of blood to give the desired final blood volume dilution as is depicted in Fig. 4.9b. Before the insertion of the mixture into the coil, the syringe was shaken one more time for 2-3 seconds (Fig. 4.9c).

Three blood volume dilution experiments were performed (33%, 50% and 67%) with the total volume of the mixtures of blood and PFOB emulsion constant at 1.5 ml. This permitted the use of the entire sensitive volume of the solenoid coil. The average polarization of the H-Xe gas from the flow system was around 5%.

The NMR settings were as it follows: spectral width 10 kHz, block size 2048 points and the carrier frequency set between the PFOB and the water xenon resonances, at 150 ppm with respect to the reference xenon gas peak. The RF pulse flip angle (15°) was calibrated using the method of Patyal *et al.* [69]. MRRS Specana software was used to analyze the spectra.

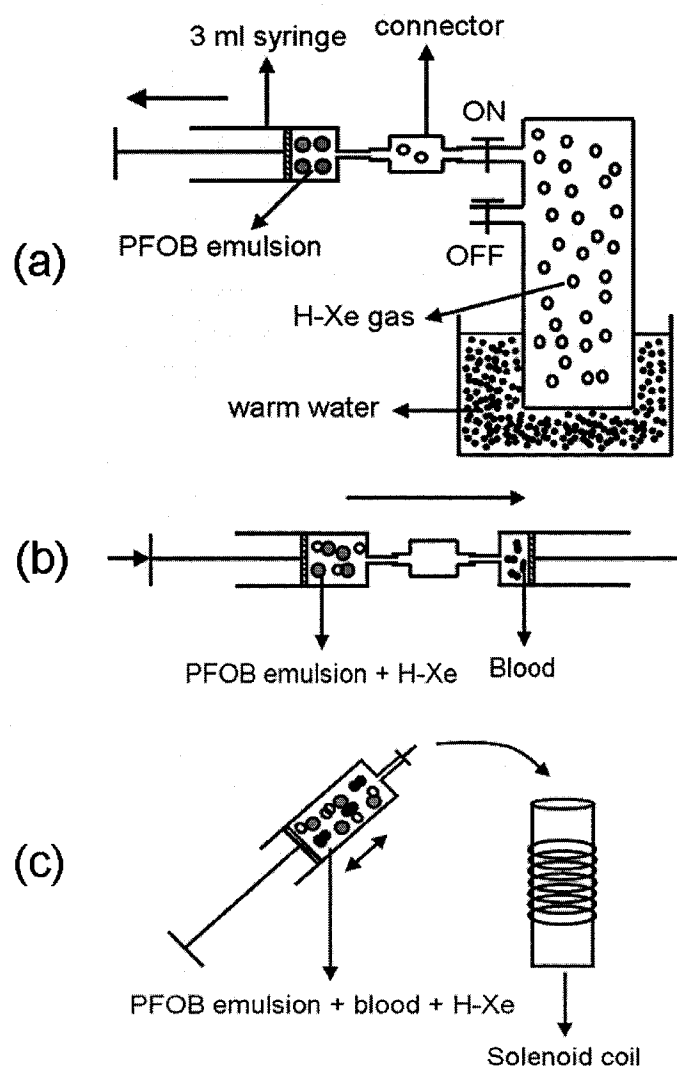


Fig. 4.9. The main experimental steps (a), (b) and (c) for acquiring NMR spectra from H-Xe dissolved in mixtures of blood and PFOB emulsion.

4.3.2. Results and Discussion

Figure 4.10 shows a sample of experimental spectra of H-Xe dissolved in PFOB emulsions and blood for the three dilutions. Peak B (~ 100 ppm) corresponds to the H-Xe dissolved in the PFOB droplets. Peak A (~192 ppm) corresponds to the resonance frequency of H-Xe dissolved in plasma [45]. The decrease in the MR signal which can be observed with increasing blood concentration can be explained by the low solubility of xenon in blood compared to PFOB.

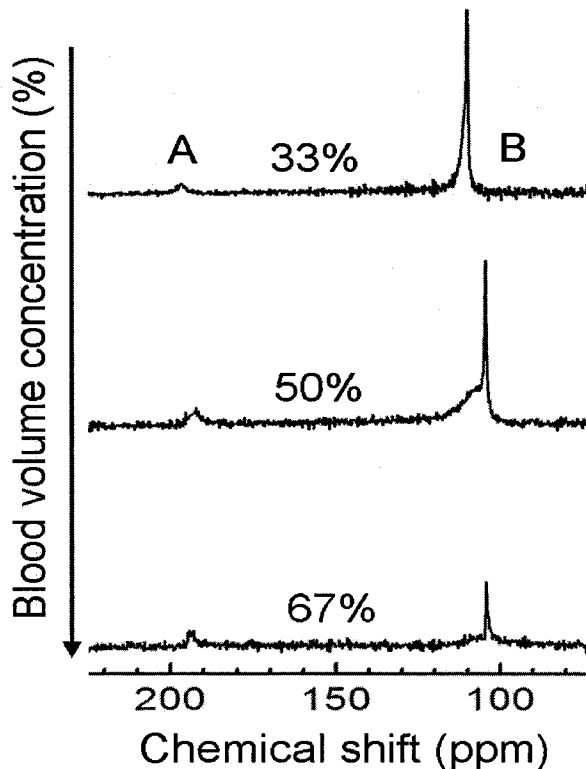


Fig. 4.10. Plots of typical experimental spectra of H-Xe dissolved in mixtures of PFOB emulsion and blood for three blood volume concentrations. Peak A represents the resonance peak from H-Xe dissolved in blood and water mixture and peak B is the peak from H-Xe dissolved in PFOB droplets (the reference frequency for the chemical shift scale is with respect to the gas peak at 0 ppm).

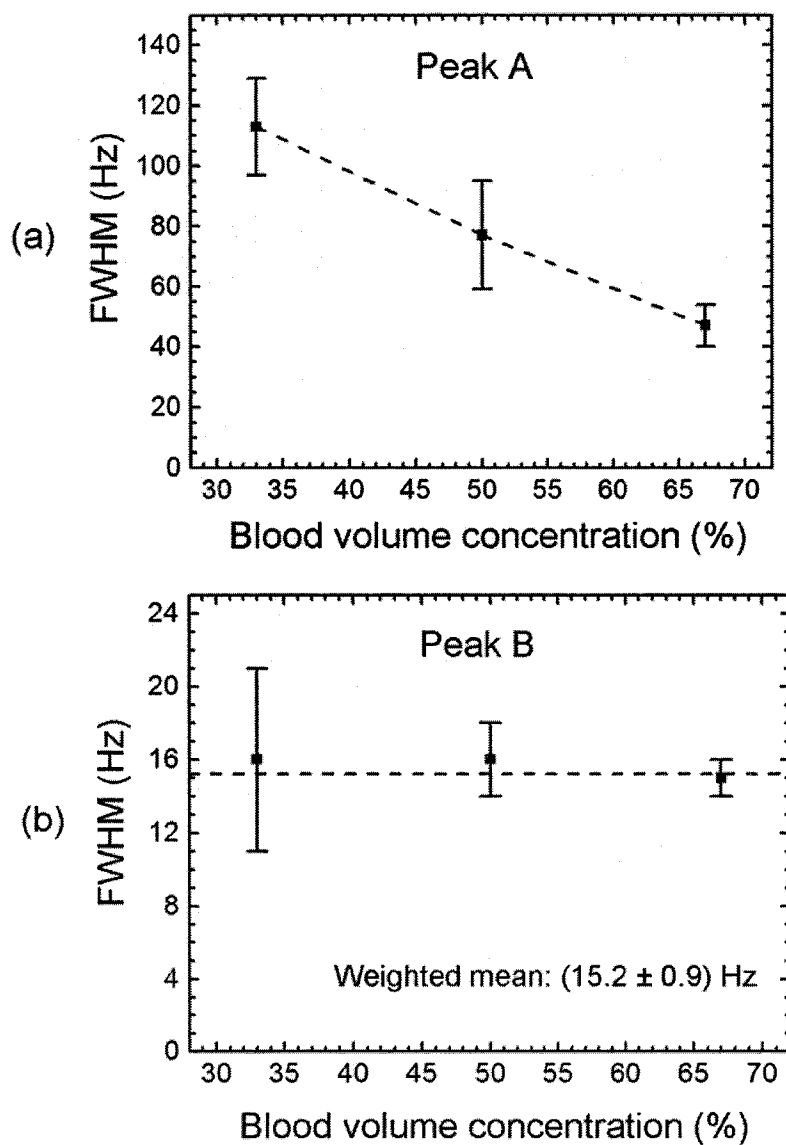


Fig. 4.11. Plot of FWHM of the experimental peaks A and B corresponding to H-Xe dissolved in water/blood mixture and PFOB, respectively. The error bars represent the standard deviation of three repeated experiments. The dashed line in graph (b) from the figure represents the weighted mean of the combined measurements for the three blood volume concentrations.

Figure 4.11 shows the plots of FWHM as function of blood volume concentration for the two observed peaks which correspond to H-Xe dissolved in the blood/water mixture (peak A) and H-Xe dissolved in PFOB (peak B) respectively. The expected decrease in the blood/water peak linewidth with increasing blood volume due to the transition to very slow exchange was obtained. The PFOB linewidth was constant on average for all three dilutions. The large error bars are due to low SNR of the spectra and the use of different emulsion batches during the experiments.

This is the same trend as was observed for the water peak of H-Xe dissolved in various water dilutions of the PFOB emulsion (see Fig. 4.5). This means that it should be possible to establish a relationship between blood volume concentration and FWHM of H-Xe in plasma peak. For a given PFOB emulsion, this relationship implies linewidth measurements similar to the ones in Fig. 4.11.

Further insight can be gained if the slow exchange approximation which was described in Chapter 3 is used. The experimental NMR spectra shown in Fig. 4.10 arise from slow exchange of H-Xe spins between the PFOB droplet compartment and blood/water volume. In this regime, Eqs. (3.13 – 3.16) can be applied. The transverse relaxation rate of H-Xe in PFOB from Table 4.1 and the average weighted mean of the linewidth of the PFOB peak from Fig. 4.10 can be used in Eqs. (3.13) and (3.15) to calculate the average residence time of H-Xe spins in PFOB droplets: $\tau_1 = (32.0 \pm 2.8)$ ms. Hence, the average exchange rate can be found if the residence time in the plasma/water volume τ_2 is estimated. Because the water volume is changing with PFOB emulsion concentration, the transverse relaxation rate in this site, γ_2 , is not

constant for different blood volume concentrations and the procedure used for τ_1 cannot be applied to calculate τ_2 .

The residence time τ_2 can be found using the relative H-Xe population ratio P_1/P_2 in the two compartments and Eq. (3.16). P_1/P_2 can be estimated using xenon Ostwald solubility values for water (S_w), PFOB (S_{PFOB}) and blood (S_{blood}), along with the initial PFOB volume concentration in the injected emulsion (c_0) and blood volume dilution (c):

$$\frac{P_1}{P_2} = \frac{S_{PFOB} c_0 (1-c)}{S_w (1-c_0) + S_{blood} c}. \quad (4.3)$$

The values of xenon Ostwald solubility for xenon in water (S_w) and in PFOB (S_{PFOB}) are given in Table 4.1. The solubility of xenon in blood (S_{blood}) has been reported to be 0.14 at $T = 37^\circ C$ and atmospheric pressure $p = 1 atm$ [39]. Further, Eq. (3.14) gives the final expression of the exchange rate as function of relative population ratio (P_1/P_2) and residence time in PFOB droplets, τ_1 :

$$\frac{1}{\tau} = \frac{1}{\tau_1} \left(1 + \frac{P_1}{P_2} \right). \quad (4.4)$$

The results of exchange rate ($1/\tau$) calculations for all three blood volume dilutions ($c = 0.33, 0.50$ and 0.67) are shown in Fig. 4.11. A linear dependence was found similar to the general case shown in Fig. 3.6 from Chapter 3. For very high blood volume concentration, the exchange rate vanishes as it is expected. This confirms the validity of using the slow exchange approximation equations to estimate the exchange rate of H-Xe in PFOB emulsions and blood.

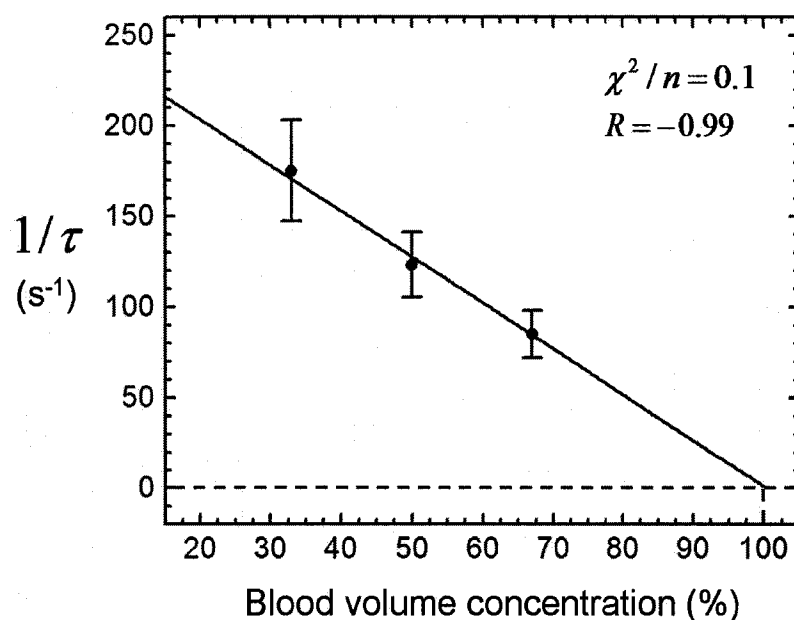


Fig. 4.12. Graph of exchange rate ($1/\tau$) as a function of blood volume concentration. Expected linear dependence is observed. The solid line represents the linear fit of the estimated values. The exchange rate vanishes when blood concentration approaches the maximum concentration of blood as expected. Error bars were calculated using error propagation from the uncertainties on the FWHM of the observed PFOB peak.

4.4. Conclusions

In this chapter, NMR spectra of H-Xe dissolved in different water volume concentrations PFOB emulsions were analyzed using the theoretical model developed in the previous chapter. Using previously measured parameters of xenon in water and PFOB, full characterization of PFOB emulsions stabilized with EYP was possible.

Fitting the FWHM of the experimental spectra with the theoretical FWHM, the permeability of the EYP monolayer and the average droplet diameter were estimated. A

relative porosity of 1.6% of the EYP membrane was found and the diffusion coefficient of xenon inside the membrane's pores was calculated to be approximately $2.1 \times 10^{-11} \text{ m}^2/\text{s}$.

Experiments with H-Xe dissolved in PFOB emulsions mixed with blood showed that the linewidth of the spectra can be used to estimate blood concentration. Relatively large separation between PFOB and blood peaks (~90 ppm) (Fig. 4.10) confirms that slow exchange of xenon describes the observed experimental spectra. Using the slow exchange approximation from Chapter 3, the exchange rate was calculated for the three blood volume concentrations and a linear dependence with blood volume concentration was obtained. Extrapolating the linear behaviour to higher blood volume concentrations, the vanishing exchange rate in the case of the pure blood sample was also confirmed.

5. Water Flow Experiments with H-Xe Dissolved in PFOB Emulsions

5.1. Introduction

Figure 4.5 from chapter 4 shows that the linewidth of the water peak from H-Xe dissolved in PFOB emulsions depends on the water dilution of the emulsion. This dependence was also predicted in Chapter 3 based on the model of diffusive exchange of spins in a two-compartment radial geometry where the effects on NMR spectra were theoretically investigated and equations for calculating residence times for the case of slow exchange were derived.

In this chapter, experiments involving dynamic acquisition of spectra from H-Xe dissolved in a PFOB emulsion injected into a flowing water stream are described to simulate a bolus injection *in vivo*. A volume of ~4 ml of 80% water volume PFOB emulsion in which H-Xe was dissolved was injected into a closed, continuously flowing water system.

The purpose of these experiments was to show that the relationship between water dilution of PFOB emulsions and linewidth of the H-Xe water peak can be used to measure the PFOB concentration in the flowing bolus and thereby measure flow rate. H-Xe spectra acquired with RF pulses equally spaced by 250 ms were used to estimate PFOB concentration as a function of time. The PFOB concentration-time curves and

bolus dilution theory were used to calculate water flow rate and mean transit time (MTT) of a bolus passage through a solenoid coil and verified using the known flow rate.

5.2. Theory

The lineshapes of H-Xe dissolved in PFOB emulsions are described by slow diffusive exchange kinetics as already shown in Chapter 4. In this regime, Eq. (3.13) is valid and residence times in the two sites: τ_1 and τ_2 can be determined using:

$$\tau_i = (\pi FWHM_i - \gamma_i)^{-1}. \quad (5.1)$$

In this equation, $FWHM_i$ represent the linewidth measurements of the two peaks respectively and γ_i are the transverse relaxation rates of the two compartments respectively.

Residence time ratio τ_1/τ_2 is related to compartment volume ratio V_1/V_2 and solubility ratio β via Eq. (3.16) from Chapter 3. Hence, using the residence times τ_1 and τ_2 , the volume concentration of PFOB in the emulsion $c_1 = V_1/(V_1 + V_2)$ is given by:

$$c_1 = \frac{\tau_1}{\tau_1 + \beta \tau_2}. \quad (5.2)$$

The solubility ratio of xenon between PFOB and water, β , is 10.9 [35]. Residence times in the two compartments can be estimated using the measured FWHM values for PFOB and water peaks and Eq. (5.1) for each spectrum. Using Eqs. (5.1) and (5.2), a value of PFOB volume concentration c_1 can be obtained for each spectrum. This means

PFOB concentration-time curves can be calculated in discrete time steps equal to $TR = 250$ ms.

The mean flow rate (volume/time) and mean transit time (MTT) of the bolus can be calculated using two basic relationships from bolus dilution theory [92] [93]. Flow (F) can be estimated using the Stewart-Hamilton equation which is based on the law of conservation of mass in the context of bolus dilution. Applied to the case of PFOB emulsion bolus dilution, flow is given by:

$$F = \frac{c_{10} V_0}{\int_0^{\infty} c_1(t) dt} \quad (5.3)$$

In Eq. (5.3) c_{10} represents the initial PFOB volume concentration in the injected emulsion, V_0 is the injected volume of PFOB emulsion and c_1 represents the volume concentration of PFOB in the bolus measured from FWHM of the spectra and Eqs. (5.1) and (5.2).

The mean transit time of the PFOB emulsion bolus (MTT) as a function of PFOB volume concentration-time dependence $c_1(t)$ is given by [93]:

$$MTT = \frac{\int_0^{\infty} t c_1(t) dt}{\int_0^{\infty} c_1(t) dt} \quad (5.4)$$

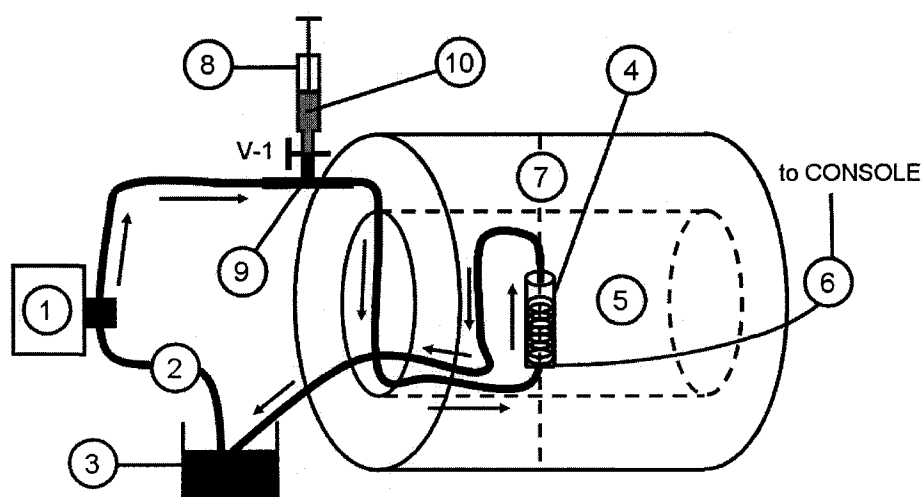
In bolus dilution theory, the volume available for the tracer is usually referred to as volume of distribution V_d . V_d can be calculated using the Central-Volume Principle [93] [94]:

$$F = \frac{V_d}{MTT} \quad (5.5)$$

5.3. Materials and Methods

5.3.1. Experimental Setup and Procedures

The main components used in these experiments were: (i) a 1 cm-diameter solenoid coil used for the experiments described in the previous chapter and (ii) a peristaltic pump (Cole-Parmer Instr., Chicago, IL, USA) which maintained a continuous flow of water in a closed loop system made of rubber hose pieces adjusted to the superconductive magnet geometry. A scheme of this arrangement is shown in Fig. 5.1.



* NOT TO SCALE

LEGEND

1 – PERISTALTIC PUMP	6 – SOLENOID COIL OUTPUT
2 – RUBBER HOSE	7 – ISOCENTER POSITION
3 – WATER RESERVOIR	8 – 10 ml SYRINGE
4 – SOLENOID COIL	9 – INJECTION POINT
5 – 1.89 T MAGNET	10 – H-Xe DISSOLVED IN PFOB EMULSION

Fig. 5.1. Schematic of the experimental setup used in the flow experiments with H-Xe dissolved in PFOB emulsions.

The point of injection of the PFOB emulsion and H-Xe mixture was made as close to the bore of the superconducting magnet as possible to minimize the loss of magnetization due to the decrease of the static magnetic field experienced by the H-Xe dissolved in emulsion probe. Since the diameter of the coil (1.1 cm) was slightly larger than the rubber hose which composed most of the flow loop, the flow direction through the coil was always chosen to be opposite to the direction of the gravitational field, so at all times during the flow, the volume of the coil was completely filled with water.

The water flow was controlled by the dial of the peristaltic pump. The pump was calibrated for five different flow rates. Calibration was performed using a graduated glass cylinder (0.5 ml uncertainty) and a timer with 1 s precision. The flow calibration values and precision were calculated from the average and standard deviation of three repeated measurements.

Two different flow rates were chosen for the experiments involving H-Xe dissolved in PFOB emulsions: (2.35 ± 0.05) ml/s and (3.38 ± 0.08) ml/s. This selection was based on the volume of the coil ($V = 4.85$ ml) and the injection time range (1-3 s). The flow was chosen to be larger than the input flow of the injection into the water stream, but also slow enough to allow bolus dilution during its time course from the injection point to the coil. The total volume of the hose between the injection point and the coil was approximately 11 ml. The maximum flow rate available with the peristaltic pump was (4.09 ± 0.11) ml/s.

PFOB emulsion preparation and water dilution followed the same steps detailed in the experimental section in Chapter 4. An 80% volume water concentration of the emulsion was chosen for the measurements. This water dilution choice was based on the

fact that both water and PFOB peaks are required for the dynamic PFOB concentration measurements. The uncertainty in the peak linewidth measurements depends on the SNR. The evolution of peak height and linewidth for the two peaks of H-Xe dissolved in different water dilutions of the PFOB emulsions is shown in Figs. 4.3 and 4.5 in the previous chapter. The best balance between the peak heights is obtained for water volume dilutions in the range 85% to 90%. Hence, initial 80% water volume concentration of the PFOB emulsion was considered to be the best for the dynamic acquisition of H-Xe spectra.

The next steps were similar to the ones used in the static dilution experiments described in Chapter 4. The H-Xe gas from the polarizer was cryotrapped using a glass trap and liquid nitrogen (Fig. 4.1). After approximately 3 minutes, the trap was immersed in warm water and the H-Xe gas was expanded in the syringe containing 4.0 ml of 80% water volume diluted PFOB emulsion. Immediately prior to this procedure, the NMR described in the following section was initiated. This step was done before the injection because the bolus arrived at the coil during or immediately after the injection depended on the chosen water flow rate. In this way, throughout the entire time of the bolus passage through the coil, the RF pulses were able to excite the magnetization of the dissolved H-Xe and sample the complete bolus passage through the coil. A single experiment included 8 to 12 spectra depending on how long the bolus passed through the coil.

Immediately after the H-Xe was dissolved in the diluted PFOB emulsion, the content of the syringe was injected into the water stream using a valve system connected to the flow system. The injection time was difficult to control, so the injection time was estimated to be in the range of 1-3 seconds.

5.3.2. Pulse Sequence Design

The NMR pulse sequence consisted of a train of 500 RF pulses separated by a time $TR = 250$ ms. The RF pulse duration was $150 \mu\text{s}$. The spectral width was set at 10 kHz which covered the chemical shift range of 1900 Hz between the water peak and PFOB peak of the H-Xe dissolved in emulsion. A 2048 point sample array was used, corresponding to a time of 205 ms for one data acquisition (T_{acq}).

The choice of TR was determined based on two factors: (i) sufficient time resolution is required to allow the acquisition of a reasonable number of spectra during the bolus passage through the coil of only 2-3 seconds and (ii) the time between pulses has to accommodate the transverse relaxation time. For a given transverse relaxation time T_2^* , the optimal acquisition time T_{acq} , using the Rayleigh resolution criterion, is given by [55]:

$$T_{\text{acq}} = \pi T_2^* . \quad (5.6)$$

FWHM values of the H-Xe resonance peaks in water-diluted PFOB emulsions vary from 65 Hz down to 5 Hz. Using Eq. 2.23 and Eq. 5.6, the corresponding range of transverse relaxation times is 15-200 ms. This range is entirely covered by the selection of point array size and spectral width.

The selection of RF pulse duration and amplitude was based on a compromise between signal-to-noise ratio (SNR) and tracking the whole volume of the injected bolus. On the one hand, large flip angle RF pulses improve the overall SNR leading to better accuracy of the linewidth measurements. On the other hand, the solenoid coil has an extended volume of 4.85 ml, and samples the entire bolus. In the case of hyperpolarized

gases, large flip angle RF pulse application results in irreversible loss of the transverse magnetization M_z by an amount $M_z \cos\alpha$ as it was discussed in section 2.4. Since H-Xe concentration in the tail of the bolus is small, the magnetization has to be interrogated with small tip angle RF pulses to properly sample the entire volume of the injected emulsion.

Tip-angle (α) was calibrated using the NMR sequence described above and a 'static' sample consisting of H-Xe dissolved in 1.5 ml of water in a syringe. The result of this experiment is shown in Fig. 5.2 in which the relative MR signal intensity (measured as the water peak height), I/I_0 , is plotted against time $t = n \cdot TR$, where n is the number of applied RF pulses and TR represents the time between RF pulses. Looking at the plot from Fig. 5.2 one can notice that even after 130 RF pulses the magnetization has not decayed completely indicating a small tip angle. The linear fit and the graph from Fig. 5.2 were done using Origin 5.0 (MicroCal, Northampton, MA, USA).

Using the natural logarithm of Eq. (2.25) from Chapter 2, the relationship between slope a and longitudinal relaxation time T_1 is:

$$T_1 = -1/a. \quad (5.7)$$

Using this equation, longitudinal relaxation time was estimated to be: $T_1 = (27.6 \pm 0.6)$ s.

Similarly, the relationship between flip angle α , intercept b and number of RF pulses n , is:

$$\alpha = \cos^{-1}(e^{-b/n}). \quad (5.8)$$

Using Eq. (5.8) and intercept b from the linear fit of Fig. 5.2, the flip angle was estimated to be $\alpha = (3.64 \pm 0.10)^\circ$. This value of the flip angle was considered sufficiently

small not to destroy the magnetization corresponding to low concentrations of H-Xe in the tail of the injected bolus.

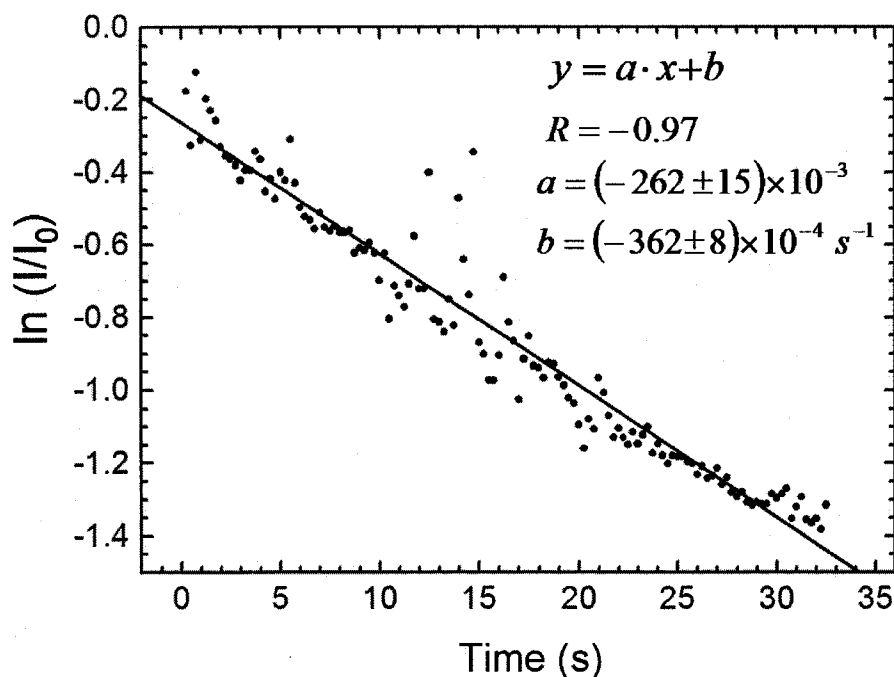


Fig. 5.2. Semi-logarithmic plot of relative H-Xe dissolved in water signal during the application of n ($= 130$) RF pulses equally spaced at $TR = 250$ ms. The observed exponential decay of the signal is the result of irreversible loss of magnetization and longitudinal relaxation T_1 . Correlation coefficient of the linear fit is $R = -0.97$.

5.3.3. Data Analysis

The acquired spectra were analyzed using the MRRS Specana software (MRRS MR5000, Surrey, UK). This step included phase corrections of the spectra using the spectral analysis software and extracting the FWHM values for the two peaks of each spectrum. For three different flow measurements (three sets of spectra), SNR values (ratio between peak height and noise standard deviation) were recorded and their average

value was found to be approximately 9.4. This value was further used in computing the errors in FWHM readings and PFOB volume concentration estimates.

There are two ways to express SNR in the frequency domain: (i) using peak height as signal or (ii) area under the peak as signal [87]. If area under the peak is chosen, the SNR in the frequency domain is equal to the SNR in the time domain. In the other case, SNR is inversely proportional to the FWHM of the peak [87]. Thus, $\sigma(FWHM)$ can be evaluated as a function of SNR expressed as peak height/noise standard deviation ratio:

$$\sigma(FWHM) = FWHM / SNR . \quad (5.9)$$

Each experimental procedure contributed to the total uncertainty. In particular, the uncertainty in PFOB concentration, c_1 , for each acquired H-Xe spectrum can be calculated by error propagation of $\sigma(FWHM)$ from Eq. (5.9) to Eqs. (5.4) and (5.5). The overall uncertainties on the flow measurements and average concentrations were estimated by repeating each flow experiment three times.

Practical implementation of Eqs. (5.3)-(5.5) reduced to numerical evaluation of the integrals using the discrete concentration-time values and a C++ code.

5.4. Results and Discussion

Figure 5.3 shows typical H-Xe spectra dissolved in emulsion after the bolus injection obtained in one experiment.

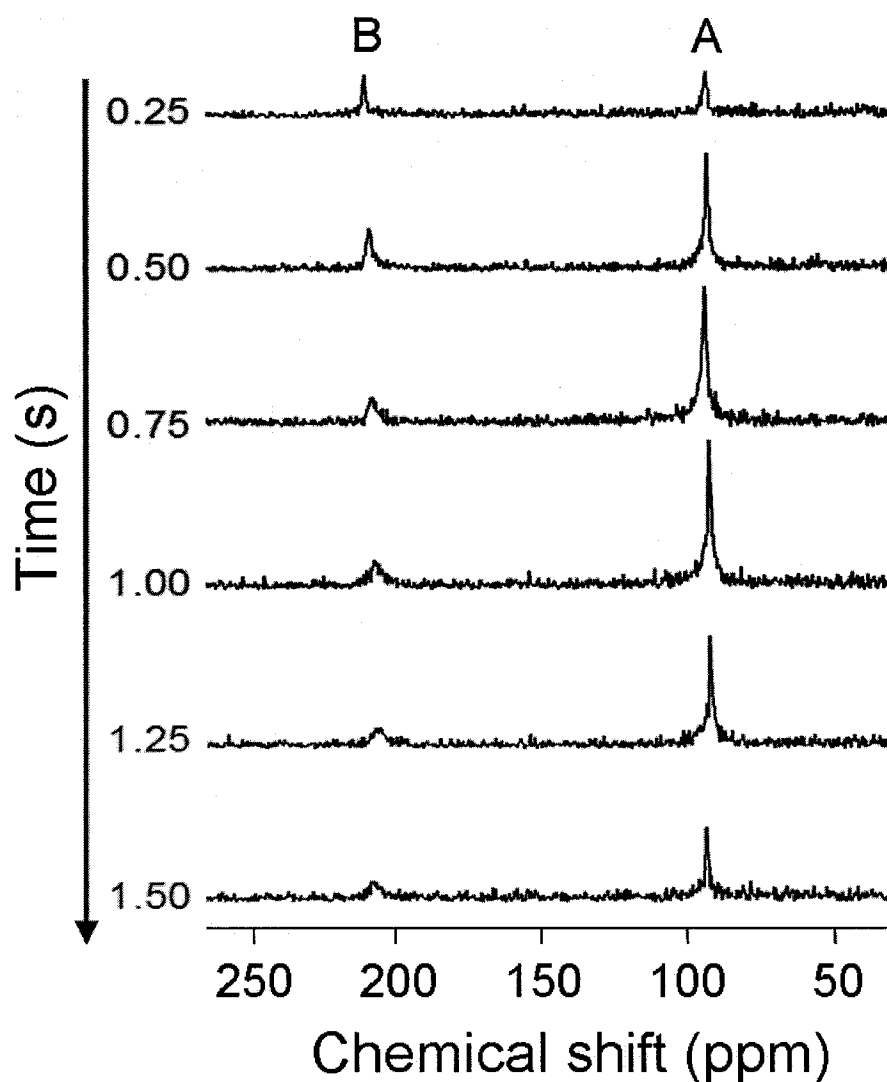


Fig. 5.3. Plot of typical dynamic acquisition of NMR spectra of H-Xe dissolved in the PFOB emulsion bolus. Peak A represents the PFOB peak and peak B is the water peak. The H-Xe gas resonance peak was used as reference for the chemical shift scale.

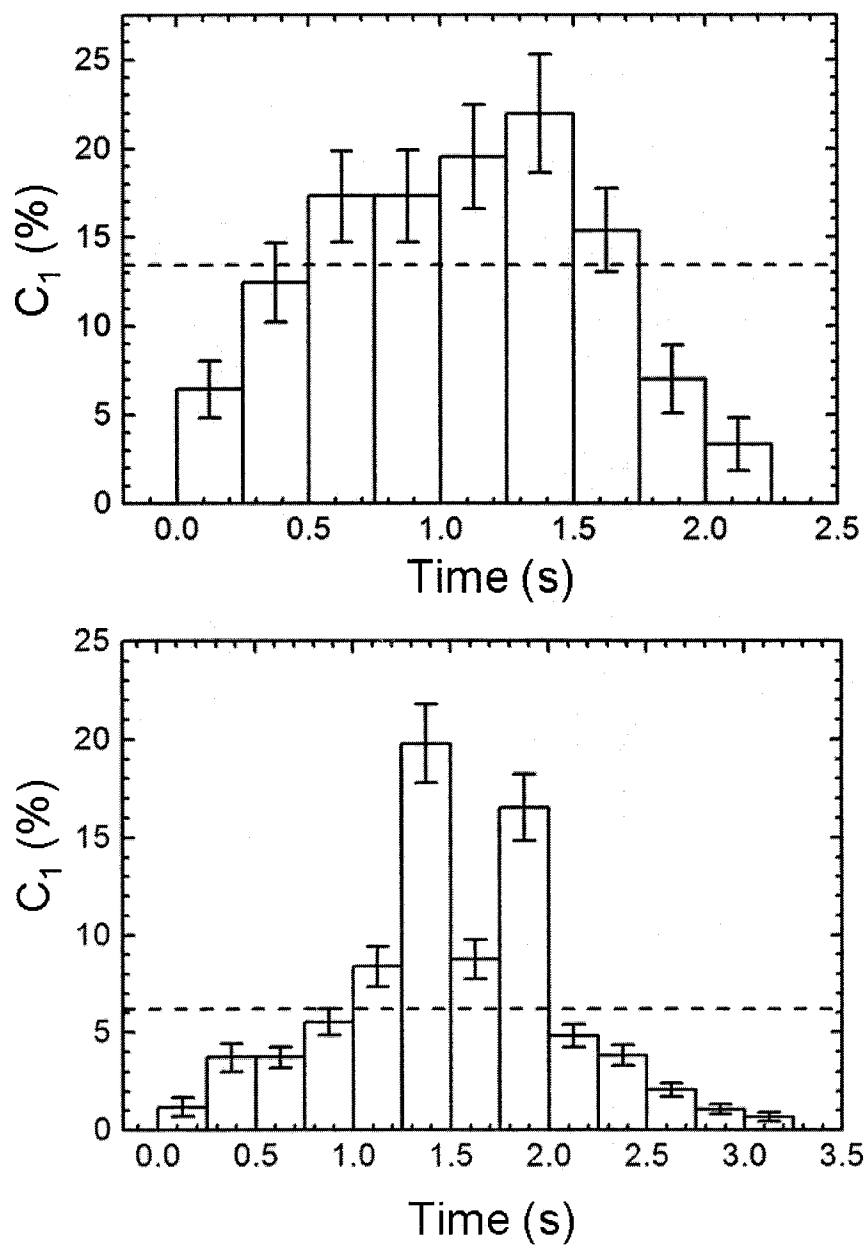


Fig. 5.4. Two different PFOB concentration-time data plots corresponding to the two flow rates: (a) (2.35 ± 0.05) ml/s and (b) (3.38 ± 0.08) ml/s. The dashed line represents the average PFOB volume concentration \bar{c}_1 . The error bars were calculated based on the average SNR of the acquired spectra.

The average PFOB volume concentration \bar{c}_1 was calculated based on the area under the concentration-time curve. In this case, the average concentration is given by the arithmetic mean of the measured values of the PFOB volume concentration during bolus passage:

$$\bar{c}_1 = \frac{\sum_{i=1}^n c_1(i)}{n}. \quad (5.10)$$

In this equation, $c_1(i)$ represents the PFOB volume concentration in the coil measured after the i -th RF pulse application and n represents the total number of RF pulses corresponding to the bolus passage.

It can be seen from analyzing Fig. 5.4 that the lower average volume concentration of PFOB corresponds to the higher flow rate, as it was expected (Fig. 5.4b). This can be explained by the fact that a higher flow rate gives rise to a more diluted bolus for a relatively constant injection time of the same volume of PFOB emulsion. Hence, flow measurements are dependent on the injection time as well as the water flow rate.

Figure 5.5 shows the flow rates calculated using Eq. 5.3 and concentration-time data (Fig. 5.4) versus expected flow rates. The χ^2 per number of degrees of freedom (χ^2/n) was 0.19 and indicates a good agreement of NMR measurements with calibrated values of the peristaltic pump within experimental uncertainties.

As it has been previously discussed for the case of PFOB concentration-time plots, the main variability factor in the experiments was the injection procedure. The initial volume of 80% water volume-diluted PFOB emulsion was chosen to be 4.0 ml, but during the experiments the expulsion of the remaining H-Xe gas was unavoidably associated with spillage. This is a reason for the uncertainty in the volume of PFOB

emulsion injected in the water stream using the experimental tools described in the previous section. For the initial PFOB emulsion volume V_0 used as an input value in Eqs. (5.3) and (5.5), a value of 3.9 ml was used for the final flow and bolus volume calculations.

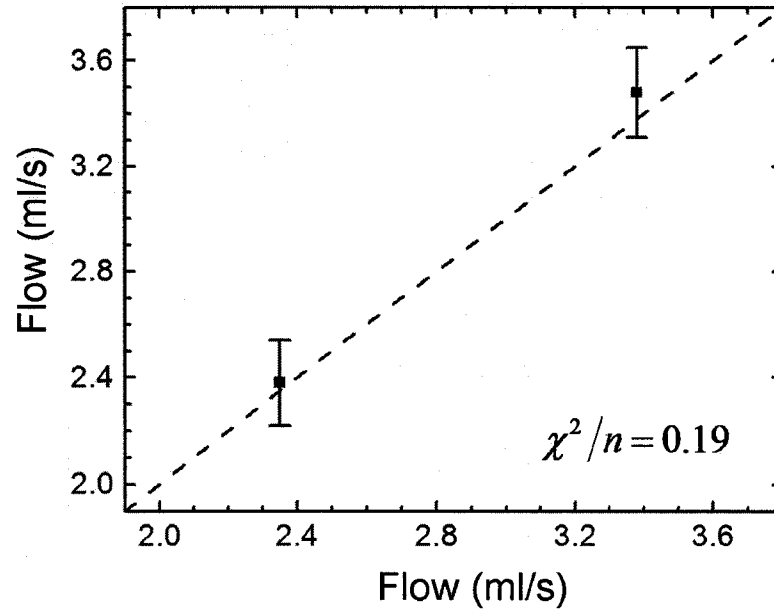


Fig. 5.5. Plot of the flow rate measurements. The dashed line represents the identity between flow measurements (vertical) and flow calibrated values of the peristaltic pump (horizontal). The error bars represent the standard deviation of three repeated measurements.

Mean transit time (MTT) of the bolus was estimated following Eq. (5.4). The results are shown in Fig. 5.6. This time depends on the water flow and the total volume of the bolus. The difference between the two high flow values means that the higher flow rate was compensated by a larger bolus volume as it is shown in Fig. 5.8.

The average water volume concentration corresponding to the two flow rates is shown in Fig. 5.7. A significant increase is seen for the highest flow rate value.

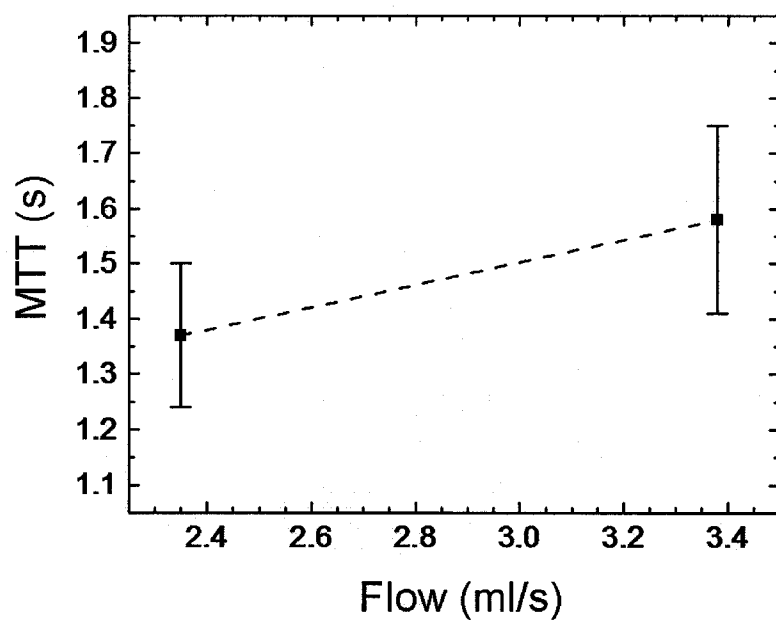


Fig. 5.6. Plot of the mean transit time (MTT) corresponding to the two flow rates.

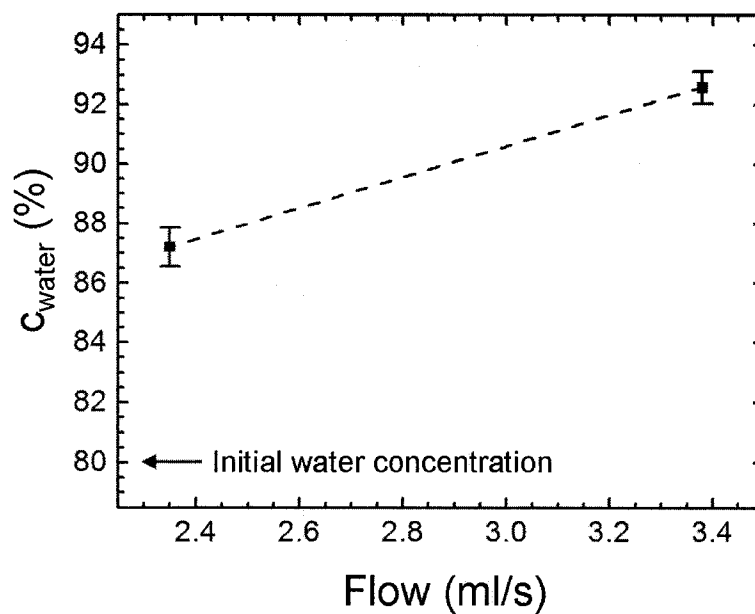


Fig. 5.7. Plot of the water volume concentration corresponding to the two flow rates. Water dilution increased with increasing flow rate as it was expected.

The volume of distribution, V_d , (i.e. volume available for the PFOB droplets) can be calculated using the Central-Volume Principle (Eq. 5.5). In Fig. 5.8, the average values of the volume of distribution are shown for the two flow rates (full square points). In the upper part of the graph (full circle points), the volume calculated based on injected volume V_0 , initial PFOB volume concentration c_0 , and average PFOB volume concentration \bar{c}_1 corresponding to the two flow rates is shown. The value of \bar{c}_1 in the bolus was estimated using Eq. (5.10). This volume, V , represents the total volume of diluted emulsion starting from an initial volume of emulsion V_0 with initial PFOB volume concentration c_0 and is given by:

$$V = \frac{c_0 V_0}{c_1} . \quad (5.11)$$

The discrepancy between the volumes of distribution, V_d , calculated based on Eqs. (5.4) and (5.5) and volumes calculated using Eq. (5.11) reveals that the injected bolus of PFOB emulsion and H-Xe is not completely mixed into the water stream. Incomplete mixing impedes the diffusive exchange of H-Xe between the PFOB droplets and water to mask the true PFOB concentration in the water stream during the bolus passage. This is particularly relevant for this experiment since the PFOB emulsion is composed of droplets with average diameter larger than $1 \mu\text{m}$, so thermal agitation is insufficient to completely mix the PFOB emulsion bolus during its time course from the injection point to the coil. The importance of well-mixed tracers in the compartments has been discussed in the literature [92] [93]. The fact that flow rates were correctly predicted

using the Stewart-Hamilton relation (Eq. 5.3) confirms that its validity is not restricted by the degree of tracer mixing in the volume of distribution V_d [93].

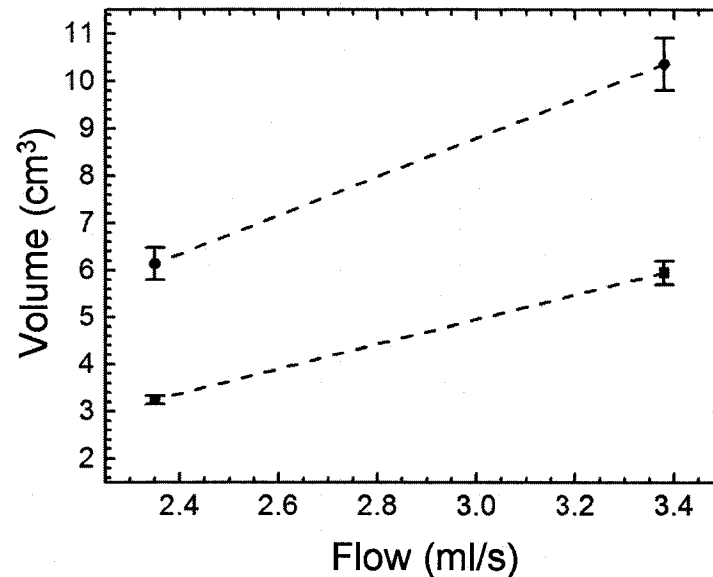


Fig. 5.8. Plot of the calculated volume of distribution V_d (solid squares) and total diluted emulsion volume based on the average PFOB volume concentration \bar{c}_1 (solid circles) for the two flow rates. The discrepancy between the two values can be explained by incomplete mixing of the injected bolus into the water stream.

The Stewart-Hamilton equation cannot be used for *in vivo* blood flow in tissue measurements because the initial quantity of tracer entering a targeted volume of tissue is not known [95]. For this reason, the Central-Volume Principle (Eq. 5.5) is more useful for blood perfusion measurements [14]. This is especially advantageous because it has been shown by Roberts *et al.* [96] that the relationship is equally valid for the case of multicompartiment systems.

Static experiments with PFOB emulsions in blood described in Chapter 4 showed the dependence of blood linewidth on volume concentration. This means that, in principle, the diffusive exchange of H-Xe atoms between PFOB emulsion droplets and

blood could be used to probe the volume of distribution of H-Xe in tissues. This could be achieved using *in vivo* H-Xe spectroscopy in magnetic field gradient selected slices. The principle of such an experiment is depicted in Fig. 5.8.

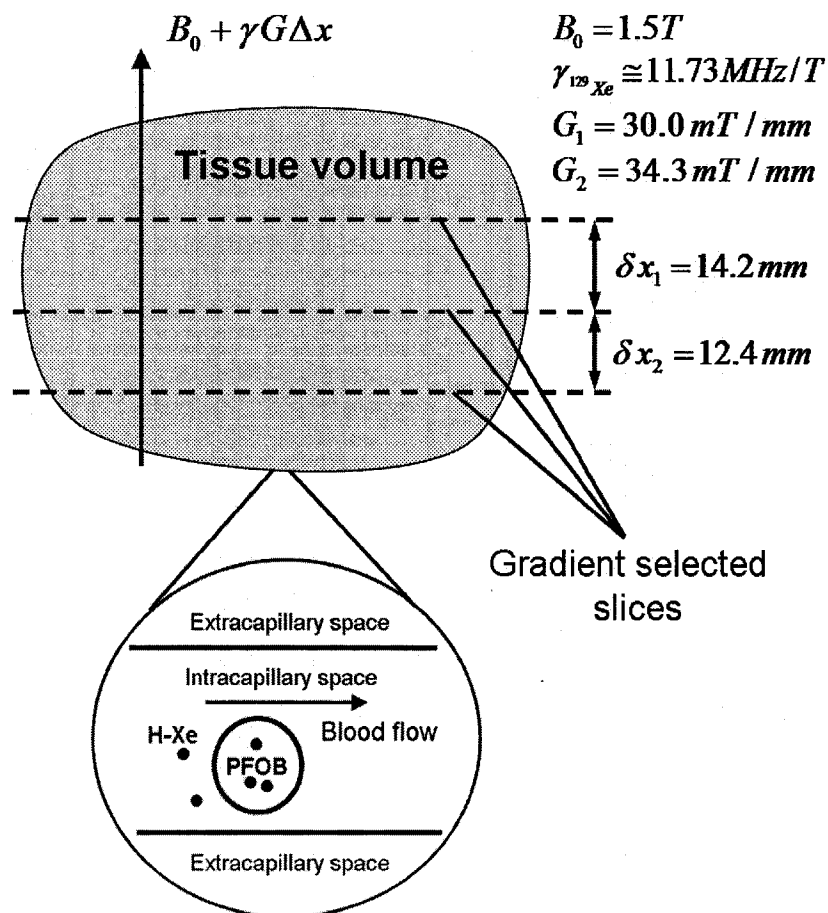


Fig. 5.9. Scheme of proposed *in vivo* blood concentration measurements. Dashed lines represent the boundaries of two adjacent gradient selected slices. The lower part of the figure is an enlarged representation of the diffusive exchange process of H-Xe between PFOB droplets and blood in the capillaries of the tissue. It is assumed that the tissue volume is perfused by an arterial injection of PFOB emulsion carrying the H-Xe gas.

The magnetic field gradient and slice thickness values shown in Fig. 5.8 were calculated based on γ which is the gyromagnetic ratio of ^{129}Xe and the selected

frequency width δf . The shift in the resonance frequency Δf due to the change of the static magnetic field produced by a gradient G at distance Δx is given by:

$$\Delta f = \gamma G \Delta x. \quad (5.12)$$

A graphical representation of these calculations is shown in Fig. 5.9. In the linear plot, it is assumed that for distance $\Delta x = 0$, the gradient is zero ($G = 0$). All calculations are done with $B_0 = 1.5T$, which is the static field of most superconducting magnets used in clinics.

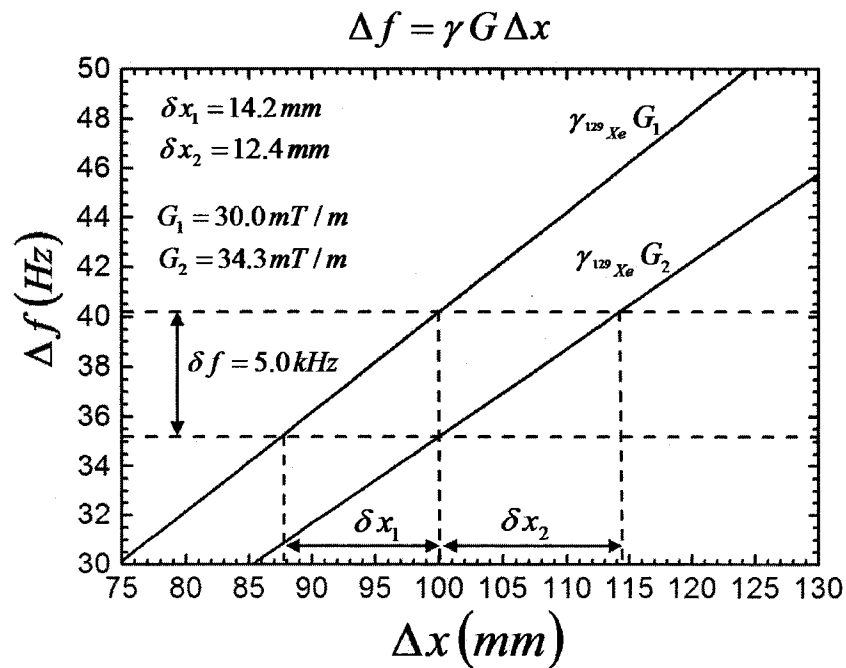


Fig. 5.10. Plot of the linear dependence of resonance frequency shift Δf as a function of position Δx for two magnetic field gradient values: $G_1 = 30.0 \text{ mT/m}$ and $G_2 = 34.3 \text{ mT/m}$ which correspond to the two adjacent slices from Fig. 5.9.

Concentration-time curves of H-Xe in blood corresponding to the two gradient selected slices shown in Fig. 5.8 could be measured as it was shown in Fig. 5.3. for the case of PFOB emulsion and H-Xe bolus injected in a water stream. With enough SNR,

sub-second time resolution of spectra acquisition is possible *in vivo* as well as in water. Using optical microscopy methods, blood flow and red-blood cell speed have been measured in the microvasculature of Syrian golden hamsters for different partial oxygen pressures (pO_2) [97]. Blood flow measurements were found to be in the range of a few tens of nl/s, while red-blood-cell (RBC) speed was in the range of a few mm/s. This means that even a time resolution larger than one second provides a good sampling of the bolus within a 10 mm slice thickness.

The methodology of NMR blood flow measurements with paramagnetic contrast agents using bolus dilution theory has been extensively discussed in the literature. Tissue concentration-time curve response to an idealized bolus is called tissue residue function (TRF) and when it is measured in the injected artery is called arterial input function (AIF). The actual measured concentration-time curve in tissue is a convolution of TRF and AIF [14]. Since the volume of dilution for the contrast agent (blood volume for non-diffusible contrast agents) is not known, relative blood perfusion measurements are possible by comparing AIF measurements with concentration-time measurements in tissue [14] [95]. Absolute blood perfusion measurements using paramagnetic contrast agents are possible only if information about blood vasculature is provided [18].

The difficulties of blood perfusion measurements using MR paramagnetic contrast agents has been related to the problem of finding a direct, reliable relationship between the NMR signal and tracer concentration *in vivo* [19]. The NMR signal comes from the water molecules whose relaxation time is affected by the passage of paramagnetic contrast agent bolus. In tissues, the motion of water molecules is not

restricted to a single compartment. Hence, the MR signal is affected by the chemical exchange of water among different compartments [14] [19].

H-Xe dissolved in PFOB emulsions offers the possibility of a direct relationship between NMR spectra and blood concentration as it was shown in Chapter 4. Following the steps described in this chapter, *in vivo* blood concentration-time measurements with H-Xe dissolved in PFOB emulsions are possible if a reasonable SNR (>10) of the NMR signal is achievable. Given concentration-time data, mean transit time (MTT) can be calculated using Eq. (5.4). Comparison of MTT values in two or more slices can provide valuable information about blood perfusion (i.e. flow rate, MTT) in the tissue volume of interest.

5.5. Conclusions

Water flow measurements using H-Xe dissolved in PFOB emulsion matched the calibrated values of the peristaltic pump. This result confirmed the hypothesis that diffusive exchange of H-Xe between water and PFOB droplets in a PFOB emulsion can be used for dynamic water concentration measurements. NMR methods included optimized H-Xe spectra acquisition using 3.6° tip angle RF pulse spaced by 0.25 seconds. PFOB volume concentrations during the PFOB emulsion and H-Xe bolus passage through the coil were calculated using the slow exchange approximation explained in detailed in Chapter 3. The residence times in the two compartments can be found directly

from the FWHM measurements of the spectra shaped by the diffusive exchange of spins. Thus concentration-time curves were obtained for two different water flow rates.

The correlation between concentration-time curves and flow rates mathematically expressed by the Stewart-Hamilton relationship allowed calculations of flow rates. Mean transit time of the bolus passage was also estimated for the two flow rates and it was found that the PFOB emulsion bolus was not completely mixed into the water stream as it was expected.

Also, it is proposed that *in vivo* blood concentration-time measurements could be obtained from the NMR spectra of H-Xe dissolved in a PFOB emulsions used as a carrier for hyperpolarized ^{129}Xe gas. Gradient selected slices are proposed as a possible tracking method of the PFOB emulsion bolus. Hence, MTT values could possibly be estimated in different parts of the body tissue and could provide useful information about blood flow or blood perfusion in tissues.

6. Summary and Future Work

6.1. Summary

Physiological effects induced by pathological angiogenesis within malignant tissues can be detected by relative or absolute blood flow/perfusion measurements. In this thesis, hyperpolarized ^{129}Xe dissolved in PFOB emulsions has been proposed as an MR contrast agent for cancer detection.

This proposal meets two requirements of a good contrast agent for blood perfusion measurements: (i) biocompatibility and (ii) good time resolution (i.e. < 1 s) necessary for dynamic data acquisition.

Xenon is a virtually inert, noble gas, with no toxic effects associated with *in vivo* administration. For more than 50 years, the anaesthetic effect of xenon has been observed and studied [97]. While this physiological effect may present additional complications in the use of H-Xe in pulmonary studies, the small quantities of xenon (~ml) which would be introduced in the body by a single PFOB emulsion injection are too small to induce general anaesthesia.

Xenon is a soluble substance in water and in other organic substances present in the body, especially lipids [39]. The measured diffusion coefficient of xenon in water [88] is on the same order of magnitude with the range of measured water diffusion coefficients in the body. This mobility is the underlying strength of xenon for this method: the diffusive exchange of H-Xe between PFOB emulsion droplets and blood

could permit dynamic measurements of PFOB concentration during the passage of the intravenous injected bolus through a certain volume of tissue.

PFOB is an inert organic substance with good solubility for gases. Given these properties, the PFOB emulsion stabilized by EYP has been proposed as a blood substitute (i.e. carrier for O₂ and CO₂). No adverse side effects have been associated with *in vivo* parenteral administration of PFOB emulsion [46].

The assessment of H-Xe dissolved in PFOB emulsions applicability as a contrast agent for cancer detection described in this thesis included three major steps: (i) development of the two-compartment spin diffusive exchange model, (ii) acquisition and analysis of spectra of H-Xe dissolved in PFOB emulsions and *in vitro* spectra of H-Xe dissolved in PFOB emulsions and blood, and (iii) water flow measurements.

6.1.1. Theoretical Modeling

The development of the theoretical two-compartment radial diffusive exchange model was based on the generalized Bloch equations. The motivation was to correctly interpret the NMR spectra of H-Xe dissolved in PFOB emulsions in terms of relative water/PFOB content, emulsion average droplet size, xenon solubility and diffusion coefficients in the two constituents, and EYP membrane permeability. The theoretical model met and exceeded this original purpose. Its applicability is not restricted to emulsions; it is expected to be useful for quantitative analysis of various NMR systems exhibiting radial diffusive spin exchange between two compartments (i.e. two different geometrically separated regions where the NMR relaxation properties and resonance

frequencies are different). The final results were expressed in terms of theoretical NMR spectra for different parameters which characterize the geometry, transverse NMR relaxation, diffusion and solubility. By varying the membrane permeability, spectra corresponding to slow, intermediate and fast exchange regimes were obtained.

In the slow exchange regime (i.e. exchange rate smaller than frequency separation for equal spin populations in the two compartments), a simple equation was found which relates the average spin residence time in one site with the FWHM of resonance peaks in the presence and in the absence of exchange. In this regime, the relative spin population ratio between the two compartments given by the volume ratio weighted by solubility is equal to residence time ratio. Hence, there is the possibility of measuring volume ratio of the two compartments from FWHM measurements of the resonance peaks.

6.1.2. Spectra of H-Xe Dissolved in PFOB Emulsions and Blood

Spectra of H-Xe dissolved in PFOB emulsions for different water volume concentrations allowed a quantitative analysis using the theoretical modeling developed in Chapter 3. From the fit of the experimental FWHM with the theoretical FWHM, the membrane permeability and the average diameter were estimated. Using the slow exchange approximation, the residence time of xenon within the PFOB droplet was estimated. By comparing this time with the average time within a sphere without any surrounding membrane to restrict diffusion, the fractional porosity of the EYP membrane was estimated. Static water dilution spectra also revealed the fact that the PFOB concentration in such emulsions can be calculated based on linewidth FWHM

measurements of the spectra. This feature was exploited in Chapter 5 where PFOB concentration was calculated based on FWHM measurements from H-Xe dissolved in a PFOB emulsion and then injected into a flowing water stream.

In vitro spectra of H-Xe dissolved in PFOB emulsions mixed with blood, revealed a large PFOB peak and a small plasma peak. The difference can be explained by the much lower xenon solubility in blood comparing to PFOB (~10 times) and short longitudinal relaxation time T_1 of xenon in blood (4-7 seconds) [99] [100].

The exchange rate was also calculated based on the relative population ratio between PFOB and blood/water mixture and the calculated residence time in the PFOB droplet. It was found that the exchange rate followed the expected dependence on blood volume concentration confirming that the slow exchange of xenon between PFOB droplet and the surrounding plasma/water compartment determines the observed lineshapes.

The measured FWHM of the plasma peak showed a decreasing trend in the linewidths with increasing blood volume concentration similar to the one observed for diluted PFOB emulsions. This dependence allows PFOB concentration measurements in blood based purely on spectral analysis. This suggests a possible future use *in vivo* for blood flow measurements by dynamic measurements of PFOB concentration after an emulsion bolus injection in which H-Xe has been previously dissolved.

6.1.3. Water Flow Measurements

Flow measurements in Chapter 5 were performed using a peristaltic pump which maintained a closed loop flow of water through a solenoid coil. These measurements for

two different flow rates confirmed the potential of estimating PFOB concentration from basic analysis of dynamically-acquired spectra.

In order to achieve good results, the NMR pulse sequence had to be optimized to fit the purpose of these measurements. Consecutive 3.6° tip-angle pulses were applied every 250 ms. The range of transverse relaxation times permitted this time resolution without which the flow measurements would have not been possible with the given experimental setup.

The Stewart-Hamilton bolus dilution equation, based on the principle of mass conservation, was used for the quantitative analysis of the concentration-time curves and flow calculations. The calculated flow rates were found to be in good agreement with the calibrated values of the peristaltic pump. The mean transit time (MTT) was also calculated as the first moment of the concentration-time distribution. The volume of the distribution (i.e. available volume for bolus dilution) was calculated in two ways. First, it was calculated using the Central Volume Theorem and, then, it was estimated using initial PFOB concentration and measured average PFOB concentration in the bolus while it passed through the coil. The discrepancy between the two values revealed that the injected bolus was not completely mixed into the water stream. This result was expected given the relatively high flow rates and short injection times that did not allow complete mixing of PFOB emulsion droplets into the flowing water.

The final part of Chapter 5 addressed speculatively the possible methods to be used for future *in vivo* blood flow measurements. The comparison between MTT estimates of the H-Xe bolus passage for two different gradient selected slices can provide useful information about blood perfusion in the tissue. Even though this new proposed

method would not solve the problem of absolute perfusion measurements, a few advantages with respect to paramagnetic contrast agents for proton MR imaging systems can be distinguished: (i) no need for arterial input function (AIF) measurements since comparison between slices could be done in the tissue volume of interest, (ii) sub-second time resolution, and (iii) clear distinction between signals from H-Xe in different compartments since PFOB and blood peaks are well separated in the frequency domain (~ 100 ppm).

6.2. Future Work

In vivo blood flow measurements are necessary to validate the techniques described in this thesis. PFOB concentration in blood could be measured from *in vivo* H-Xe in bolus spectra, using calibration curves from *in vitro* experiments similar to the ones presented in Chapter 4. Alternatively, PFOB concentration could also be calculated directly from *in vivo* spectra using the slow exchange approximation and measurements of H-Xe transverse relaxation time in blood for different water dilutions.

The pulse sequence can be suitably modified for *in vivo* blood flow measurements. For the acquisition of spectra from H-Xe dissolved in PFOB emulsion and injected in the flowing water used here, small tip angles ($\sim 4^\circ$) were employed to preserve the magnetization of H-Xe in the tails of the bolus. In principle, larger flip-angle pulses can be used. The only limitation of the flip angle value is that the entire volume of H-Xe in the bolus has to be sampled by the RF pulses in order to obtain an accurate time-

concentration curve. Since the linewidth value and not NMR signal amplitude was used in the flow calculations, the dynamics of signal strength after repeated RF pulse excitations is not important.

Low SNR of H-Xe dissolved in blood represents the major impediment in the applicability of this method for *in vivo* blood flow/perfusion measurements. The factors contributing to low SNR have been identified to be the following: short longitudinal relaxation time of H-Xe in blood ($T_1 = 4-7$ s) [99] [100], low solubility of xenon in blood and current polarization levels (5% - 20%) using laser pumping technique.

The short T_1 of xenon in blood constrains the injection point to be as close to the target as possible. In particular, H-Xe dissolved in PFOB emulsion method could benefit from higher nuclear spin polarization techniques even if production would be limited to small amounts of hyperpolarized gas. While xenon solubility and T_1 in blood cannot be improved, higher spin polarization levels are possible. Improvements in ^{129}Xe polarization techniques ($\sim 80\%$) have been demonstrated [101] and are encouraging for *in vivo* H-Xe applications.

References

- [1] Säbel M. and Aichinger H., Recent developments in breast cancer imaging, *Phys. Med. Biol.* **41**:315-68 (1996).
- [2] Jones C.H., Methods of breast imaging, *Phys. Med. Biol.* **27**:463-99 (1982).
- [3] Carmeliet P. and Jain R.K., Angiogenesis in cancer and other diseases, *Nature* **407**:249-57 (2000).
- [4] Auerbach R., Auerbach W. and Polakowski I., Assay for angiogenesis: a review, *Parmac. Ther.* **51**:1-11 (1991).
- [5] Gullino P.M., Angiogenesis and oncogenesis, *J. Natl. Cancer Inst.* **61**:639-643 (1978).
- [6] Aronen H.J., Pardo F.S., Kennedy D.N., Belliveau J.W., Packard S.D., Hsu D.W., Hochberg F.H., Fischman A.J., and Rosen B.J., High microvascular blood volume is associated with high glucose uptake and tumor angiogenesis in human gliomas, *Clin. Cancer Res.* **6**:2189-2200 (2004).
- [7] Raghunand N., Gatenby R.A., and Gillies R., Microenvironmental and cellular consequences of altered blood flow in tumors, *Br. J. Radiol.* **76**: S11-S22 (2003).
- [8] McDonald D.M. and Balluk P., Significance of blood vessel leakiness in cancer, *Cancer Res.* **62**:5381-85 (2002).
- [9] Jackson V.P., Imaging of radiographically dense breast, *Radiology*, **188**:297-301 (1993).
- [10] Jackson V.P., Role of US in breast imaging, *Radiology* **177**:305-11 (1990).

- [11] Gambhir S.S., Molecular imaging of cancer with positron emission tomography, *Nature Reviews Cancer* **2**:683-93 (2002).
- [12] Wahl R.L., Current status of PET in breast cancer imaging, staging, and therapy, *Semin. Roentgenol.* **36**:250-60 (2001).
- [13] Santyr G.E., MR imaging of the breast-imaging and tissue characterization without intravenous contrast agent, *MRI Clinics North Am.*, **4**:673-90 (1994).
- [14] Rosen B.C., Belliveau J.W., Vevea J.M., and Brady T., Perfusion imaging with NMR contrast agents, *Magn. Reson. Med.* **14**:249-65 (1990).
- [15] Choyke P.L., Dwyer A.J., and Knopp M.V., Functional tumor imaging with dynamic contrast-enhanced magnetic resonance imaging, *J. Magn. Reson. Imaging* **17**:509-20 (2003).
- [16] Berg W.A., Gutierrez L., NessAlver M.S., Carter W.B., Bhargavan M., Lewis R.S., and Ioffe O.B., Diagnostic accuracy of mammography, clinical examination, US, and MR imaging in preoperative assessment of breast cancer, *Radiology* **233**:830-49 (2004).
- [17] Orel S.G. and Schnall M.D., MR imaging of the breast for detection, diagnosis, and staging of breast cancer, *Radiology* **220**:13-30 (2001).
- [18] Kiselev V.G., On the theoretical basis of perfusion measurements by dynamic susceptibility contrast MRI, *Magn. Reson. Med.* **46**:1113-22 (2001).
- [19] Cron G., *Quantitative dynamic contrast-enhanced magnetic resonance imaging of the breast*, Ph.D. thesis, Dept. of Medical Physics, University of Wisconsin-Madison, USA (1998).

- [20] Seemann M.D., Neklla S., Ziegler S., Bengel F., and Schwaiger M., PET/CT: fundamental principles, *Eur. J. Med. Res.* **9**:241-6 (2004).
- [21] Bloch F., Nuclear Induction, *Phys. Rev.* **70**:460-74 (1946).
- [22] Purcell E.M., Torrey H.C., and Pound R.V., Resonance absorption by nuclear magnetic moments in a solid, *Phys. Rev.* **69**:37-8 (1946).
- [23] Freeman R., Pioneers of High Resolution NMR, *Concepts Magn. Reson.* **11**:61-70 (1999).
- [24] Damadian R., Tumor detection by nuclear magnetic resonance, *Science* **171**:1151-3 (1971).
- [25] Lauterbur P.C., Image formation by induced local interactions: Examples employing nuclear magnetic resonance, *Nature* **242**:190-1 (1973).
- [26] Mansfield P. and Maudsley A.A., Planar and line scan spin imaging by NMR, *Magnetic Resonance and Related Phenomena Proc. 19th Congr. Ampere, Heidelberg* (IUPAP):247-252 (1976).
- [27] Parra-Robles J., Cross A.R., and Santyr G.E., Theoretical signal-to-noise ratio and spatial resolution dependence on the magnetic field strength for hyperpolarized noble gas magnetic resonance imaging of human lungs, *Med. Phys.* **32**(1):221-9 (2005).
- [28] Kastler A., *J. Phys. Radium* **11**:255-65 (1950).
- [29] Bouchiat M.A., Carver T.R., and Varnum C.M., Nuclear polarization in ^3He gas induced by optical pumping and dipolar exchange, *Phys. Rev. Lett.* **5**(8):373-5 (1960).

- [30] Colegrove F.D., Schearer L.D., and Walters G.K., Polarization of ^3He gas by optical pumping, *Phys. Rev.* **132**:2561-72 (1963).
- [31] Grover B.C., Noble-gas NMR detection through noble-gas-rubidium hyperfine contact interaction, *Phys. Rev. Lett.* **40**(6):391-2 (1978).
- [32] Bhaskar N.D., Happer W., Larsson M., and Zeng X., Slowing down of rubidium-induced nuclear spin relaxation of ^{129}Xe gas in a magnetic field, *Phys Rev. Lett.* **50**(2):105-8 (1983).
- [33] Happer W., Miron E., Schaefer S., Schreiber D., van Wijngaarden W.A., and Zeng X., Polarization of the nuclear spins of noble-gas atoms by spin exchange with optically pumped alkali-metal atoms, *Phys. Rev. A* **29**:3092-110 (1984).
- [34] Zeng X., Wu Z., Call T., Miron E., Schreiber D., and Happer W., Experimental determination of the rate constants for spin exchange between optically pumped K, Rb, and Cs atoms and Xe nuclei in alkali-metal-noble-gas van der Waals molecules, *Phys. Rev. A* **31**:260-78 (1985).
- [35] Raftery D., Long H., Meersman T., Grandinetti P.J., Reven L., and Pines A., High field NMR of adsorbed xenon polarized by laser pumping, *Phys. Rev. Lett.* **66**(5):584-7 (1991).
- [36] Albert M.S., Cates G.D., Driehuys B., Happer W., Saam B., Springer C.S., and Wishnia A., Biological magnetic resonance imaging using laser-polarized ^{129}Xe , *Nature* **370**:199-201 (1994).
- [37] Runge V.M., Safety of approved MR contrast media for intravenous injection, *J. Magn. Reson. Imaging.* **12**:205-13 (2000).

- [38] Kety S.S., The theory and applications of the exchange of inert gas in the lungs and tissues, *Pharmacol. Rev.* **3**:1-41 (1951).
- [39] Cherubini A. and Bifone A., Hyperpolarized xenon in biology, *Prog. Nucl. Magn. Reson. Spectrosc.* **42**:1-30 (2003).
- [40] Sakai K., Bilek A.M., Oteiza E., Walsworth R.L., Balamore D., Jolesz F.A., and Albert M.S., Temporal dynamics of hyperpolarized ^{129}Xe resonances in living rats, *J. Magn. Reson. Series B* **111**:300-4 (1996).
- [41] Wagshul M.E., Button T.M., Li H.F., Liang Z., Springer C.S., Zhong K., and Wishnia A., In vivo MR imaging and spectroscopy using hyperpolarized ^{129}Xe , *Magn. Reson. Med.* **36**:183-91 (1996).
- [42] Mugler III J.P. *et al.*, MR imaging and spectroscopy using hyperpolarized ^{129}Xe gas: preliminary human results, *Magn. Reson. Med.* **37**:809-15 (1997).
- [43] Swanson S.D., Rosen M.S, Agranoff B.W., Coulter K.P., Welsh R.C., and Chupp T.E., Brain MRI with laser-polarized Xe, *Magn. Reson. Med.* **38**:695-8 (1997).
- [44] Kilian W., Seifert F., and Rinneberg H., Dynamic NMR spectroscopy of hyperpolarized Xe in human brain analyzed by an uptake model, *Magn. Reson. Med.* **51**:843-7 (2004).
- [45] Bifone A., Song Y.-Q., Seydoux R., Taylor R.E., Goodson B.M., Pietrass T., Budinger T.F., Navon G., and Pines A., NMR of laser-polarized xenon in human blood, *Proc. Natl. Acad. Sci. USA* **93**:12932-36 (1996).
- [46] Riess J.G., Oxygen carriers ("blood substitutes") - raison d'être, chemistry, and some physiology, *Chem. Rev.* **101**:2797-2919 (2001).

- [47] Clark L.C. and Gollan F., Survival of mammals breathing organic liquids equilibrated with oxygen at atmospheric pressure, *Science* **152**:1755-6 (1966).
- [48] Sloviter H.A., Kamimoto T., Erythrocyte substitute for perfusion of brain, *Nature* **216**:458-60 (1967).
- [49] Pollack G.L., Kennan R.P. and Holm G.T., Solubility of inert gases in PFC blood substitute, blood plasma and mixtures, *Biomat. Art. Cells Immob. Biotech.* **20**:1101-4 (1992).
- [50] Wolber J., Rowland I.J., Leach M.O. and Bifone A., Perfluorocarbon emulsions as intravenous delivery media for hyperpolarized xenon, *Magn. Reson. Med.* **41**:442-9 (1999).
- [51] Wolber J., McIntyre D.J.O., Rodrigues L.M., Carnochan P., Griffiths J.R., Leach M.O. and Bifone A., *In vivo* hyperpolarized Xe NMR spectroscopy in tumors, *Magn. Reson. Med.* **46**:586-91 (2001).
- [52] Slichter C.P., *Principles of Magnetic Resonance* (Springer-Verlag, New York 1990).
- [53] Cowan B., *Nuclear Magnetic Resonance and Relaxation* (Cambridge University Press, Cambridge 1997).
- [54] Rabi I.I., Ramsey N.F. and Schwinger J., Use of rotating coordinates in magnetic resonance problems, *Rev. Mod. Phys.* **26**: 167-171 (1954).
- [55] Callaghan P.T., *Principles of Nuclear Magnetic Resonance Microscopy* (Clarendon Press, Oxford 1991).
- [56] Bloembergen N., Purcell E.M., Pound R.V., Relaxation effects in nuclear magnetic resonance absorption, *Phys Rev.* **73**:679-712 (1948).

- [57] Carr H.Y. and Purcell E.M., The effect of diffusion on free precession in nuclear magnetic resonance, *Phys. Rev.* **94**:630-8 (1954).
- [58] Meiboom S. and Gill D., Modified spin-echo method for measuring nuclear relaxation times, *Rev. Sci. Instr.* **29**:688-91 (1958).
- [59] Torrey H.C., Bloch equations with diffusion terms, *Phys. Rev.* **104**:563-5 (1956).
- [60] Hoult D.I. and Bhakar B., NMR signal reception: virtual photons and coherent spontaneous emission, *Concepts Magn. Reson.* **9**:277-97 (1997).
- [61] Hoult D.I., The Principle of Reciprocity in signal strength calculations – a mathematical guide, *Concepts Magn. Reson.* **12**:173-87 (2000).
- [62] Hoult D.I. and Richards R.E., The signal-to-noise ratio of the nuclear magnetic resonance experiment, *J. Magn. Reson.* **24**:71-85 (1976).
- [63] Hoult D.I. and Richards R.E., Critical factors in the design of sensitive high resolution nuclear magnetic resonance spectrometers, *Proc. Roy. Soc. (London) A* **344**: 311-40 (1975).
- [64] Cooley J.W. and Tukey J.W., An algorithm for the machine calculation of complex Fourier series, *Math. Computation* **19**:297-301 (1965).
- [65] Johnson J.B., Thermal agitation of electricity in conductors, *Phys. Rev.* **32**:97-109 (1928).
- [66] Happer W., Optical pumping, *Rev. Mod. Phys.* **44**:169-249 (1972).
- [67] Walker T.G. and Happer W., Spin-exchange optical pumping of noble-gas nuclei, *Rev. Mod. Phys.* **69**:629-42 (1997).
- [68] Goodson B. M., Nuclear magnetic resonance of laser-polarized noble gases in molecules, materials, and organisms, *J. Magn. Reson.* **155**:157-216 (2002).

- [69] Patyal B.R., Gao J.-H., Williams R.F., Roby J., Saam B., Rockwell B.A., Thomas R.J., Stolarski D.J., and Fox P.T., Longitudinal relaxation and diffusion measurements using magnetic resonance signals from laser-hyperpolarized Xe nuclei, *J. Magn. Reson.* **126**:58-65 (1997).
- [70] Gao J.-H., Lemen L., Xiong J., Patyal B., and Fox P.T., Magnetization and diffusion effects in NMR imaging of hyperpolarized substances, *Magn. Reson. Med.* **37**:153-8 (1997).
- [71] Gherase M.R., Wallace J. C., Cross A.R., and Santyr G.E., Two-compartment radial diffusive exchange analysis of the NMR lineshape of Xe dissolved in a PFOB emulsion, *J. Chem. Phys.*, **124**, accepted (AIPID # 504627JCP, 2006).
- [72] Zimmerman J.R. and Brittin W.E., Nuclear magnetic resonance studies in multiple phase systems: lifetime of a water molecule in an adsorbing phase on silica gel, *J. Chem. Phys.* **61**:1328-33 (1957).
- [73] Allerhand A. and Gutowsky H.S., Spin-echo NMR studies of chemical exchange. I. Some general aspects, *J. Chem. Phys.* **41**:2115-26 (1964).
- [74] Allerhand A. and Gutowsky H.S., Spin-echo NMR studies of chemical exchange. II. Some general aspects, *J. Chem. Phys.* **42**:1587-99 (1964).
- [75] Carver J.P. and Richards R.E., A general two-site solution for the chemical exchange produced dependence on T_2 upon the Carr-Purcell pulse separation, *J. Magn. Reson.* **6**:89-105 (1972).
- [76] McConnell H.M., reaction rates by nuclear magnetic resonance, *J. Chem. Phys.* **28**:430-1 (1958).

- [77] Belton P.S. and Hills B.P., The effects of diffusive exchange in heterogeneous systems on NMR line shapes and relaxation processes, *Mol. Phys.* **61**:999-1018 (1987).
- [78] Torrey H.C., Bloch equations with diffusion terms, *Phys. Rev.* **104**:563-5 (1956).
- [79] Brownstein K.R. and Tarr C.E., Importance of classical diffusion in NMR studies of water in biological cells, *Phys. Rev. A* **19**:2446-53 (1979).
- [80] Belton P.S. and Hills B.P., The effects of exchange and interfacial reaction in two-phase systems on NMR lineshapes and relaxation processes, *Mol. Phys.* **65**:313-26 (1988).
- [81] Price W.S., Barzykin A.V., Hayamizu K., and Tachiya M., A model for diffusive transport through a spherical interface probed by pulsed-field gradient NMR, *Biophys. J.* **74**:2259-71 (1998).
- [82] Powers D.L., *Boundary value problems*, Academic Press, New York (1999).
- [83] Hey M.J. and Al-Sagheer F., Interphase transfer rates in emulsions studied by NMR spectroscopy, *Langmuir* **10**:1370-76 (1994).
- [84] Venkatesh S., Li J., Caldwell K.D., and Anderson B.D., Compositional heterogeneity in parenteral lipid emulsions after sedimentation field flow fractionation, *J. Pharm. Sci.* **87**, 859-66 (1998).
- [85] Freire M.G., Dias A.M.A., Coelho M.A.Z., and Coutinho J.A.P., Aging mechanisms of perfluorocarbon emulsions using image analysis, *J. Coll. Inter. Sci.* **286**:224-32 (2005).

- [86] White A.S., *Volume estimation from three-dimensional hyperpolarized ^{129}Xe magnetic resonance images*, M.Sc. thesis, Dept. of Physics, Carleton University, Ottawa, Canada (2004).
- [87] Kreis R., Issues of spectral quality in clinical ^1H -magnetic resonance spectroscopy and a gallery of artifacts, *NMR Biomed.* **17**:361-81 (2004).
- [88] Wolber J., Doran S.J., Leach M.O., and Bifone A., Measuring diffusion of xenon in solution with hyperpolarized ^{129}Xe NMR, *Chem. Phys. Lett.* **296**:391-6 (1998).
- [89] Santyr G.E., Kay I., Henkelman M.R., and Bronskill M.J., Diffusive exchange analysis of two-component T_2 relaxation of red-blood-cell suspensions containing Gadolinium, *J. Magn. Reson.* **90**:500-13 (1990).
- [90] Cowan G., *Statistical data analysis* (Clarendon Press, Oxford 1998).
- [91] Forster R.E., The transport of water in erythrocytes, *Current topics in membranes and transport* **2**:42-99 (1971).
- [92] Whitmore R.L., *Rheology of the circulation* (Pergamon Press, Oxford 1968).
- [93] Cottrall M.F., Considerations of the application of indicator dilution methods to the measurements of the flow rates of fluids, *Phys. Med. Biol.* **22**:693-713 (1977).
- [94] Gore J.C. and Majumdar S., Measurements of tissue blood flow using intravascular relaxation agents and magnetic resonance imaging, *Magn. Reson. Med.* **14**:242-48 (1990).
- [95] Axel L., Cerebral blood flow determination by rapid-sequence computed tomography, *Radiology* **137**:679-86 (1980).
- [96] Roberts G.W., Larson K.B., and Spaeth E.E., The interpretation of mean transit time measurements in multiphase tissue systems, *J. Theor. Biol.* **39**:447-75 (1973).

- [97] Filho I.P.T., Kerger H., and Intaglietta M., pO₂ measurements in arteriolar networks, *Microvasc. Res.* **51**:202-12 (1996).
- [98] Lynch C., Baum J., and Tenbrinck R., Xenon anesthesia, *Anesthesiology* **92**:865-68 (2000).
- [99] Albert M.S., Kacher D.F., Balamore D., Venkatesh A.K., Jolesz F.A., T₁ of Xe in blood and the role of oxygenation, *J. Magn. Reson.* **140**:264-73 (1999).
- [100] Wolber J., Cherubini A., Dzik-Jurasz A.S.K., Leach M.O., and Bifone A., Spin-lattice relaxation of laser-polarized xenon in human blood, *Proc. Natl. Acad. Sci. USA* **96**:3664-69 (1999).
- [101] Knagge K., Prange J., and Raftery D., A continuously recirculating optical pumping apparatus for high xenon polarization and surface NMR studies, *Chem. Phys. Lett.* **397**:11-16 (2004).

APPENDIX A

In order to simplify the future calculations, one can employ the following notations:

$$\xi_j = \sqrt{\frac{\alpha_j}{D_j}}, \quad j = 1, 2. \quad (\text{A.1})$$

$$\mu_j = \frac{M_{0j}}{D_j}, \quad j = 1, 2. \quad (\text{A.2})$$

Equations (3.3) and (3.4) from Chapter 3 can be re-written as:

$$\frac{\partial^2}{\partial r^2} (\tilde{M}_1 \cdot r) - \xi_1^2 \cdot (\tilde{M}_1 \cdot r) = -\mu_1 \cdot r \quad (\text{A.3})$$

and

$$\frac{\partial^2}{\partial r^2} (\tilde{M}_2 \cdot r) - \xi_2^2 \cdot (\tilde{M}_2 \cdot r) = -\mu_2 \cdot r. \quad (\text{A.4})$$

The first step is to find the solutions of the homogeneous part of Eqs. (A.3) and (A.4):

$$\frac{\partial^2}{\partial r^2} (\tilde{M}_1 \cdot r) - \xi_1^2 \cdot (\tilde{M}_1 \cdot r) = 0 \quad (\text{A.5})$$

and

$$\frac{\partial^2}{\partial r^2} (\tilde{M}_2 \cdot r) - \xi_2^2 \cdot (\tilde{M}_2 \cdot r) = 0. \quad (\text{A.6})$$

The independent solutions of the homogeneous equations are:

$$\tilde{M}_j(r, s) = c_j^+ \cdot \frac{\sinh(\xi_j \cdot r)}{r} + c_j^- \cdot \frac{\cosh(\xi_j \cdot r)}{r}, \quad j = 1, 2. \quad (\text{A.7})$$

Since the function $\frac{\cosh(\xi_1 \cdot r)}{r}$ is not bounded at $r=0$, one can choose a particular solution of the non-homogeneous equation (A.3) of the form:

$$\tilde{M}_1(r, s) = q_1 \cdot u_1(r, s) + \frac{\mu_1}{\xi_1^2} \quad (\text{A.8})$$

The constant q_1 to be later determined from the boundary conditions and the function $u_1(r, s)$ is given by:

$$u_1(r, s) = \frac{\sinh(\xi_1 \cdot r)}{\xi_1 \cdot r} \quad (\text{A.9})$$

This choice solves the singularity problem, thus satisfying the boundary condition (3.7).

Similarly, for the second equation:

$$\tilde{M}_2(r, s) = q_2^+ \cdot u_2^+(r, s) + q_2^- \cdot u_2^-(r, s) + \frac{\mu_2}{\xi_2^2}. \quad (\text{A.10})$$

The functions $u_2^+(r, s)$ and $u_2^-(r, s)$ were chosen as linear combinations of the independent solutions of the homogeneous equation (A.6) such that:

$$\left(\frac{\partial u_2^+}{\partial r} \right)_{r=a} = 0 \quad (\text{A.11})$$

and

$$\left(\frac{\partial u_2^-}{\partial r} \right)_{r=b} = 0. \quad (\text{A.12})$$

These conditions simplify the calculations when the constants: q_1 , q_2^+ and q_2^- are found from the remaining three boundary conditions: equations (3.5), (3.6) and (3.8). The result is:

$$u_2^+(r,s) = \frac{\xi_2 \cdot a \cdot \cosh[\xi_2 \cdot (r-a)] + \sinh[\xi_2 \cdot (r-a)]}{\xi_2 \cdot r} \quad (\text{A.13})$$

and

$$u_2^-(r,s) = \frac{\xi_2 \cdot b \cdot \cosh[\xi_2 \cdot (r-b)] + \sinh[\xi_2 \cdot (r-b)]}{\xi_2 \cdot r}. \quad (\text{A.14})$$

With this choice, the boundary condition expressed in equation (3.8) gives:

$$q_2^+ = 0. \quad (\text{A.15})$$

One can now determine q_1 and q_2^- from boundary conditions (3.5) and (3.6).

Redefining the notations $q_2 = q_2^-$ and $u_2(r,s) = u_2^-(r,s)$, the transverse magnetization in water as a function of the complex angular frequency s and radius r is:

$$\tilde{M}_2(r,s) = q_2 \cdot u_2(r,s) + \frac{\mu_2}{\xi_2^2}. \quad (\text{A.16})$$

Equations (A.8) and (A.16) represent the solution of the boundary value problem.

In order to find the spectrum, one must integrate the transverse magnetizations in the two sites over the volumes of the two sites: V_1 and V_2 . The volume of the spherical droplet is:

$$V_1 = \frac{4 \cdot \pi \cdot a^3}{3}. \quad (\text{A.17})$$

The volume of the radial shell of water is:

$$V_2 = \frac{4 \cdot \pi \cdot (b^3 - a^3)}{3}. \quad (\text{A.18})$$

The complex quantity S as a function of s representing the complex MR signal can be written as:

$$S(s) = \int_{V_1} \tilde{M}_1(r) \cdot dV + \int_{V_2} \tilde{M}_2(r) \cdot dV. \quad (\text{A.19})$$

In spherical coordinates representation: (r, ϕ, φ) , the volume integrals reduce to:

$$S(s) = 4 \cdot \pi \cdot \int_0^a r^2 \cdot \tilde{M}_1(r) \cdot dr + 4 \cdot \pi \cdot \int_a^b r^2 \cdot \tilde{M}_2(r) \cdot dr. \quad (\text{A.20})$$

Substituting equations (A.8) and (A.16) into (A.20), one can find that:

$$S(s) = \frac{\mu_1 a}{\xi_1^2} V_1 + \frac{\mu_2 (b-a)}{\xi_2^2} V_2 + 4\pi \left[q_1 \int_0^a r^2 u_1(r, s) dr + q_2 \int_a^b r^2 u_2(r, s) dr \right] \quad (\text{A.21})$$

APPENDIX B

A summary of all notations used starting from the known parameters to the final expression of the spectrum given by equation (3.12), is given in the equations below. The “ j ” index refers to parameters and variables corresponding to one of the two chemical environments considered in this model: PFOB (index 1) and water (index 2).

$$p_j = \frac{\gamma_j}{D_j}, \quad j = 1, 2. \quad (\text{B.1})$$

$$r_j = \frac{\omega - \omega_{0j}}{D_j}, \quad j = 1, 2. \quad (\text{B.2})$$

$$\beta = \frac{|M_{01}|}{|M_{02}|} = \frac{\text{Solubility in compartment 1}}{\text{Solubility in compartment 2}}. \quad (\text{B.3})$$

Using the solubility, β , and the initial phase of the initial transverse magnetization, φ_0 , one can find the real and imaginary parts of M_{01} and M_{02} :

$$\text{Re}(M_{01}) = \frac{\beta}{\beta + 1} \cdot \cos(\varphi_0), \quad (\text{B.4})$$

$$\text{Im}(M_{01}) = \frac{\beta}{\beta + 1} \cdot \sin(\varphi_0), \quad (\text{B.5})$$

$$\text{Re}(M_{02}) = \frac{\beta}{\beta + 1} \cdot \cos(\varphi_0), \quad (\text{B.6})$$

$$\text{Im}(M_{02}) = \frac{\beta}{\beta + 1} \cdot \sin(\varphi_0). \quad (\text{B.7})$$

The following notations help in separating the real and imaginary parts of the complex expressions:

$$R_j(m) = (p_j^2 + r_j^2)^{\frac{m}{4}} \cdot \cos\left[\frac{m}{2} \cdot \tan^{-1}\left(-\frac{r_j}{p_j}\right)\right], \quad m=\text{integer number}, \quad j=1,2. \quad (\text{B.8})$$

$$I_j(m) = (p_j^2 + r_j^2)^{\frac{m}{4}} \cdot \sin\left[\frac{m}{2} \cdot \tan^{-1}\left(-\frac{r_j}{p_j}\right)\right], \quad m=\text{integer number}, \quad j=1,2. \quad (\text{B.9})$$

$$cc_j(x) = \cos(Q_j \cdot x) \cdot \cosh(P_j \cdot x), \quad j=1,2. \quad (\text{B.10})$$

$$ss_j(x) = \sin(Q_j \cdot x) \cdot \sinh(P_j \cdot x), \quad j=1,2. \quad (\text{B.11})$$

$$cs_j(x) = \cos(Q_j \cdot x) \cdot \sinh(P_j \cdot x), \quad j=1,2. \quad (\text{B.12})$$

$$sc_j(x) = \sin(Q_j \cdot x) \cdot \cosh(P_j \cdot x), \quad j=1,2. \quad (\text{B.13})$$

$$P_j = R_j(1), \quad j=1,2. \quad (\text{B.14})$$

$$Q_j = I_j(1), \quad j=1,2. \quad (\text{B.15})$$

$$aa_1 = \frac{cc_2(b-a) \cdot cs(b-a) + ss_2(b-a) \cdot sc_2(b-a)}{[cc_2(b-a)]^2 + [ss_2(b-a)]^2}. \quad (\text{B.16})$$

$$aa_2 = \frac{cc_2(b-a) \cdot sc_2(b-a) - ss_2(b-a) \cdot cs_2(b-a)}{[cc_2(b-a)]^2 + [ss_2(b-a)]^2}. \quad (\text{B.17})$$

$$bb_1 = aa_1 \cdot [a \cdot b \cdot R_2(2) - 1] - a \cdot b \cdot aa_2 \cdot I_2(2) + (b-a) \cdot P_2. \quad (\text{B.18})$$

$$bb_2 = aa_2 \cdot [a \cdot b \cdot R_2(2) - 1] + a \cdot b \cdot aa_1 \cdot I_2(2) + (b-a) \cdot Q_2. \quad (\text{B.19})$$

$$AA_1 = (-a) \cdot \frac{bb_1 \cdot (b \cdot P_2 - aa_1) + bb_2 \cdot (b \cdot Q_2 - aa_2)}{bb_1^2 + bb_2^2}. \quad (\text{B.20})$$

$$AA_2 = (-a) \cdot \frac{bb_1 \cdot (b \cdot Q_2 - aa_2) - bb_2 \cdot (b \cdot P_2 - aa_1)}{bb_1^2 + bb_2^2}. \quad (\text{B.21})$$

$$dd_1 = a \cdot [P_1 \cdot cc_1(a) - Q_1 \cdot ss_1(a)] - cs_1(a). \quad (\text{B.22})$$

$$dd_2 = a \cdot [Q_1 \cdot cc_1(a) + P_1 \cdot ss_1(a)] - sc_1(a). \quad (\text{B.23})$$

$$BB_1 = a \cdot \frac{dd_1 \cdot cs_1(a) + dd_2 \cdot sc_1(a)}{dd_1^2 + dd_2^2}. \quad (\text{B.24})$$

$$BB_2 = a \cdot \frac{dd_1 \cdot sc_1(a) - dd_2 \cdot cs_1(a)}{dd_1^2 + dd_2^2}. \quad (\text{B.25})$$

$$Y_1 = \frac{D_2}{k} - \beta \cdot AA_1 + \frac{D_2}{D_1} \cdot BB_1. \quad (\text{B.26})$$

$$Y_2 = \frac{D_2}{D_1} \cdot BB_2 - \beta \cdot AA_2. \quad (\text{B.27})$$

$$e_{11} = \frac{\beta}{D_2} \cdot [R_2(-2) \cdot \text{Re}(M_{02}) + I_2(-2) \cdot \text{Im}(M_{02})]. \quad (\text{B.28})$$

$$e_{12} = \frac{1}{D_1} \cdot [R_1(-2) \cdot \text{Re}(M_{01}) - I_1(-2) \cdot \text{Im}(M_{01})]. \quad (\text{B.29})$$

$$ee_1 = e_{11} - ee_{12}. \quad (\text{B.30})$$

$$e_{21} = \frac{\beta}{D_2} \cdot [R_2(-2) \cdot \text{Im}(M_{02}) + I_2(-2) \cdot \text{Re}(M_{02})]. \quad (\text{B.31})$$

$$e_{22} = \frac{1}{D_1} \cdot [R_1(-2) \cdot \text{Im}(M_{01}) + I_1(-2) \cdot \text{Re}(M_{01})]. \quad (\text{B.32})$$

$$ee_2 = e_{21} - e_{22}. \quad (\text{B.33})$$

$$ff_1 = \frac{D_2}{D_1} \cdot R_1(-2) - R_2(-2). \quad (\text{B.34})$$

$$ff_2 = \frac{D_2}{D_1} \cdot I_1(-2) - I_2(-2). \quad (\text{B.35})$$

$$X_1 = ee_1 \cdot ff_1 - ee_2 \cdot ff_2. \quad (\text{B.36})$$

$$X_2 = ee_1 \cdot ff_2 + ee_2 \cdot ff_1. \quad (\text{B.37})$$

The real part of the exchange term is:

$$\operatorname{Re}[Exchange(s)] = \frac{X_1 \cdot Y_1 + X_2 \cdot Y_2}{Y_1^2 + Y_2^2}. \quad (\text{B.38})$$

The real part of the non-exchange term represents the Lorentzian line-shapes corresponding to Larmor frequencies in the two compartments.

$$Lor_1 = \frac{V_1}{D_1} \cdot [R_1(-2) \cdot \operatorname{Re}(M_{01}) - I_1(-2) \cdot \operatorname{Im}(M_{01})], \quad (\text{B.39})$$

$$Lor_2 = \frac{V_2}{D_2} \cdot [R_2(-2) \cdot \operatorname{Re}(M_{02}) - I_2(-2) \cdot \operatorname{Im}(M_{02})] \quad (\text{B.40})$$

The real part of the non-exchange term is:

$$\operatorname{Re}[Non - exchange(s)] = Lor_1 + Lor_2. \quad (\text{B.41})$$

Since the magnitude of the initial magnetization was chosen to be unity, according to equation (3.12) the spectrum is then given by:

$$P(\omega) = \frac{1}{2\pi} \cdot \{\operatorname{Re}[Non - exchange(s)] + \operatorname{Re}[Exchange(s)]\}. \quad (\text{B.42})$$